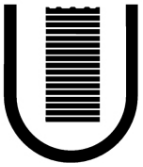

Tor Vergata University, Rome, Italy
Department of Civil and Computer Engineering
Geoinformation PhD Programme
XXV Cycle

Application of neural networks to atmospheric ozone retrievals from the Ozone Monitoring Instrument

Antonio Di Noia

Supervisor: **Dr. Fabio Del Frate**
Coordinator: **Prof. Domenico Solimini**

A thesis submitted in partial fulfillment of the requirements for the degree of Doctor of Philosophy

October 2013

Acknowledgements

Questa tesi è il coronamento di un percorso di quattro anni durante i quali ho avuto la possibilità di interagire con diverse persone, interne ed esterne al mio gruppo di ricerca, ciascuna delle quali ha dato un contributo importante alla mia formazione.

La prima persona che vorrei ringraziare è Fabio Del Frate, per aver avuto la costanza e la pazienza di seguirmi in qualità di tutor durante questi anni, e per avermi aiutato a sviluppare le mie capacità di ricerca. Lo ringrazio molto per la fiducia accordatami durante questi anni, e per aver sempre valorizzato la mia indipendenza, anche quando ho voluto seguire linee di ricerca notevolmente diverse da quelle tracciate in passato. Spero che l'esperienza di questo periodo possa anche costituire la base per nuove collaborazioni in futuro.

Ringrazio altresì il Prof. Domenico Solimini, coordinatore del corso di dottorato, per avermi trasmesso la passione per l'elettromagnetismo ed il telerilevamento durante gli anni precedenti al dottorato, e per le stimolanti discussioni scientifiche avute durante gli anni del dottorato stesso, discussioni che hanno di volta in volta riguardato argomenti complessi come la rappresentazione analitica della polarizzazione del campo elettromagnetico, la formulazione del teorema di reciprocità e l'impatto degli aerosol e dello scattering molecolare sulle misure radiometriche alle frequenze ottiche.

La mia collaborazione con il Laboratorio di Osservazione della Terra ha radici piuttosto lontane nel tempo, essendo cominciata nel 2006 con la tesi di Laurea triennale, proseguita nel 2008-2009 con quella di Laurea specialistica e culminata con questo lavoro di dottorato. La mia scelta di partecipare a questo programma di dottorato è maturata durante il corso di Laurea in Ingegneria delle Telecomunicazioni, durante il quale mi sono interessato alle tematiche dell'elettromagnetismo applicato e del telerilevamento anche grazie ad una serie di corsi tenuti da altri docenti afferenti al Laboratorio: i Proff. Giovanni Schiavon, Paolo Ferrazzoli e Leila Guerriero.

Durante gli anni trascorsi in Laboratorio ho condiviso il mio percorso con molti colleghi, con i quali ho sempre avuto un ottimo rapporto personale, e che vorrei ringraziare in queste righe. Un ringraziamento particolare va senz'altro a Lino Sellitto, il quale, lavorando su tematiche di ricerca molto vicine alle mie, è in assoluto la persona con cui ho avuto il maggior numero di interazioni. Lino mi ha seguito come co-relatore durante la mia tesi di Laurea Specialistica, ha poi collaborato con me nel progetto APOLLO, nonché alla stesura di articoli e altre pubblicazioni scientifiche, e più in generale mi ha trasmesso il proprio bagaglio di esperienza nel telerilevamento dell'ozono durante i primi anni di dottorato. Come detto in precedenza, molte sono le persone con cui ho condiviso le mie giornate in laboratorio durante questi anni. In ordine "rigorosamente casuale"[1] : Matteo Picchiani, Giorgio Licciardi, Gaia Vaglio Laurin, Daniele Latini, Chiara Pratola, Andrey Giardino, Rachid Rahmoune, Irene Fabrini, Michele Lazzarini, Ruggero Avezzano, Alessandro Piscini, Emanuele Angiuli, Alireza Taravat Najafabadi.

The final part of my PhD activity has been carried out at the Royal Netherlands Meteorological Institute (KNMI). This has been an amazing life experience, that was made possible by several people, whom I would like to thank here. The first person I would like to thank is Jos de Laat, for being my supervisor during my stay at KNMI. Jos has helped me strengthen my research results on the tropospheric ozone retrieval algorithm especially with respect to the comparisons between satellite retrievals and chemistry/transport model simulations. Furthermore, he has greatly helped me in organizing my research results so as to facilitate their publication on a scientific paper, and he has provided me with timely and decisive support every time I have needed his help, not only on the scientific side but also whenever logistic/organizational issues have come into play. A person I would like to thank next has left KNMI shortly before my arrival in the Netherlands, and this person is Mark Kroon. He has been the one who introduced me to the KNMI during a short, but intense, two-day visit that I made during October 2011, and has had a decisive role in the start of this collaboration by expressing his positive opinion over it after my brief visit mentioned before. Many thanks to Pieternel Levelt, head of the KNMI Earth Observation and Climate (AK) division, for accepting my request to work in her group; to Johan de Haan and Pepijn Veefkind for helping me understand the OMI operational ozone profile retrieval algorithm; to

[1] Onde non polarizzare nemmeno in maniera subconscia l'ordine di apparizione dei nomi, la lista mostrata di seguito e' stata generata da una routine di ordinamento casuale implementata al calcolatore.

Piet Stammes for the interesting discussions about radiative transfer, and for facilitating me in discussing my results by letting me participate to the GOME/SCIAMACHY/SEVIRI (GSS) group meetings; to Jacqueline Baas for her logistic and organizational support; to Maarten Sneep for his skillful support with the HDF data format and other programming-related issues. Furthermore, I would like to address my special thanks to Elise Hendriks for being a very nice office mate; to Tero Mielonen and Brent Maddux for the nice time spent together during lunches (and sometimes dinners) and in general for sharing their experiences of expats in the Netherlands with me; and to everyone else in the KNMI AK division for making me feel welcome in their group and for creating a pleasant working atmosphere, that I have enjoyed very much from the first to the last day.

Oltre a docenti e colleghi italiani ed olandesi, nel corso della mia attività di dottorato ho interagito con persone non facenti parte del mio gruppo di ricerca, le quali hanno contribuito al mio lavoro in qualità di fornitori di dati: Marco Cervino (ISAC-CNR); Gabriele Curci, Marco Iarlori e Vincenzo Rizi (CETEMPS); Stefania Vergari ed Emanuele Vuerich (ReSMA, Aeronautica Militare Italiana); Marcello Marinelli e Valter Sambucini (ISPRA). A tutti loro vanno i miei più sinceri ringraziamenti.

Ringrazio infine tutti i miei amici e familiari, per avermi sostenuto durante questi anni.

Contents

Preface **7**

1 Passive remote sensing of the Earth's atmosphere **9**
1.1 Radiative processes in the Earth's atmosphere 9
1.1.1 Atmospheric absorption 10
1.1.2 Atmospheric emission 13
1.1.3 Atmospheric scattering 14
1.2 The radiative transfer equation 16
1.2.1 Scalar radiative transfer equation in a LTE atmosphere without inelastic scattering 16
1.2.2 Formal solution 17
1.2.3 Plane-parallel approximation 18
1.3 Radiative transfer in the UV 19
1.3.1 Neglecting the emission terms 19
1.3.2 The solar source 19
1.3.3 UV absorption 20
1.3.4 Rayleigh scattering by air molecules 21
1.3.5 Raman scattering and Ring effect 23
1.3.6 Vertical information in UV radiance measurements . . 25
1.3.7 Effects of the Earth's surface 30
1.3.8 Effects of atmospheric aerosols 32
1.3.9 Effects of clouds 33
1.4 Retrieval techniques 37
1.4.1 Statement of the problem 37
1.4.2 Variational techinques 37
1.4.3 Neural network techniques 38
1.4.3.1 Basic concepts and terminology 38
1.4.3.2 Multilayer perceptrons 39
1.4.3.3 Neural networks in retrieval problems 40

1.4.3.4 Neural network design principles 41

2 Validation of the OMI-TOC NN tropospheric ozone column retrieval algorithm with ozone soundings over Europe 43
2.1 Introduction 43
2.2 The NASA-Aura mission and the OMI instrument 46
2.3 The OMI-TOC NN algorithm 47
2.4 Validation set and intercomparison methodology 49
2.5 Validation results 51
2.6 Correction of tropopause related errors 54
2.7 Outline 57

3 Global tropospheric ozone retrievals from OMI data by means of neural networks 61
3.1 Introduction 61
3.2 Preparation of the OMITROPO3-NN dataset 64
3.2.1 Definition of the input vector 64
3.2.2 Geographical coverage and co-location procedure . . . 67
3.2.3 Pre-processing of OMI spectral measurements 68
3.2.4 Processing of ozonesonde data 70
3.3 Design of the neural network 70
3.3.1 Training, validation and test subsets 70
3.3.2 Input pre-processing 71
3.3.3 Training and architecture selection 71
3.4 Results 72
3.4.1 Generalization during and after the training period . . 74
3.4.2 Geographical features in the retrieval algorithm 74
3.4.3 Non-climatological features 76
3.4.4 Contribution of OMI reflectances to the retrieved TCO 80
3.5 Case studies: 17th and 26th August 2006 85
3.5.1 Global retrievals 85
3.5.2 Comparisons with the TM5 Chemistry and Transport Model 87
3.5.3 Retrieval sensitivity to tropopause pressure 92
3.6 Outline 93

4 A neural network algorithm to retrieve ozone profiles from OMI data 98
4.1 Introduction 98
4.2 Methodology 99

4.3 Results . . . 101
4.3.1 Profiles . . . 101
4.3.2 Integrated columns . . . 108
4.4 Outline . . . 129

5 Conclusions **131**
5.1 Summary of the work . . . 131
5.2 Future work: error characterization . . . 132
5.2.1 NNs and averaging kernels . . . 133
5.2.2 NNs and error covariance matrix . . . 134

A Satellite TCO retrievals: An useful tool to quantify surface ozone pollution? An experiment using OMI observations **136**
A.1 Introduction . . . 136
A.2 Relationship between TCO and surface ozone . . . 137
A.3 Methodology . . . 142
A.4 July 2007 ozone episode . . . 142

Preface

The capability to build instruments able to perform accurate and comprehensive measurements of the atmospheric composition from space has been one of the most important achievements reached by the Earth Observation technology in the last 20 years. The development of satellite hyperspectral sounders covering the ultraviolet (UV), visible (VIS) and infrared regions (IR) of the electromagnetic spectrum has allowed retrievals of a large number of atmospheric constituents, thereby providing the scientific community with an unprecedented amount of data concerning the atmospheric composition and its global changes. UV/VIS/NIR spectrometers such as the Global Ozone Monitoring Experiment (GOME) and the SCanning Imaging Absorption SpectroMeter for Atmospheric CHartographY (SCIAMACHY) have made satellite retrievals of trace gases like tropospheric nitrogen dioxide (NO_2), bromine oxide (BrO), formaldehyde (HCHO) and methane (CH_4), possible for the first time in the history of remote sensing (*Burrows et al.*, 1999, 2011a). The high spatial resolution of the Ozone Monitoring Instrument (OMI) has enabled studies of tropospheric pollution events at urban scale (*Levelt et al.*, 2006a). The Infrared Atmospheric Sounding Interferometer (IASI) has provided the first global retrievals of absorbers as weak as nitric acid (HNO_3), ammonia (NH_3), methanol (CH_3OH) and formic acid (HCOOH) (*Hilton et al.*, 2012). The forthcoming TROPOspheric Monitoring Instrument (TROPOMI), scheduled for launch in 2014, is expected to provide information on the same constituents that were observed by SCIAMACHY, but at a much higher spatial resolution (*Veefkind et al.*, 2012).

As a consequence of their high spectral resolution and of their increasing capabilities in terms of spatial resolution and coverage, the state-of-the-art hyperspectral atmospheric sounders produce an amount of data that is challenging for the most established variational retrieval algorithms, that are computationally demanding because of their need for multiple runs of a radiative transfer model in order to converge to an acceptable solution of the retrieval problem. In some cases, this limitation prevents a full exploitation

of the spatial information offered by the most modern instruments. This is the case, e.g., for the operational OMI ozone profile product, where only one every five swaths of the instrument is processed in order to keep the product generation times acceptable. This problem may become even more severe with TROPOMI, given the higher spatial resolution of its future observations. This difficulties may be mitigated if fast retrieval algorithms such as neural networks are introduced in the processing chains of operational product generation environments.

During the last 20 years, the Earth Observation Laboratory of the Tor Vergata University in Rome has been active in the development of neural network algorithms for ozone retrievals from GOME (*Del Frate et al.*, 2002, 2005a,b; *Iapaolo et al.*, 2007) , SCIAMACHY (*Sellitto et al.*, 2012a,b) and OMI (*Sellitto et al.*, 2011). This dissertation continues this line of research, reporting on the latest advances obtained by our group in the development of neural network algorithms for ozone retrieval from OMI data.

The dissertation is organized as follows. Chapter 1 gives a broad overview on the passive remote sensing of the Earth's atmosphere, with a discussion of the key factors that affect the radiance measured by a satellite spectrometer in the ultraviolet, and a discussion of the principal inversion methods. Chapter 2 describes a validation of the neural network algorithm for tropospheric ozone retrievals from OMI data developed by *Sellitto et al.* (2011), that has represented the starting point for this thesis. Chapter 3 describes the design and validation of a new neural network algorithm for tropospheric ozone retrieval from OMI data, that overcomes some limitations of the previous algorithm. Chapter 4 reports on the development of a neural network algorithm to retrieve the ozone profile from OMI data. This activity has been carried out at the Royal Netherlands Meteorological Institute (KNMI). Chapter 5 summarizes the results of this work, and discusses some important tasks to be performed in the next future in order to ensure a better operational use of neural network retrievals.

Chapter 1

Passive remote sensing of the Earth's atmosphere

In this chapter, the physical principles behind the passive remote sensing of the Earth's atmosphere, as well as the techniques that can be used to infer atmospheric parameters from satellite remote measurements, are explained. Particular emphasis is given to the radiative transfer in the ultraviolet (UV) range, as this is the range of interest for the work discussed in this dissertation.

1.1 Radiative processes in the Earth's atmosphere

Passive measurements of electromagnetic radiation by a satellite or a ground-based instrument are related to the atmospheric state through the Radiative Transfer Equation (RTE). Such equation establishes a balance between energy gains and losses experienced by a beam of electromagnetic radiation traveling in a given direction. Such gains and losses result from the interactions between the electromagnetic radiation and the Earth's atmosphere and surface. Let s be a curvilinear abscissa along a direction specified by the angles (θ, ϕ) in the usual spherical coordinate system. The variation of the intensity (radiance) I_λ along such direction can be written, in a very general form, as

$$\frac{dI_\lambda}{ds} = -i_\lambda^{(l)} + i_\lambda^{(g)} \tag{1.1}$$

where λ is the wavelength, and $i_\lambda^{(l)}$ and $i_\lambda^{(g)}$ are the *lost* and *gained* intensity per unit path length, respectively.

In order to derive a more useful form for this energy balance, the two terms at the right end of the equation (1.1) must be explicitly described, by relating gains and losses of radiation to their causes.

Intensity losses along a given direction (θ, ϕ) are caused by the following phenomena:

- Absoprtion of radiation by the atmosphere and the Earth's surface.
- Scattering of radiation towards different directions with respect to (θ, ϕ).
- Scattering of radiation towards different wavelengths with respect to λ (*inelastic scattering*).

Conversely, the following mechanisms lead to gains in intensity:

- Spontaneous emission of radiation by the atmosphere and the Earth's surface.
- Scattering of radiation from other directions towards the considered (θ, ϕ).
- Scattering of radiation from other wavelengths towards the considered λ.

1.1.1 Atmospheric absorption

According to the *Beer-Lambert's law*, the loss of intensity along an infinitesimal path ds is proportional to the original intensity itself. In formal terms, we have:

$$\frac{dI_\lambda}{ds} = -k_{a,\lambda} I_\lambda \tag{1.2}$$

The proportionality constant $k_{a,\lambda}$ is called the *absorption coefficient*, and depends on the type and amount of absorbers along the radiation path. It can be written as

$$k_{a,\lambda}(s) = \sigma_{a,\lambda}(s) N_a(s) \tag{1.3}$$

where $N_a(s)$ is the number of absorbers per unit volume and $\sigma_{a,\lambda}$ is its *absorption cross-section*, that is specifical for each absorbing molecule and is often temperature dependent.

The behaviour of the absorption cross-section as a function of the wavelength is a result of phenomena that act at atomic or molecular scale. Specifically, the absorption of radiation by an atmospheric molecule leads to the

excitation of some of its quantum levels of electronic, vibrational or rotational energy. While a detailed treatment of these processes is out of the scope of this work – and the reader may refer to several books (e.g. *Goody and Yung*, 2005; *Liou*, 2002) – it might be useful to point out some of the main concepts here.

The absorption of a photon of wavelength λ by an atmospheric molecule causes a transition in its electronic, vibrational or rotational quantum numbers. Electronic transitions require the highest energies, and are thus relevant at the shortest wavelengths, in the ultraviolet (UV) and visible (VIS) spectral ranges. In the infrared (IR), the absorption is mainly caused by vibrational interactions, and at microwaves it is mainly caused by rotational interactions (which often also have a superimposed vibrational structure).

The selection rules for the aforementioned quantum transitions (i.e., the allowed transitions) depend on the molecular structure of the absorbers (polarizability and type of chemical bonds between the atoms). As a result, the absorption processes have a pronounced spectral selectivity, that is of key importance for the atmospheric remote sensing. In fact, in most cases this spectral selectivity provides the basis for the retrieval of the concentration of several atmospheric constituents.

Considerations on the quantum nature of the absorption processes would suggest that the absorption spectrum of an atmospheric molecules consists of a number of discrete lines. In this case, the wavelength dependence of the absorption cross-section would be simply written as

$$\sigma_{a,\lambda} = \sum_i \mathcal{S}_i \delta(\lambda - \lambda_i) \tag{1.4}$$

where δ is the Kronecker distribution, each λ_i is the wavelength corresponding to the i-th absorption line and $\mathcal{S}_i$ is its *strength*, which quantifies the intensity of the absorption process.

However, the absorption spectra that are observed in nature have a continuous wavelength dependence. In fact, the theoretical absorption lines are broadened because of three mechanisms:

1. *Natural broadening.* It is the broadening due to the finite lifetime of the molecular excited states. Its value is usually negligible compared to the other broadening mechanisms.

2. *Pressure broadening.* It is due to the reduction of the lifetime of the molecular excited states caused by the collisions between molecules. This mechanism is more important as the collision frequency becomes

higher. The collision frequency is proportional to the product between the density of the gas (proportional to the ratio p/T, where p is the pressure and T is the temperature) and the average molecular speed (which, in turn, is proportional to $\sqrt{T}$). As a result, the linewidth due to pressure broadening is proportional to the ratio $p/\sqrt{T}$.

3. *Doppler broadening.* It is due to the Brownian motion of the atmospheric molecules, that produces a frequency shift between the incoming radiation and the molecular absorption cross section.

As a result, it is more realistic to model the wavelength dependence of the absorption cross section as

$$\sigma_{a,\lambda} = \sum_i \mathcal{S}_i \Phi_i(\lambda, \lambda_i) \tag{1.5}$$

where each Φ_i is a *line shape* function that describes the wavelength dependence of the absorption cross-section around each (theoretical) absorption line λ_i. The functional form of the Φ_i depends on the dominant broadening mechanism. In particular:

- The effect of natural broadening is usually much smaller than the other two mechanisms.
- When pressure broadening is the dominant process, Φ_i can be approximated by a Lorentzian function, whose width is proportional to the pressure.
- When Doppler broadening dominates, Φ_i is approximated by a Gaussian function, whose width is directly proportional to the frequency and inversely proportional to the mean square velocity of the molecules.
- When the magnitudes of the two mechanisms are comparable, the line shape is described by a convolution between the Lorentzian and the Gaussian function, giving rise to the so called *Voigt* line shape. Such function has to be evaluated numerically.

The relative contribution of pressure and Doppler broadening depends on the considered spectral range and on the altitude in the atmosphere. Since the Doppler line width is proportional to the frequency, whereas the pressure line width does not depend on it, the Doppler broadening is very important at high frequencies, such as in UV and VIS, and is still noticeable in the IR. At lower frequencies, such as microwaves, pressure broadening becomes

the dominant process. However, since the pressure broadening line width is proportional to the pressure and the pressure decreases with height, a "cut-off" height exists in the atmosphere, above which the pressure broadening becomes again comparable to the Doppler broadening. Such height is usually located in the mesosphere.

The relationship between pressure broadening line width and pressure is exploited to perform atmospheric *soundings* – i.e., profile retrievals – at microwaves and in the thermal infrared. Doppler broadening, instead, does not have a significant vertical dependence, and thus it cannot be exploited to retrieve atmospheric profiles in the UV/VIS. This is the main reason why nadir UV/VIS measurements tend to have less vertical information compared to IR and microwave measurements. Nevertheless, as will be seen later in this chapter, some vertical information can still be obtained in the UV by exploiting another physical mechanism, namely the competition between Rayleigh scattering and ozone absorption.

1.1.2 Atmospheric emission

The Earth's atmosphere emits electromagnetic radiation via thermal and non-thermal processes. While the absorption of radiation by a molecule implies an excitation in some of its energetic states – caused, as seen in Section 1.1.1, by radiative and collisional processes – the emission of radiation results from a de-excitation, which may be either caused by radiative processes (spontaneous and induced recombination), collisions or other mechanisms (chemical recombinations, photochemical reactions).

When the de-excitations are mainly caused by inelastic collisions, the populations of the excited states satisfy the Boltzmann distribution, and it is possible to define a local kinetic temperature $T(s)$. In such case, known as Local Thermodynamical Equilibrium (LTE), it can be shown that the radiance emitted per unit path length is given by

$$i_\lambda^{\mathrm{em}} = k_{a,\lambda} B_\lambda(T(s)) \tag{1.6}$$

where $B_\lambda(T(s))$ is the black body radiance at the temperature $T(s)$, given by the Planck's distribution:

$$B_\lambda(T) = \frac{2hc^2}{\lambda^5} \frac{1}{\exp\left(\dfrac{hc}{k_B \lambda T}\right) - 1} \tag{1.7}$$

In the Equation (1.7), h is the Planck's constant, c is the light speed in vacuum and k_B is the Boltzmann's constant. The use of the absorption

coefficient $k_{a,\lambda}$ in Equation (1.6) is justified by the Kirchhoff's reciprocity law, according to which the emission and absorption properties of a medium in LTE are the same. The black body radiance is isotropic and unpolarized, and only depends on the temperature of the emitting surface.

If the LTE condition is not verified, the Equation (1.6) does not apply, and the expression for the emitted radiance becomes more complicated. Specifically, in Non-LTE (NLTE) cases, the emitted radiance depends on the radiation field itself. More details about the parametrization of NLTE emissions can be found in *López-Puertas and Taylor* (2001). The LTE condition is not verified at short wavelengths – such as in the UV/VIS – because the kinetic energy at typical atmospheric temperatures is much smaller than the energy associated with electronic transitions; and also at longer wavelengths where the atmospheric density is small – i.e., in the upper atmosphere – because of the reduced probability of collisions between molecules or atoms. Important instances of NLTE emissions are the airglow and the auroral emissions that occur in the upper atmosphere, and cover a broad spectral range that extends from the Extreme Ultraviolet (EUV) to the infrared (IR). These emission mechanisms are exploited in UV remote sensing, in order to monitor the extension of the auroral oval and to measure the upper atmospheric composition by using the airglow as radiation source (*Meier*, 1991; *Huffman*, 1992). Another source of non-thermal emission is the fluorescence from vegetation, that is particularly intense at certain wavelengths in the deep red and near infrared (*Entcheva Campbell et al.*, 2008), and that can be observed from space since few years (*Joiner et al.*, 2011; *Guanter et al.*, 2012).

1.1.3 Atmospheric scattering

In addition to absorbing and emitting radiation, atmospheric molecules and particles also scatter radiation. If the scattering process does not involve a change in the wavelength of the scattered radiation, it is said to be *elastic*. Conversely, the scattering process is said to be *inelastic* if the wavelength of the scattered radiation differs from the wavelength of the incident radiation.

Scattering may be either a loss or a gain mechanism, depending on the considered direction. Specifically, part of the intensity of a traveling beam is lost due to scattering towards other directions. On the other hand, radiation traveling in other directions may be scattered towards the considered direction, leading to a gain in intensity.

The intensity lost per unit path length due to elastic scattering towards

all the possible directions is proportional to the incident intensity, i.e.

$$\frac{dI_\lambda}{ds} = -k_{s,\lambda} I_\lambda \tag{1.8}$$

The proportionality constant, called the *scattering coefficient*, can be written as

$$k_{s,\lambda}(s) = \sigma_{s,\lambda}(s) N_s(s) \tag{1.9}$$

where $N_s(s)$ is the number of scattering particles per unit volume and $\sigma_{s,\lambda}$ is its *scattering cross-section* of a particle.

It is useful to define the *extinction coefficient* as the sum of absorption and scattering coefficients:

$$k_{e,\lambda} = k_{a,\lambda} + k_{s,\lambda} \tag{1.10}$$

The extinction coefficient quantifies the fraction of the incoming intensity that is lost due to scattering and absorption. Another useful parameter is the *single scattering albedo*, defined as

$$\varpi_\lambda = \frac{k_{s,\lambda}}{k_{e,\lambda}} \tag{1.11}$$

The intensity gained per unit path length due to elastic scattering from other directions can be written as

$$\frac{dI_\lambda}{ds} = \frac{k_{s,\lambda}}{4\pi} \int_0^{2\pi} \int_{-1}^{1} P_\lambda(s, \mu', \phi', \mu, \phi) I_\lambda(s, \mu', \phi') d\mu' d\phi' \tag{1.12}$$

where the cosine of the zenith angle $\mu = \cos\theta$ has been introduced. In Equation (1.12), P_λ is the *scattering phase function* of the propagation medium. Such function describes the directional distribution of the scattering properties of the medium. Specifically, the radiance scattered from the direction (μ_i, ϕ_i) towards the direction (μ_s, ϕ_s) is written as

$$I_\lambda(s, \mu_s, \phi_s) = \frac{k_{s,\lambda}}{4\pi} P_\lambda(s, \mu_i, \phi_i, \mu_s, \phi_s) I_\lambda(s, \mu_i, \phi_i) \tag{1.13}$$

The scattering behaviour of atmospheric particles depends on the ratio between their linear dimensions and the wavelength. In particular, once the *size parameter* of a scattering particle is defined as

$$x = \frac{2\pi r}{\lambda} \tag{1.14}$$

where r is the particle radius, it is possible to define three scattering regimes:

- *Rayleigh scattering* ($x \ll 1$). The scattering coefficient is inversely proportional to λ^4. The phase function depends very weakly on the direction and the particle shape.

- *Resonance scattering* ($x \approx 1$). The scattering coefficient and phase function are strongly dependent on the particle shape. The scattering properties of the object can be computed only by solving the Maxwell's equations exactly. For spherical objects, the resonance scattering is called *Mie scattering*, after Gustav Mie, who first solved the scattering problem for spheres (*Mie*, 1908). The scattering phase functions of spherical objects in the Mie regime have a peak in the forward direction. Such peak becomes more pronounced as x increases.

- *Geometric optics* ($x \gg 1$). The concept of scattering can be replaced with the Snell's laws of reflection and refraction, and the scattering parameters can be replaced with the Fresnel's coefficients accordingly.

After this discussion, it is clear that the scattering properties of an object are wavelength dependent. For instance, atmospheric molecules ($r \approx 10^{-5}$ μm) are sources of Rayleigh scattering in the UV/VIS spectral range (approximately until the blue region of the VIS spectrum), whereas their effect becomes negligible at longer wavelengths. Aerosol and haze particles ($r \approx 0.1 \div 1$ μm) are sources of Mie scattering in the UV/VIS range, can cause Mie or Rayleigh scattering in the IR depending on their size, and can be neglected at microwaves. The scattering from cloud droplets ($r \approx 10$ μm) is in geometrical or Mie regime at VIS wavelengths and in Rayleigh regime at millimeter wavelengths, while it is negligible at microwaves. Hydrometeors ($r \approx 1$ mm) can be approximated as Rayleigh scatterers at microwaves and as Fresnel reflectors at short wavelengths.

1.2 The radiative transfer equation

1.2.1 Scalar radiative transfer equation in a LTE atmosphere without inelastic scattering

The discussions developed in Sections 1.1.1 to 1.1.3 allow to explicitly write down the terms of the Equation (1.1). From now on, the subscript λ in the wavelength dependent quantities will be omitted in order to simplify the notation.

It is clear, now, that the term $i^{(l)}$ at the right end of Equation (1.1) is the sum of the Equations (1.2) and (1.8). The term $i^{(g)}$, instead, is obtained by

summing the Equations (1.6) (under the LTE assumption) and (1.12) (under the assumption of elastic scattering). Therefore, it is possible to write the radiative transfer equation for an LTE, elastically scattering atmosphere, as

$$\frac{dI(s,\mu,\phi)}{ds} = -k_e(s)I(s,\mu,\phi) + k_a(s)B(T(s)) + \frac{k_s(s)}{4\pi}\int_0^{2\pi}\int_{-1}^{1} P(s,\mu',\phi',\mu,\phi)I(s,\mu',\phi')d\mu' d\phi' \quad (1.15)$$

A further assumption that was implicitly made in the derivation of the Equation (1.15) is that the considered radiative processes do not depend on polarisation. In the real atmosphere this is assumption is often too simplistic. In particular, polarisation is often important in the scattering processes. For instance, the Rayleigh scattering produced by the atmospheric molecules in the UV/VIS, polarizes the incoming Solar radiation. Sometimes, also absorption and emission processes may be polarisation dependent. An example is the Zeeman splitting of the oxygen emission lines at mm waves, that is important in the upper atmosphere and must be properly accounted for in radiative transfer models (*Rosenkranz and Staelin*, 1988).

In order to account for polarisation, a radiative transfer equation must be derived for all the four component of the Stokes vector of the radiation, which has the radiance I as first component. In this case, the extinction coefficient and the scattering phase function must be replaced with matrices. More details can be found – for instance – in *Mishchenko* (2002). The polarimetric version of the RTE is often referred to as Vector Radiative Transfer Equation (VRTE).

1.2.2 Formal solution

The Equation (1.15) is an integro-differential equation, as the unknown quantity – i.e. the radiance field I – appears as argument of both a derivative and an integral. An analytical solution of the Equation (1.15) is not possible unless strong assumptions are made about the spatial distribution of k_e, T and the expression of P. However, even an implicit solution of the equation gives some insight on the physical processes that lie behind measurements of atmospheric radiation by means of remote instruments. In order to obtain such a solution, it is useful to incorporate the processes leading to gains of

radiation in a *source function*

$$S(s,\mu,\phi) = k_a(s)B(T(s)) + \frac{k_s(s)}{4\pi}\int_0^{2\pi}\int_{-1}^{1} P(s,\mu',\phi',\mu,\phi)I(s,\mu',\phi')d\mu' d\phi' \quad (1.16)$$

In this case, it is possible to prove that the solution of the Equation (1.15) can be written as

$$I(s,\mu,\phi) = I(s_0,\mu,\phi)\exp\left(-\int_{s_0}^{s} k_e(s')ds'\right) + \int_{s_0}^{s} S(s',\mu,\phi)\exp\left(-\int_{s'}^{s} k_e(s'')ds''\right)ds' \quad (1.17)$$

where $I(s_0,\mu,\phi)$ serves as boundary condition at some point s_0 along the integration path. The Equation (1.17) shows that the radiance measured at a point s is given by the boundary radiance (e.g. the radiance at the Earth's surface if a downward-looking instrument is considered, or the radiance at the top of atmosphere in the case of an upward-looking instrument), attenuated by the extinction along the propagation path, plus a sum of the source contributions along the integration path, attenuated by the extinction along the path between the source points and the point s.

The Equation (1.17) represents a formal solution of the scalar RTE (1.15). In order to find the actual solution, the expressions for the boundary radiance and the source function (which may in turn depend on the radiance I) must be assigned.

1.2.3 Plane-parallel approximation

If θ is not close to $\pi/2$ (i.e. if μ is not close to zero), the curvature of the Earth's atmosphere can be neglected. In this case, the curvilinear abscissa s along the integration path can be related to the vertical coordinate z through the simple equation

$$ds = dz/\mu \quad (1.18)$$

Thus, the RTE (1.15) can be rewritten as

$$\mu\frac{dI}{dz} = -k_e I + S \quad (1.19)$$

where S is the source function as defined in Equation (1.16). At this point, it is useful to define the *vertical optical depth* as

$$\tau = \int_z^{\infty} k_e(z')dz \quad (1.20)$$

and rewrite the Equation (1.19) in the compact form

$$\mu \frac{dI}{d\tau} = -I + J \tag{1.21}$$

where $J = S/k_e$. If this formalism is used, the formal solution of the RTE for a plane-parallel atmosphere can be written as

$$I(\tau, \mu, \phi) = I(\tau_0, \mu, \phi) e^{-(\tau_0 - \tau)/\mu} + \frac{1}{\mu} \int_{\tau_0}^{\tau} J(\tau', \mu, \phi) e^{-(\tau' - \tau)/\mu} d\tau' \tag{1.22}$$

Of course, a satellite instrument is placed at $\tau = 0$.

1.3 Radiative transfer in the UV

Having derived a general form for the radiative transfer equation, it is useful to describe the radiative processes that affect satellite measurements in the Near Ultraviolet (NUV) range, as this is the range of interest in this work. The aim of this section is to describe the radiative environment in which instruments and retrieval algorithms must operate.

1.3.1 Neglecting the emission terms

The ozone retrieval algorithms of our interest derive ozone information from high spectral resolution measurements of the UV solar radiation backscattered by the Earth's atmosphere towards a satellite instrument. Therefore, the measurements are performed during daytime. As a consequence, the emission terms in the RTE – due to airglow emissions from the upper atmosphere – can be neglected when nadir observations are considered, because such emissions are much weaker than the solar backscattered radiance.

1.3.2 The solar source

While in many remote sensing applications – mostly related to solid Earth observation – the spectrum of the solar radiation is approximated by a black body spectrum at the temperature of about 6000 K, such approximation is not acceptable in the context of hyperspectral atmospheric remote sensing. In fact, the spectral resolutions of the current UV/VIS/NIR atmospheric spectrometers are fine enough to observe narrowband features in the solar irradiance spectrum. Such features, that make the solar irradiance spectrum different from a blackbody spectrum, are essentially the *Fraunhofer lines*, i.e. absorption lines of chemical constituents (oxygen, hydrogen, helium

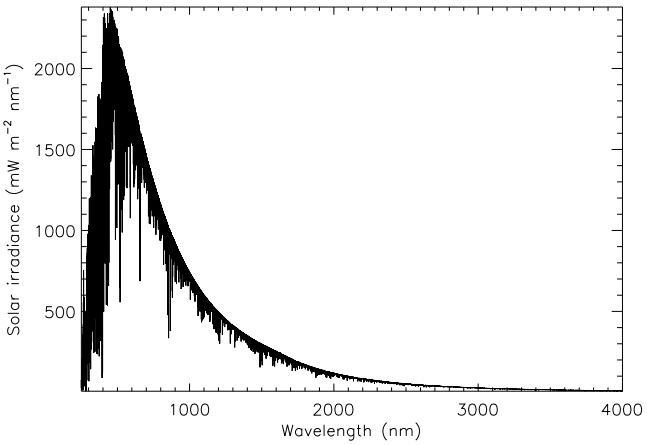

Figure 1.1: Solar irradiance spectrum between 250 nm and 4 μm with a spectral resolution of 0.1 nm. Data taken from *Kurucz* (1993).

and several metals) of the outer solar atmosphere. Figure 1.1 shows a plot of the solar irradiance spectrum between 250 nm and 4 μm measured at a resolution of 0.1 nm by *Kurucz* (1993).

1.3.3 UV absorption

The gaseous absorption in the UV is largely dominated by ozone. The spectral region where the strongest absorption by O_3 occurs consists of the Hartley bands ($200 \div 310$ nm). Furthermore, ozone also absorbs radiation in the Huggins bands ($310 \div 350$ nm). In this latter spectral range, the ozone absorption cross section displays a considerable temperature dependence. Fig. 1.2 shows the spectral dependence of the ozone absorption cross section between 260 and 340 nm at four temperatures (180, 240, 260 and 300 K). The plot has been produced using data published in *Bass and Paur* (1985).

Other trace gases that have absorption features in the UV are sulphur dioxide (SO_2), formaldehyde (HCHO), chlorine dioxide (OClO) and bromine oxide (BrO). However, their absorption cross sections are several orders of magnitude smaller than the O_3 cross sections, and they may interfere with ozone retrievals only when very large amounts of these gases are present in the observed scene (e.g. in case of intense volcanic eruptions, which release large amounts of SO_2).

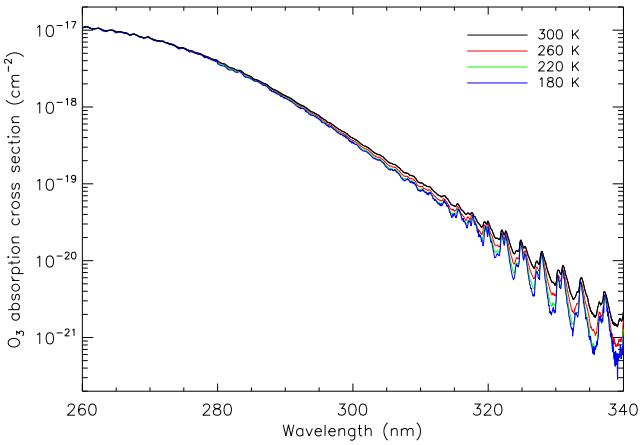

Figure 1.2: Ozone absorption cross section between 260 and 340 nm at 180, 240, 260 and 300 K. Data taken from *Bass and Paur* (1985).

1.3.4 Rayleigh scattering by air molecules

Rayleigh scattering by air molecules is the main reason why a satellite instrument is able to detect appreciable levels of UV radiation from the Earth's atmosphere. The solar radiation induces an electrical dipole moment in the atmospheric molecules. As a consequence, such molecules radiate a secondary electromagnetic field. The induced dipole moment in a molecule can be expressed by a tensor product series:

$$\mathbf{p} = \sum_{k=1}^{\infty} \frac{1}{k!} \boldsymbol{\alpha}_k \mathbf{E}_{loc}^k \tag{1.23}$$

where $\mathbf{E}_{loc}$ is the electric field in the molecule, $\mathbf{E}_{loc}^k$ is the tensor product of $\mathbf{E}_{loc}$ by itself taken k times, and $\boldsymbol{\alpha}_k$ is the *polarizability tensor* of order k of the considered molecule. It is often enough to consider only the first term of the right end of the Equation (1.23), which gives rise to Rayleigh (and Raman, as will be seen in the next section) scattering. The higher order terms, if considered, are called hyper-Rayleigh (and Raman) terms.

In the following discussion, the higher order terms of the induced dipole moment will be always neglected. Therefore, the term "polarizability" and the symbol $\boldsymbol{\alpha}$ will be used to designate the first order polarizability $\boldsymbol{\alpha}_0$.

If the considered molecule is spherically symmetric, i.e. it has an isotropic polarizability, then $\boldsymbol{\alpha}$ is a diagonal tensor, whose nonzero elements all amount

to a common value α. In this case, it can be shown that the Rayleigh cross section of a molecule is given by

$$\sigma_R = \frac{8\pi^3\alpha^2}{3\epsilon_0^2\lambda^4} \tag{1.24}$$

where ϵ_0 is the vacuum permittivity.

The polarizability can be related to the molecular refractive index n via the *Clausius-Mossotti (or Lorentz-Lorentz) relation:*

$$\alpha = \frac{3\epsilon_0}{N}\left(\frac{n^2-1}{n^2+2}\right) \tag{1.25}$$

where N is the number of molecules per unit volume. Tables of the refractive index of standard air in the ultraviolet can be found in *Penndorf* (1957).

The effect of the molecule anisotropy is accounted for by multiplying the Equation (1.24) by a correction factor that has been proposed for the first time by *King* (1923). If $\alpha^{\parallel}$ and $\alpha^{\perp}$ are the parallel and the perpendicular components of the polarizability with respect to the electric field, respectively, then the King's correction factor can be written as (*Bates*, 1984):

$$F_K = 1 + 2\left(\frac{\gamma}{3\bar{\alpha}}\right)^2 \tag{1.26}$$

where $\gamma = \alpha^{\parallel} - \alpha^{\perp}$ and $\bar{\alpha} = (\alpha^{\parallel} + 2\alpha^{\perp})/3$. Alternative expressions of F_K are based on the definition of the *depolarization ratio* ρ, such as

$$F_K = \frac{6+3\rho}{6-7\rho} \tag{1.27}$$

Further details about the definition of ρ can be found in *Bhahethi and Fraser* (1980), and *Young* (1980, 1981).

The Rayleigh optical depth of the atmosphere is proportional to the atmospheric pressure, following the relationship (*Bodhaine et al.*, 1999)

$$\tau_R = \sigma_R \frac{pN_A}{m_a g} \tag{1.28}$$

where p is the pressure, N_A Avogadro's number, m_a is the mean molecular weight of air and g is the gravity acceleration.

The results of calculations of the Rayleigh cross-section and optical depth for air as functions of wavelengths can be found in *Fröhlich and Shaw* (1980), *Bucholtz* (1995) and *Bodhaine et al.* (1999).

The Rayleigh phase function for the radiance can be expressed as

$$P(\Theta) = \frac{3}{2}\frac{1+\rho}{2+\rho}\left(1 + \frac{1-\rho}{1+\rho}\cos^2\Theta\right) \tag{1.29}$$

where Θ is the angle between the scattering and the observation direction. However, as a consequence of the anisotropy of the air molecules, Rayleigh scattering is polarizing. Therefore, the spatial distribution of the scattered radiation must be expressed by a phase matrix. The reader may refer to *Hansen and Travis* (1974) and *Ahmad and Bhartia* (1995) for details.

1.3.5 Raman scattering and Ring effect

Besides producing Rayleigh scattering, the atmospheric molecules are also responsible for Raman scattering. Raman scattering is an inelastic scattering process, i.e. the wavelength of the scattered radiation differs from the wavelength of the incident radiation. Raman scattering from a molecule is caused by temporal variabilities in its polarizability tensor due to vibrational or rotational motions. While a complete treatment of the Raman scattering would require a complex quantum mechanical approach, an approximated treatment based on classical concept gives some insight on the scattering process. The linear induced dielectric dipole moment in a molecule (first order term at right hand in Equation (1.23)) is related to the local electric field $\mathbf{E}$ by the relationship

$$\mathbf{p}^{(1)} = \boldsymbol{\alpha} \cdot \mathbf{E} \tag{1.30}$$

where α is the polarizability tensor of the molecule. Let $Q_0, Q_1, \ldots$ the natural vibration (or rotation) coordinates of the molecule. Such coordinates will have a time dependence of the form (*Long*, 2002)

$$Q_k = Q_{k0}\cos(\omega_k t + \delta_k) \tag{1.31}$$

where ω_k and δ_k are respectively the circular frequency and the phase associated with the k-th molecular vibrational or rotational mode. If the relationship between the polarizability tensor and the coordinate Q_k is approximated by a first order Taylor expansion, it is possible to write

$$\boldsymbol{\alpha} = \boldsymbol{\alpha}_0 + \boldsymbol{\alpha}'_k Q_k \tag{1.32}$$

where $\boldsymbol{\alpha}'_k = \partial\boldsymbol{\alpha}/\partial Q_k$ evaluated in the equilibrium position $Q_k = 0$. By substituting Eq. (1.31) in Eq. (1.32), and then Eq. (1.32) in Eq. (1.30), one finds that the linear induced dipole moment associated with an electric field

$$\mathbf{E} = \mathbf{E}_0\cos(\omega_0 t) \tag{1.33}$$

will be

$$\mathbf{p}^{(1)} = \boldsymbol{\alpha}_0 \mathbf{E}_0 \cos(\omega_0 t) + \boldsymbol{\alpha}'_k \mathbf{E}_0 \cos(\omega_k t + \delta_k) \cos(\omega_0 t) \tag{1.34}$$

By using simple trigonometric relationships, Eq. (1.34) can be rearranged as

$$\mathbf{p}^{(1)} = \mathbf{p}^{(1)}(\omega_0) + \mathbf{p}^{(1)}(\omega_0 - \omega_k) + \mathbf{p}^{(1)}(\omega_0 + \omega_k) \tag{1.35}$$

where the following identities hold:

$$\mathbf{p}^{(1)}(\omega_0) = \boldsymbol{\alpha}_0 \cdot \mathbf{E}_0 \tag{1.36}$$

$$\mathbf{p}^{(1)}(\omega_0 \pm \omega_k) = \frac{1}{2} \boldsymbol{\alpha}'_0 Q_k \cdot \mathbf{E}_0 \cos[(\omega_0 \pm \omega_k)t + \delta_k] \tag{1.37}$$

Therefore, to summarize, the coupling between the frequency of the electric field and the characteristic frequency of the k-th vibration (or rotation) mode in the molecule, gives rise to two terms in the linear induced dipole moment whose frequencies are different from that of the electric field. Such terms are responsible for Raman scattering.

The quantity $\mathbf{p}^{(1)}(\omega_0)$ represents the standard Rayleigh term that would be obtained even in absence of variabilities in the polarizability tensor. Such term can be referred to in many ways in literature. Some authors call it "Rayleigh line", some others prefer to use the name "Cabannes line", as they consider Raman scattering as a component of Rayleigh scattering. A broad discussion about this matter can be found in *Young* (1982). For the sake of simplicity, henceforth we will simply distinguish Rayleigh and Raman scattering – as done by *Long* (2002) – although we are aware that such definition may be historically inaccurate.

$\mathbf{p}^{(1)}(\omega_0 - \omega_k)$ and $\mathbf{p}^{(1)}(\omega_0 + \omega_k)$ are called the Stokes and anti-Stokes components of Raman scattering, respectively. Eq. (1.37) contains an important point. In fact, it shows that only the molecules whose polarizability tensor changes with the rotation or vibration coordinates produce Raman scattering. In particular, it can be shown that all the biatomic molecules are Raman active, whereas for the polyatomic molecules a "mutual exclusion rule" exists between the Raman active and the infrared active modes (*Long*, 2002).

In the Earth system, it is useful to distinguish two Raman scattering mechanisms; the rotational Raman scattering (RRS) and the vibrational Raman scattering (VRS). In the UV, the atmospheric molecules – especially oxygen (O_2) and nitrogen (N_2) – are mainly responsible for RRS, whereas an appreciable level of VRS is produced by liquid water. As a result, significant VRS signals can be observed in satellite high resolution spectra measured over oceans (*Vasilkov et al.*, 2002).

A possible method to account for Raman scattering in radiative transfer computations is described in *Vountas et al.* (1998). The key idea of this method is to add two further terms to the RTE (1.15): the gain in radiance due to scattering of radiation from Raman lines adjacent to the considered λ

$$i^{(g)}_{\text{Raman}} = \sum_{j=1}^{L} k_s^{\text{Ram}}(s, \lambda_j, \lambda) \int_0^{2\pi} \int_{-1}^{1} P_{\text{Ram}}(s, \mu', \phi', \mu, \phi) I_{\lambda_j}(s, \mu', \phi') d\mu' d\phi' \tag{1.38}$$

and the loss due to scattering towards other wavelengths:

$$i^{(l)}_{\text{Raman}} = \sum_{i=1}^{L} k_s^{\text{Ram}}(s, \lambda, \lambda_i) \int_0^{2\pi} \int_{-1}^{1} P_{\text{Ram}}(s, \mu', \phi', \mu, \phi) I_{\lambda}(s, \mu', \phi') d\mu' d\phi' \tag{1.39}$$

In these equations, k_s^{Ram} is the scattering coefficient associated to the considered Raman transition, and P_{Ram} is the Raman phase function. More detailed explanations about these and related quantities can be found in *Kattawar et al.* (1981) and *Joiner et al.* (1995).

RRS from atmospheric molecules has been found to be the main responsible for the so-called *Ring effect* (*Grainger and Ring*, 1962), after the name of one of its discoverers, J. Ring. This effect consists in a filling-in of the solar Fraunhofer lines that is observed in Top Of Atmosphere (TOA) earthshine radiance spectra. A very effective explanation for this effect can be found in *van Deelen* (2007). Since the solar irradiance in a Fraunhofer line λ_F is much smaller than the irradiance at other wavelengths, the amount of radiation scattered from other wavelengths to the Fraunhofer line tends to be larger than the radiation that is elastically scattered in the line itself. Therefore, the inelastic scattering causes a net gain of radiation at λ_F and a net loss at the other wavelengths. As a consequence, when the TOA radiance is divided by the incident solar irradiance in order to compute a TOA reflectance, a peak in the Fraunhofer lines appears. The overall process is illustrated in Figure 1.3.

1.3.6 Vertical information in UV radiance measurements

In order to understand the penetration of the UV radiation in the Earth's atmosphere, it is useful to discuss the formal solution of the RTE (1.17) under the following assumptions:

1. Plane parallel approximation.

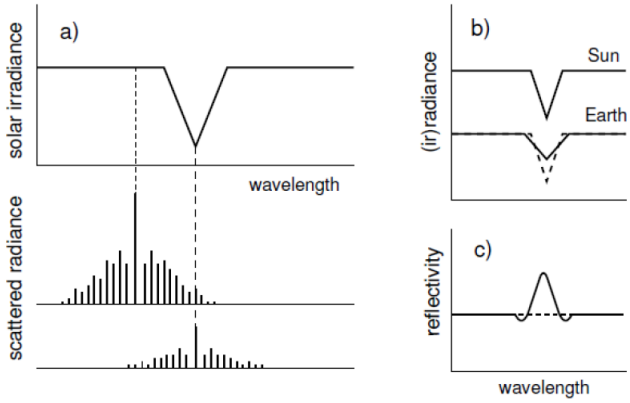

Figure 1.3: Schematic explanation of the filling-in of the solar Fraunhofer lines and its impact on top of atmosphere reflectance calculations. a) Wavelength distribution of the scattered irradiance (due to Rayleigh and Raman scattering) inside and outside a Fraunhofer line of the solar spectrum; b) solar irradiance (above) and earthshine radiance (below) with filling-in of the Fraunhofer line; c) spurious spectral feature in the reflectance spectrum caused by the filling-in. From *van Deelen* (2007).

2. No clouds and aerosols.
3. No multiple scattering.
4. No inelastic scattering.
5. Ozone is the only absorbing trace gas.
6. Negligible contribution from the surface.

The first assumption allows to write the RTE as in the Equation (1.19). The assumptions 2–4 allow to simplify the form of the source function considerably. The last assumption allows to assume that the first term at the right end of Equation (1.17) is zero.

The first step in the solution of Equation (1.19) is the specification of the source function S, whose general expression is given by the Equation (1.16). Of course, in the case of UV daytime observations, the emission term at the right end of Equation (1.16) can be neglected. Furthermore, if only single scattering is considered and atmospheric molecules are the only source of scattering, also the scattering term in Eq. (1.16) can be simplified. In fact, if

$F^{\odot}$ is the solar irradiance outside the atmosphere and $\mu_{\odot}$ is the solar zenith angle, the source function at a height z in the atmosphere can be written as

$$S(z) = \frac{F^{\odot}}{4\pi} k_s(z) P(\Theta) \cdot \exp\left[-\frac{1}{\mu_{\odot}} \int_z^{z_{\mathrm{TOA}}} k_e(z')dz'\right] \tag{1.40}$$

Here, since only atmospheric scattering is considered and no inelastic scattering is assumed, $P(\Theta)$ and $k_s(z)$ are the Rayleigh phase function and scattering coefficient, respectively. The extinction coefficient k_e, that appears inside the integral at the right end of Eq. (1.40), is given by the sum of the Rayleigh scattering coefficient and the absorption coefficient of the atmospheric trace gases. If only the absorption by ozone is considered, the extinction coefficient can be written as

$$k_e(z) = k_s(z) + k_a(z) = \sigma_s(z) N_{\mathrm{air}}(z) + \sigma_a(z) N_{\mathrm{O_3}}(z) \tag{1.41}$$

where $\sigma_s(z)$ and $\sigma_a(z)$ are the Rayleigh scattering and ozone absorption cross section at the height z, respectively, and $N_{\mathrm{air}}(z)$ and $N_{\mathrm{O_3}}(z)$ are respectively the number of air and ozone molecules per unit volume at the height z. It can be noticed that the integral represents the optical thickness between the height z and the TOA. Therefore, it is possible to write

$$\tau(z, z_{\mathrm{TOA}}) = \tau_R(z, z_{\mathrm{TOA}}) + \tau_{\mathrm{O_3}}(z, z_{\mathrm{TOA}}) \tag{1.42}$$

where the optical thickness was split in a component due to Rayleigh scattering, τ_R, and a component due to ozone absorption, $\tau_{\mathrm{O_3}}$.

The Rayleigh component can be related to the pressure $p(z)$ as in Equation (1.28). Given the definition of optical depth, this means that it is possible to express the Rayleigh scattering coefficient as

$$k_s(z) = -\frac{d\tau_R}{dz} = -\beta^* \frac{dp}{dz} \tag{1.43}$$

where $\beta^* = (\sigma_R N_A)/(m_a g)$ is the Rayleigh scattering coefficient per unit pressure.

At this point, another simplification can be made. If it is assumed that the ozone absorption cross section is constant with height, then the optical thickness associated with ozone can be written as

$$\tau_{\mathrm{O_3}} = \alpha^* X_{\mathrm{O_3}}(z) \tag{1.44}$$

where $X_{\mathrm{O_3}}(z)$ is the integrated columnar ozone concentration above the height z, and α^* is the ozone absorption coefficient per unit ozone amount.

The assumption of σ_a constant with z is not rigorously valid in the ozone Huggins bands, because of the dependence of σ_a on the temperature in that spectral range. However, this assumption may be helpful in order to understand, at least qualitatively, the vertical sensitivity of UV radiance measurements.

With the above mentioned simplifications, combining the Equations (1.15) and (1.16), and using the plane parallel approximation, the formal solution of the RTE can be written as

$$I(z_{\mathrm{TOA}},\mu) = \frac{F^{\odot}}{4\pi\mu} P(\Theta)\beta^* \int_{z_{\mathrm{TOA}}}^{z_0} \exp\left[-M\left(\beta^* p(z') + \alpha^* X_{\mathrm{O_3}}(z')\right)\right] \frac{dp}{dz'} dz' \tag{1.45}$$

where z_0 is the surface level and the geometric air mass factor $M = \mu^{-1} + \mu_{\odot}^{-1}$ has been defined.

Equation (1.45) simplifies if the pressure p is used as integration variable instead of the height z. In fact, in such case one has

$$I(0,\mu) = \frac{F^{\odot}}{4\pi\mu} P(\Theta)\beta^* \int_{0}^{p_s} \exp\left[-M\left(\beta^* p + \alpha^* X_{\mathrm{O_3}}(p)\right)\right] dp \tag{1.46}$$

where p_s is the surface pressure and $p = 0$ was assumed for the TOA.

Bhartia et al. (1996) suggest the following procedure to evaluate the contribution of the atmospheric levels to the measured radiance. First, the fractional contribution of a layer whose thickness is $d(\ln p)$ is described by means of the Radiance Contribution Function (RCF)

$$C_\lambda(p) = p \cdot \exp\left[-M\left(\beta^*_\lambda p + \alpha^*_\lambda X_{\mathrm{O_3}}(p)\right)\right] \tag{1.47}$$

Then, the pressure level p_k where the RCF attains its maximum value can be found by differentiating $C(p)$, so as to obtain

$$\frac{dC_\lambda}{d\ln p} = p\left(1 - M\alpha^*_\lambda \frac{dX}{d\ln p} - Mp\beta^*_\lambda\right) \exp\left[-M\left(\beta^*_\lambda p + \alpha^*_\lambda X_{\mathrm{O_3}}(p)\right)\right] \tag{1.48}$$

Setting $dC_\lambda/d\ln p$ to zero, one finds the condition that must be satisfied by p_k for the RCF to have a maximum:

$$M\left(\alpha^*_\lambda \left.\frac{dX}{d\ln p}\right|_{p_k} + \beta^*_\lambda p_k\right) = 1 \tag{1.49}$$

Depending on the wavelength λ, three cases can be distinguished:

1. At "short" UV wavelengths (less than about 300 nm) the ozone absorption cross sections are so large that the first term at the left end of Eq. (1.49) dominates. Therefore, the peak wavelength satisfies the approximate relationship

$$\left.\frac{dX}{d\ln p}\right|_{p_k} \approx \frac{1}{\alpha_\lambda^* M} \tag{1.50}$$

   This result is extremely important, because it tells that the peak pressure p_k can be varied (i.e., the atmosphere can be scanned vertically) by either varying λ or M. The state-of-the-art satellite UV instruments sound the atmosphere by measuring radiation at multiple wavelengths.

   At these wavelengths, the RCF peaks usually occur at relatively high altitudes, because the large ozone optical thickness prevents UV radiation from reaching the lower atmospheric layers. It is important to point out that the shape of the RCFs in this spectral range depends on the ozone profile shape $X(p)$. Therefore, our considerations regarding the penetration depth of UV radiation in this spectral wavelength hold for "typical" ozone profiles. In cases like ozone hole conditions, instead, radiation at wavelengths that are as short as 300-305 nm might also penetrate down to the troposphere.

2. At "long" UV wavelengths (more than about 310 nm), α_λ^* becomes small, and Rayleigh scattering dominates. In such case, the peak wavelength is approximately given by

$$p_k \approx \frac{1}{\beta_\lambda^* M} \tag{1.51}$$

   At these wavelengths, the RCF peaks usually occur in the lower stratosphere, and the RCFs are appreciably different from zero also in the troposphere. Usually, low contributions can be expected from the upper stratosphere, because of the small air density, that makes Rayleigh scattering less efficient.

3. At "intermediate" wavelengths the effects are comparable, and no further simplifications of Eq. (1.49) are possible. The RCFs have usually two peaks, and are significantly different from zero throughout the entire atmosphere. Therefore, these wavelengths are particularly well suited for the retrieval of the total ozone column.

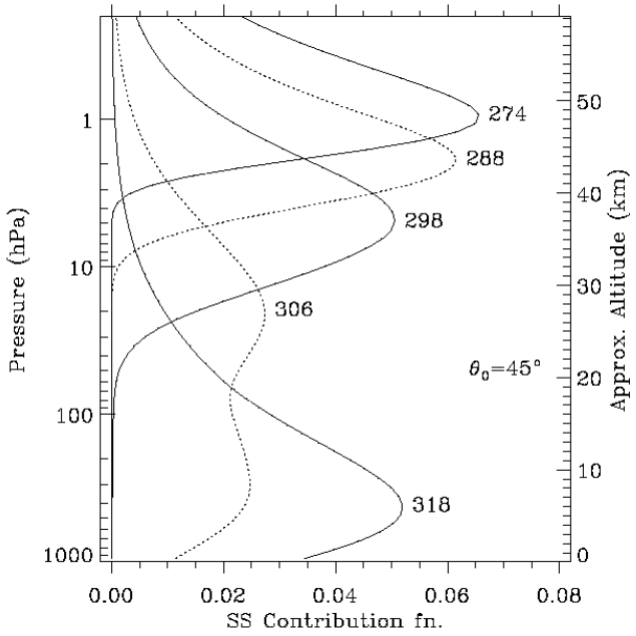

Figure 1.4: Radiance contribution functions – normalized to the total radiance – at a number of UV wavelengths, for a cloud-free atmosphere. From *Bhartia and Wellemeyer* (2002).

In Fig. 1.4, examples of RCFs normalized to the total radiance at a number of UV wavelengths are shown.

1.3.7 Effects of the Earth's surface

In the previous section, we have shown a simple model that relates the spectral radiance measured by a satellite instrument in UV to the atmospheric state. This model neglects the effects of surface, clouds and aerosols. Here, we discuss the effects of these factors on TOA radiances.

As seen in Section 1.2.2, surface properties provide the boundary condition for the formal solution of the RTE – given by Eq. (1.17) – in the case of a downward-looking instrument. While surface effects are unimportant at wavelengths shorter than about 310 nm, where the strong absorption by ozone prevents the solar radiation from reaching the surface, they start to become relevant at longer UV wavelengths. In general, most natural surfaces have quite low reflectances in the UV. Important exceptions are snow

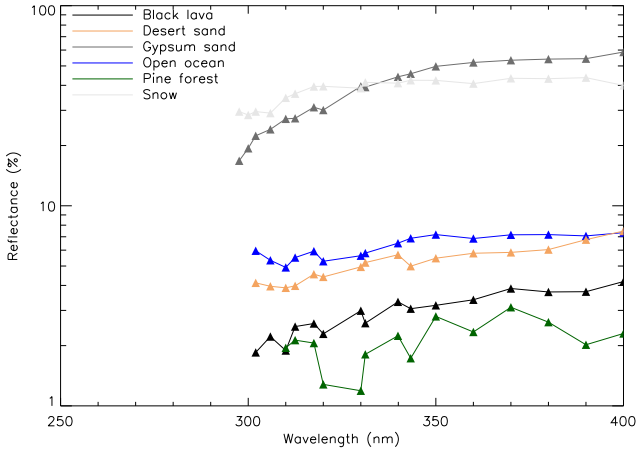

Figure 1.5: Examples of ultraviolet reflectance spectra for six types of surfaces. Data are taken from *Doda and Green* (1980a,b).

and ice, as well as some types of sands. Surface reflectance can have a large influence on the vertical sensitivity of satellite measurements. For example, satellite measurements over bright surfaces have an enhanced sensitivity to the troposphere (*Hudson et al.*, 1995; *Valks et al.*, 2003).

Doda and Green (1980a,b) analysed the UV spectral reflectance of various types of natural surfaces, as measured from an aircraft platform. They applied a linear extrapolation method to remove Rayleigh scattering and atmospheric absorption effects from the measured reflectance spectra, thereby obtaining an estimate for the surface reflectance spectra. Examples of reflectance spectra for six different surfaces are shown in Fig. 1.5. Other plots of UV reflectance spectra can be found in *Verhoeven and Schmitt* (2010).

More complete climatologies of the UV surface reflectance have been created using satellite data. Strictly speaking, the reflective properties of natural surfaces should be described in terms of their Bidirectional Reflectance Distribution Function (BRDF), that specifies the angular distribution of the reflected intensity given the angle of incidence of the incident intensity. However, given the large pixel sizes of most satellite atmospheric sounders, it is often acceptable to assume that the surface is a Lambertian reflector, i.e. that its reflectance is independent on the reflection angle. In view of this, the Earth surface is often characterized by means of its Lambertian

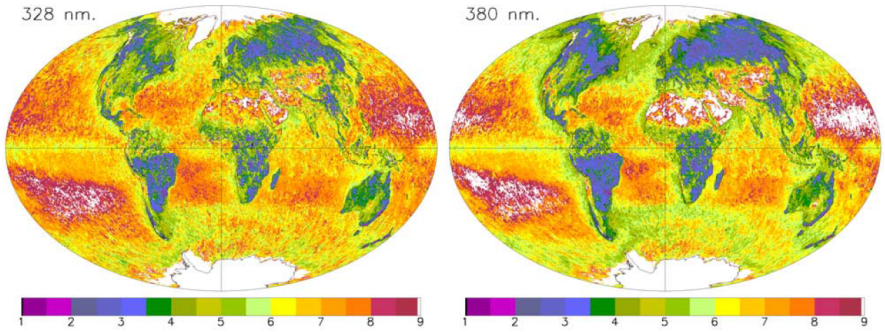

Figure 1.6: Minimum Lambertian Equivalent Reflectivity (MLER) of the Earth's surface at 328 and 380 nm as obtained from OMI data. From *Kleipool et al.* (2008).

Equivalent Reflectance (LER), defined as (*Kleipool et al.*, 2008)

$$\mathrm{LER} = \frac{R - R_0}{\mathcal{T}(\mu)\mathcal{T}(\mu_\odot) + s^*(R - R_0)} \tag{1.52}$$

where R is the TOA reflectance, R_0 is the atmospheric reflectance, $\mathcal{T}(\mu) = \exp(-\tau/\mu)$ is the atmospheric transmittance and s^* is the surface spherical albedo.

Herman and Celarier (1997) compiled a monthly climatology of the UV Earth reflectance by using Total Ozone Mapping Spectrometer (TOMS) data. They showed that the land has generally a lower reflectance than the oceans. *Koelemeijer et al.* (2003) used more than 5 years of GOME observations to compile a seasonally dependent database of the Earth's surface reflectivity from the UV to the NIR spectral range. A similar work was made for OMI by *Kleipool et al.* (2008) between 328 and 500 nm. Figure 1.6 shows global maps of the Minimum Lambertian Equivalent Reflectance (MLER) – i.e., the minimum LER observed during a given period (month, season, year, multi-year) – at 328 and 380 nm, estimated from OMI data. It can be seen that, apart from snow and ice and desertic areas, the reflectance of the land is much lower than that of the oceans. The spatial features in the ocean UV reflectance are mostly due to the phytoplankton distribution.

1.3.8 Effects of atmospheric aerosols

Aerosols affect UV radiances through scattering and absorption. The scattering properties of aerosols are mainly controlled by their shape and size

distribution, whereas their absorption properties depend on their chemical composition, that determines their complex refractive index. The effects of the atmospheric aerosols on UV satellite radiance measurements are highly dependent on the aerosol chemical and physical properties, their height, as well as the Earth's surface properties. An additional complication is due to the fact that some classes of aerosols are hygroscopic, i.e. their particle sizes increase with relative humidity.

The absorption and scattering properties of atmospheric aerosols have generally a weak wavelength dependence, that can be often approximated with a low order polynomial. A comprehensive review of the effects of aerosols on satellite UV measurements can be found in *Torres et al.* (1998). They analysed the difference between simulated reflectance spectra in presence of aerosol and reflectance spectra that would be measured in a purely molecular atmosphere, under different sets of assumptions about aerosol and surface properties. They found out that over dark sufaces, non-absorbing and weakly absorbing aerosols (e.g. sulphate, sea salt) generally cause a net increase in the TOA radiances with respect to what would be measured in a Rayleigh atmosphere, whereas strongly absorbing aerosols (e.g. carbonaceous aerosols) cause the radiance to decrease. Over bright surfaces, instead, non-absorbing aerosols have only a slightly positive effect, because their scattering does not add too much radiation to the background provided by the surface. On the other hand, highly absorbing aerosols can cause a strong decrease in the measured radiances.

1.3.9 Effects of clouds

Since clouds consist of particles whose typical dimensions are much larger than UV wavelengths, such particles mainly behave as Mie scatterers. Therefore, their radiative properties do not have a pronounced spectral dependence.

In view of the discussion made in Sect. 1.3.6, the effect of clouds on satellite radiances becomes important in the longer part of the UV spectrum. However, the wavelength where this effect starts to appear also depends on the cloud height and on the ozone profile. In order to give a visual idea of the sensitivity of UV measurements to clouds, it is interesting to look at Fig. 1.7, showing global reflectance mosaics obtained from OMI data on 25 October 2006 at 300, 305 and 310 nm. 300 nm is a rather short wavelength, where the ozone absorption is considerable (see Sect. 1.3.6). Therefore the cloud structures in the satellite reflectance field are not very sharp, except a clearly cloudy area that can be observed over the Antarctic ocean near the

Antarctica, and some small structures that appear in the intertropical belt. The cloudy structure over Antarctica is clearly visible at this short wavelength because of the ozone hole. The low stratospheric ozone concentrations reduce the absorption along the satellite line of sight, thereby allowing more solar radiation to penetrate the troposphere and more reflected radiation to reach the satellite. As a confirmation of this interpretation, it is interesting to look at the total ozone field retrieved by OMI on the same date, shown in Fig. 1.8: the position of the ozone hole matches very well with the position of the cloud structure seen in the above panel of Fig. 1.7. The small cloud structures seen between the tropics are probably due to high convective clouds, whose tops can reach altitudes close to the tropopopause, that in the tropics can be as high as 18-20 km.

As long as the wavelength increases, the cloud structures become more and more sharp in the reflectance images, and at 310 nm the cloud pattern in the reflectance image is quite similar to what would have been observed at longer (e.g. visible) wavelengths, except, perhaps, in the high ozone areas between Alaska and east Siberia, and over the south-midlatitude Pacific Ocean (see Fig. 1.8), where the high ozone absorption seems to cause some dark "halos" in the reflectances.

A more particular type of clouds is represented by the polar mesospheric clouds (PMCs), or noctilucent clouds. These clouds stand above the ozone layer, and therefore are visible at very short UV wavelengths. Figure 1.9 shows a series of noctilucent cloud images produced by the OMI instrument at 267 nm.

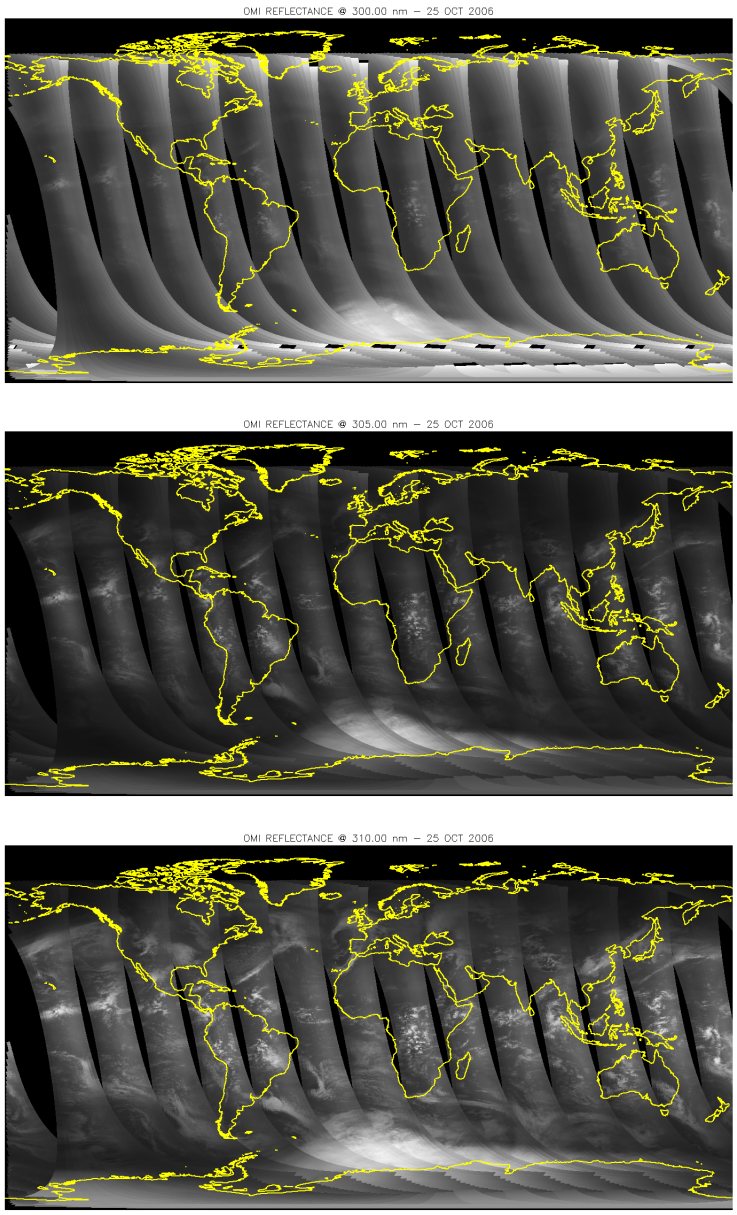

Figure 1.7: OMI global reflectance images at 300, 305 and 310 nm, taken on 25 October 2006.

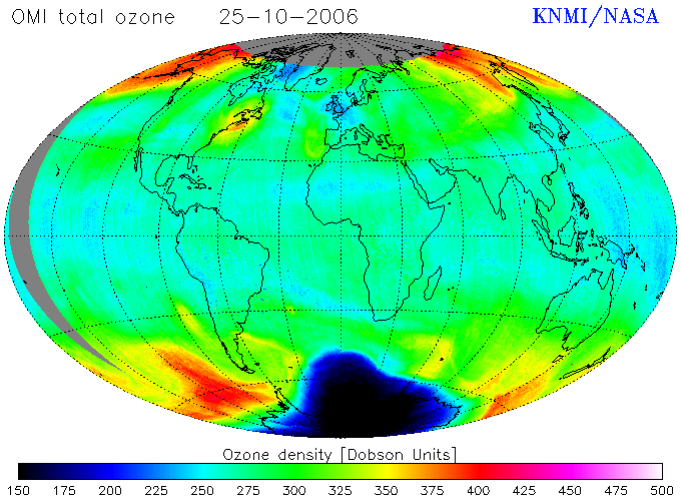

Figure 1.8: Global ozone column field on 25 October 2006 obtained using the OMI-DOAS total ozone product (OMDOAO3). From the Tropospheric Emission Monitoring Internet Service (TEMIS) website (www.temis.nl).

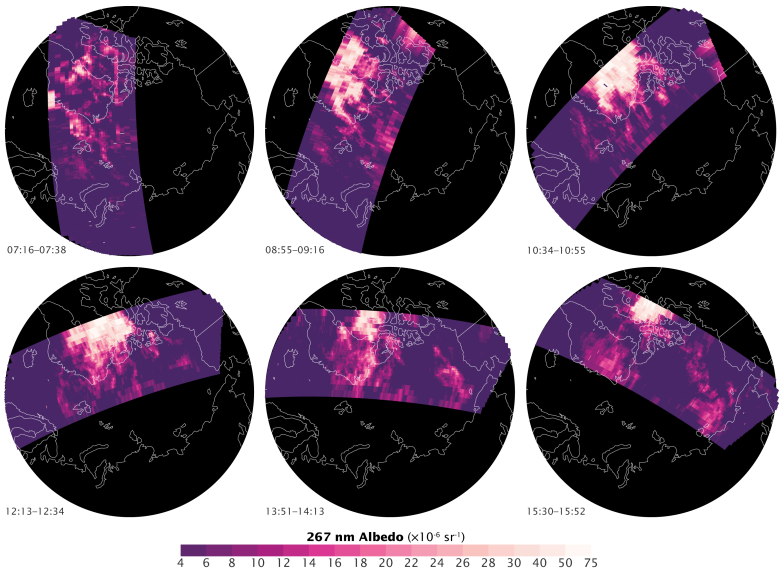

Figure 1.9: Noctilucent clouds observed by OMI at 267 nm. From the NASA Earth Observatory webpage (earthobservatory.nasa.gov).

1.4 Retrieval techniques

1.4.1 Statement of the problem

In the context of atmospheric remote sensing, a retrieval problem essentially consists in recovering the value of an atmospheric quantity (state) $\mathbf{x}$ from a set of radiometric measurements $\mathbf{y}$. Such problems are usually ill-posed, i.e. they cannot be solved by simply inverting a physical model of the measurements, because the relationship between $\mathbf{x}$ and $\mathbf{y}$ is not bijective (*Twomey*, 1977; *Tikhonov and Arsenin*, 1977). In other words, simply solving with respect to $\mathbf{x}$ an equation of the kind

$$\mathbf{y} = \mathbf{F}(\mathbf{x}, \mathbf{b}) \tag{1.53}$$

where the function $\mathbf{F}$ represents the physics of the measurement process and $\mathbf{b}$ is a fixed vector of model parameters (i.e. quantities different from $\mathbf{x}$ that affect $\mathbf{y}$), would not lead to an unique solution for $\mathbf{x}$, even in the case of noise free measurements. Instead, a space of possible solutions for $\mathbf{x}$ would be compatible with a single measurement vector $\mathbf{y}$. This happens because of two concurrent reasons: i) the elements of the measurement vector $\mathbf{y}$ are not mutually independent; ii) the existence of measurement errors usually leads to unstable solutions of the retrieval problem.

Therefore, the aim of a retrieval algorithm is to select, among a set of possible solutions for the state $\mathbf{x}$, an "optimal" solution that is used as an estimator for the true state $\mathbf{x}$.

1.4.2 Variational techinques

In the variational approach to the retrieval problem, the solution chosen as an estimator for $\mathbf{x}$ is the one that minimizes a cost function $\mathcal{C}$ depending on: (i) the discrepancy between the vector of observations $\mathbf{y}$ and a vector $\mathbf{y}_{\text{sim}}$ of simulated observations created using an assumed state $\mathbf{x}$ as an input for $\mathbf{F}$; (ii) some form of prior knowledge about the state to be retrieved.

Based on what kind of prior knowledge is used, we can distinguish to main classes of variational techniques: regularization and Optimal Estimation (OE).

Regularization consists in a least mean square estimate, where the difference between actual measurements $\mathbf{y}$ and predicted measurements $\mathbf{F}(\mathbf{x}, \mathbf{b})$ is minimized with respect to $\mathbf{x}$ with an arbitrary constraint $q(\mathbf{x})$ measuring the degree of "smoothness" of the solution. Several choices can be made for $q(\mathbf{x})$ – see, e.g., *Doicu et al.* (2010a) – and the cost function to be minimized

has the form

$$\mathcal{C}_{\text{reg}} = \|\mathbf{y} - \mathbf{F}(\mathbf{x}, \mathbf{b})\|^2 + \gamma q(\mathbf{x}), \tag{1.54}$$

where γ is a multiplicative term that weights the importance of the constraint with respect to the difference between actual and predicted observations. Of course, setting $\gamma = 0$ would mean not to use any constraint, and setting $\gamma \to \infty$ would be equivalent to ignoring the measurements. One popular form of the regularization constraint is $\mathbf{x}^T\mathbf{H}\mathbf{x}$, where $\mathbf{H}$ is a smoothing matrix.

In the OE approach (*Rodgers*, 2000), assumptions are made about the statistical properties of the state $\mathbf{x}$ to be retrieved and the measurement error ϵ. It is often assumed that both quantities follow Gaussian statistics, with mean values $\mathbf{x}_a$ and $\mathbf{0}$, and covariance matrices $\mathbf{S}_a$ and $\mathbf{S}_\epsilon$, respectively. A model of the measurement process $\mathbf{F}$ is used to transform the Probability Density Function (PDF) of $\mathbf{x}$ into the conditional PDF $P_{y|x}(\mathbf{y}|\mathbf{x})$. Then, an *a posteriori* PDF $P_{x|y}(\mathbf{x}|\mathbf{y})$ is obtained according to the classical Bayesian theory, and it is maximized with respect to $\mathbf{x}$ to yield a parametric estimator for $\mathbf{x}$, the term "parametric" being used to indicate that a specific form for the PDFs and their parameters is assumed for the optimality condition to hold. The general form for the OE cost function to be minimized, under the assumption of Gaussian statistics, is

$$\mathcal{C}_{\text{OE}} = -2\ln P_{x|y}(\mathbf{x}|\mathbf{y}) = [\mathbf{y}-\mathbf{F}(\mathbf{x},\mathbf{b})]^T\mathbf{S}_\epsilon^{-1}[\mathbf{y}-\mathbf{F}(\mathbf{x},\mathbf{b})]+(\mathbf{x}-\mathbf{x}_a)^T\mathbf{S}_a(\mathbf{x}-\mathbf{x}_a). \tag{1.55}$$

The subscripts $y|x$ and $x|y$ are used here to distinguish between the functional forms of the two PDFs.

Since $\mathbf{F}$ is a nonlinear function in most of the practical cases, its minimization is usually performed through iterative methods, such as Gauss-Newton or Levenberg-Marquardt (more details in *Rodgers*, 2000).

1.4.3 Neural network techniques

1.4.3.1 Basic concepts and terminology

NNs can be considered as algorithms for nonlinear regression and function approximation. Although several types of NNs can be devised, they share a number of common characteristics: i) the computation is distributed among elementary units (called neurons); ii) the relationship to be approximated is learned by the NN from a training dataset.

Mathematically, it can be said that a NN can be used to approximate an unknown relationship between two quantities $\mathbf{x} \in \mathbb{R}^n$ and $\mathbf{y} \in \mathbb{R}^m$ through

a nonlinear model $\Phi_{\mathbf{W}}$, such that

$$\mathbf{y} = \Phi_{\mathbf{W}}(\mathbf{x}) \tag{1.56}$$

where $\mathbf{W}$ is a set of free parameters to be adjusted from a training dataset. In the case of supervised training, which is the only relevant case for the purposes of this work, the training dataset is made of pairs $\{(\mathbf{x}_i, \mathbf{y}_i)\}$ of instances of the relationship to be approximated. The adjustment of the free parameters is made according to a learning algorithm, that basically consists of an iterative minimization of an error cost function of the kind

$$\mathcal{C} = f(\|\mathbf{y}_i - \Phi_{\mathbf{W}}(\mathbf{x}_i)\|), \tag{1.57}$$

with respect to $\mathbf{W}$. According to the exact definition of the cost function and to the choice of the iterative method chosen for its minimization, several learning algorithms can be defined. The reader can refer to *Bishop* (1995a) or *Haykin* (1999) for more detailed information.

1.4.3.2 Multilayer perceptrons

The Multilayer Perceptron (MLP) network (*Werbos*, 1974) is one of the most widespread NN architectures. Each neuron of a MLP realizes the input-output relationship

$$y = \varphi(\mathbf{w}^T\mathbf{x} + b) \tag{1.58}$$

where $\mathbf{w}$ and b are the weight vector and the bias of the neuron, respectively, and are its free parameters to be adjusted, and the function φ, chosen in advance, is the activation function of the neuron.

The neurons of a MLP are organized in layers: i) an input layer, that simply contains the input vector of the MLP; ii) at least one hidden layer, containing neurons with nonlinear activation functions; and iii) an output layer, whose neurons can either have linear or nonlinear activation functions and yield the output of the MLP. The output of each layer is the input for the next layer.

One reason for the popularity of MLPs among supervised NN techniques is their universal approximation capability: several studies have independently shown that, under rather general conditions, every continuous function on a compact set can be approximated to whatever accuracy by a MLP having only one hidden layer (*Cybenko*, 1989; *Funahashi*, 1989; *Hornik et al.*, 1989). However, it must be pointed out that the universal approximation

theorems only prescribe the existence of an approximating NN, but they do not indicate how such NN can be found in practice.

Since the MLP is the only relevant architecture in the context of this work, the terms MLP and NN will be used without distinction from here onwards.

The approximation properties of NNs makes them useful in remote sensing applications, where either forward or inverse problems have to be solved. In particular, NNs have been successfully used in various applications of satellite atmospheric remote sensing, such as temperature and humidity profile retrievals from microwave and infrared observations (*Aires et al.*, 2001; *Blackwell*, 2005), ozone retrievals from UV/VIS radiances (*Del Frate et al.*, 2002, 2005a,b; *Müller et al.*, 2002, 2003; *Iapaolo et al.*, 2007; *Sellitto et al.*, 2011, 2012a) and radiative transfer calculations (*Chevallier et al.*, 1998, 2000; *Schwander et al.*, 2001; *Göttsche and Olesen*, 2002; *Krasnopolsky and Schiller*, 2003; *Krasnopolsky and Chevallier*, 2003).

1.4.3.3 Neural networks in retrieval problems

NN retrievals can be regarded as a nonparametric alternative to OE. The training set for a NN to be used in a retrieval algorithm consists of pairs $\{(\mathbf{y}'_i; \mathbf{x}_i)\}$, where the vector $\mathbf{y}'_i$ includes the measurements $\mathbf{y}_i$ and any other parameter that is used as an input for the algorithm (e.g. geometrical parameters, ancillary data), and the $\mathbf{x}_i$ includes the quantities to be retrieved. The training set can be seen as a set of samples drawn from the PDF $P(\mathbf{x}|\mathbf{y}')$. These samples are used to adjust the parameters of a model of the same kind as Eq. (1.56), minimizing a cost function similar to Eq. (1.57). Once the training is complete, a global retrieval model

$$\hat{\mathbf{x}} = \Phi_{\mathbf{W}^*}(\mathbf{y}'), \tag{1.59}$$

is constructed, where $\mathbf{W}^*$ is the value of $\mathbf{W}$ determined at the end of the training process. This retrieval model yields a nonparametric estimator for $\mathbf{x}$ – here denoted by $\hat{\mathbf{x}}$ – meaning that no assumptions about the statistical distribution of $\mathbf{x}$ are made to specify the model. The "global" adjective refers to the fact that, once the training phase is complete, the resulting function $\Phi_{\mathbf{W}^*}$ can be applied to *every* observation in order to obtain the retrieval. This is a difference between NNs and the aforementioned retrieval techniques, where the cost function has to be minimized for *each* observation.

NN retrieval algorithms have a number of advantages over other methods: i) when the training set consists of real data, the absence of explicit modeling makes the retrieval insensitive to an incomplete knowledge of the

measurement physics; ii) the absence of assumptions about the statistical distribution of the quantity to be retrieved makes NNs robust to non-Gaussianity of the modeled processes (*Blackwell and Chen*, 2009); and iii) NN retrieval schemes are fast and relatively easy to implement. However, NNs have also some disadvantages: i) when they are trained on real data, the quality of such data is critical for the learning process; ii) they are good interpolators, but may yield unpredictable results when forced to extrapolate (*Krasnopolsky and Schiller*, 2003); and iii) NNs are *not* optimal estimators, the training process depends on random initialization of the NN parameters and may be trapped in local minima of the cost function to be minimized. Nevertheless, these shortcomings can often be handled with proper design and data quality control procedures. A more subtle shortcoming is that, since the NN training requires the minimization of a global cost function, it is possible that the cost function associated with a single observation could be better minimized with the conventional retrieval techniques.

A debated issue regarding the application of NNs to retrieval problems is the error propagation. A general review of the predictive uncertainty estimation methods for NNs is given by *Dybowski and Roberts* (2009). *Aires et al.* (2004a,b) suggest a method to define an error budget for NN retrievals that resembles that developed by *Rodgers* (1990) for the classical retrieval techniques. Specifically, *Aires et al.* (2004a) express the error covariance matrix of the retrieval as the sum of a "neural inversion" term, accounting for the effect of the suboptimalities in the NN architecture, the learning process and the training dataset, and an "intrinsic noise" term, accounting for all the other possible sources of error. However, this formulation makes it difficult to isolate sources like the null space error, that is important in order to assess the vertical resolution of a retrieval algorithm.

1.4.3.4 Neural network design principles

NN models have a relatively large number of free parameters. Some of these parameters – i.e. weights and biases – are determined during the training process, others – i.e. the activation functions, the number of hidden layers and neurons, the learning algorithm and its internal parameters – must be chosen by the designer. While it would be impossible to discuss every aspect of the design of a NN inside this paper (the interested reader is again referred to *Bishop* (1995a) or *Haykin* (1999) for a comprehensive discussion of the heuristics that can be followed), it might be worthwhile to discuss some of the most important design aspects, as this should clarify the reasons for some of the choices that were made during the development of the ozone

retrieval algorithms that are the main subject of this thesis.

The most critical design issues to be addressed during the development of a NN are the choice number of hidden layers and neurons to be used, and the choice of when to stop the training process.

As for the number of hidden layers and units, there are no universally valid rules, but heuristic methods must be used. Such methods basically consist in comparing different NN architectures on a common reference dataset, and selecting the architecture that achieves the best score in terms of some performance metric. The most elementary metric that may be used is simply the Mean Squared Error (MSE) over the reference set. Other metrics, like the Akaike Information Criterion (AIC) (*Akaike*, 1973), combine the MSE with penalty terms for an excessive number of hidden neurons.

One or two hidden layers are often enough for a good NN model (*Kecman*, 2001). A thumb rule that can be kept in mind in the selection of the number of hidden units is the *bias-variance dilemma* (*Geman et al.*, 1992). According to this rule, NNs with too few hidden nodes tend to have poor approximation capabilities (large bias, or underfitting), whereas NNs with too many hidden nodes are prone to bad generalization, i.e. poor performances on data that were not seen during the training process (large variance, or overfitting). Therefore, the right choice for the number of hidden units must result from a trade-off between these two extremes.

Another crucial point is to decide when to stop the training of a NN. Although common sense criteria can be easily formulated to decide whether a learning algorithm has converged on a given training set (a typical approach is to fix a certain threshold on the decrease in MSE between two successive iterations of the algorithm, and to decide that the algorithm has converged if such decrease remains below the threshold for a certain number of iterations), it is often not advisable to continue the training process until a convergence criterion is met. In fact, as long as the training proceeds, there is the danger that the NN ends up memorizing the training data, reaching extremely low values of the MSE on the training data but producing very poor results over data that are not included in the training set. This condition is named *overtraining*, or *overfitting*. In order to prevent this, the performances of the NN over an independent set should always be monitored during the training process, and the training should be stopped when a significant degradation in the NN performances over this set is observed. This method is called *early stopping cross-validation* (*Haykin*, 1999).

Chapter 2

Validation of the OMI-TOC NN tropospheric ozone column retrieval algorithm with ozone soundings over Europe

Parts of this chapter are extracted from the following paper:

Di Noia, A., P. Sellitto, F. Del Frate, M. Cervino, M. Iarlori and V. Rizi (2013), "Tropospheric ozone column retrieval from OMI data by means of neural networks: A validation exercise with ozone soundings over Europe", *Eurasip J. Adv. Sig. Pr.*, 2013, 21, doi:10.1186/1687-6180-2013-21.

2.1 Introduction

Tropospheric ozone is a key player in a number of atmospheric processes which affect both climate and air quality. Its climatic impact is expressed by a radiative forcing of about 0.35 W/m^2, as estimated by the Intergovernmental Panel on Climate Change (IPCC) fourth assessment report (*IPCC*, 2007). Such radiative forcing makes tropospheric ozone the fourth atmospheric greenhouse gas by importance, following water vapour, carbon dioxide and methane (*IPCC*, 2007). As for the air quality, tropospheric ozone has both a positive and a negative role; its positive role lies in the fact that

it acts as a precursor of the idroxyl radical, which is able to remove several pollutants from the middle troposphere through oxidation reactions (*Jacob*, 1999); its negative role lies in its toxicity for both humans and crops when it reaches high concentrations near the Earth's surface (*Anenberg et al.*, 2009; *Booker et al.*, 2009; *Fishman et al.*, 2010).

Monitoring the concentration of tropospheric ozone from a satellite platform offers the advantage of a temporally and spatially continuous observation, allowing the identification of long-range transport processes (*Creilson et al.*, 2003, 2005), and the generation of temporally extended records, that are useful for the investigation of long term trends (*Kim and Newchurch*, 1996; *Valks et al.*, 2003; *Fishman et al.*, 2005).

In the last two decades, the advent of a new generation of satellite hyperspectral atmospheric sounders, which make simultaneous radiance measurements with high spectral resolution and sampling rate, covering the ultraviolet (UV), visible (VIS) and infrared (IR) spectral ranges, has greatly enhanced our capability to detect and quantify several tropospheric trace gases, including ozone (*Burrows et al.*, 2011b).

Among the tropospheric gases that can be monitored from space, ozone is one of the most problematic ones. In fact, the contribution of tropospheric ozone to the measured radiance signal must be separated from the contribution of stratospheric ozone, which is much larger, due to the fact that most of the atmospheric ozone is found in the stratosphere. In order to accomplish this, several techniques were developed during the last 20 years. The rationale behind the first tropospheric ozone retrieval algorithms was to isolate the stratospheric ozone column by means of limb measurements (*Fishman et al.*, 1990; *Schoeberl et al.*, 2007) or total ozone retrievals over high-altitude clouds (*Ziemke et al.*, 1998, 2001), and then subtract it from a co-located or neighboring measurement of the total ozone column. In the case of limb measurements, the separation between stratosphere and the troposphere is achieved thanks to the limb viewing geometry, whose line of sight does not encounter the atmospheric layers located beneath the upper troposphere/lower stratosphere (UTLS). In the case of measurements over high clouds, it is assumed that such clouds shield the underlying troposphere, and that the stratospheric ozone field does not have a significant horizontal variability within a certain number of neighboring pixels. If these assumptions hold true, it is possible to say that total ozone column retrievals over high altitude clouds actually represent stratospheric columns, which can be subtracted from total ozone columns retrieved over neighboring clear-sky pixels to yield an approximated value for the tropospheric ozone column. This type of approach has been mainly used over the Tropics, where high

convective clouds are more frequent.

During the last decade, the improved sensitivity to the lower tropospheric layers that was achieved with new satellite instruments – including the Global Ozone Monitoring Experiment (GOME), the SCanning Imaging Absorption spectroMeter for Atmospheric CHartographY (SCIAMACHY) and the Ozone Monitoring Instrument (OMI) – has enabled the development of algorithms which directly derive tropospheric ozone information from ozone profiles retrieved through an Optimal Estimation (OE) scheme (*Munro et al.*, 1998; *Liu et al.*, 2005, 2006, 2010).

OE retrieval schemes make use of forward Radiative Transfer Models (RTMs), that are computationally intensive and require a consistent characterization of the whole atmospheric state, including the properties of clouds, aerosols and spectrally interfering trace gases (i.e. gases which have absorption features in the same spectral region as the trace gas of interest), which in most cases must be assumed *a priori*. This can cause the retrieval process to be slow and sensitive to wrong *a priori* assumptions, as well as to forward modeling errors (*Rodgers*, 2000).

An alternative approach to the direct determination of tropospheric ozone from satellite measurements is represented by Neural Network (NN) algorithms. Instead of explicitly using a forward model, NNs attempt to approximate the relationship between the measured radiance and the atmospheric parameter of interest directly by means of a nonlinear regression on a given training set (*Bishop*, 1995a). In the case of atmospheric retrievals, the training set for a NN algorithm will consist of simultaneous realizations of the radiometric measurements and the geophysical process of interest. In addition, other parameters that can be useful to better constrain the relationship between the radiance measurements and the parameter to be retrieved (e.g. information on the observation geometry, other atmospheric parameters) can be given as inputs to a NN. For the training of a NN to be successful, a large and comprehensive training set must be built, possibly covering all the atmospheric situations that can be encountered in reality (e.g. heavy pollution events, tropopause folds).

Although the training process can be slow, a trained NN is able to operate very quickly, which is an attractive feature for operational retrievals. Furthermore, NNs allow to handle heterogeneous data in an easy way (*Westwater*, 2003). This is an important feature when a complex model relating a large number of different quantities (e.g. atmospheric optical thickness, tropopause height and tropospheric ozone column) cannot be explicitly formulated, although it is known that a physical correlation between these quantities exists. On the other hand, a disadvantage of NNs lies in the diffi-

cult interpretation of their results. Such difficulty arises from the fact that the physical relationships underlying the retrieval process are represented by a NN in a purely numerical form, without any reference to the causal relationships that link the observed data. Because of this, NN retrieval schemes do not provide diagnostics that measure the relative contribution of each atmospheric layer to the retrievals and the number of independent pieces of information provided by the algorithm – such as the averaging kernels and the degrees of freedom for signal (DFS) (*Rodgers*, 2000) – whose computation requires an RTM.

NNs have been successfully applied in several branches of atmospheric remote sensing (*Blackwell and Chen*, 2009), including retrievals of ozone profiles (*Del Frate et al.*, 2002; *Müller et al.*, 2003), total ozone (*Müller et al.*, 2002) and tropospheric ozone column (*Sellitto et al.*, 2007, 2011, 2012a). Recently, a new NN algorithm for tropospheric ozone retrieval over the northern mid-latitudes from OMI data – named OMI-TOC NN (OMI Tropospheric Ozone Column Neural Network) – has been proposed (*Sellitto et al.*, 2011). In this chapter, the results of a validation of this latter algorithm with ozone soundings performed at a number of European stations are presented.

This chapter is organized as follows. In Section 2.2 a brief overview of the NASA Aura-OMI mission is given. In Section 2.3 a description of the OMI-TOC NN algorithm is given. In Section 2.4 the ozonesonde sites used for this validation and the co-location criteria are described. In Section 2.5 the validation results are shown, the temporal trends in the retrieval errors are discussed, and the importance of a parameter which was not originally used in the NN input vector – namely, the tropopause pressure – is demonstrated. In Section 2.6, it is shown that the inclusion of the tropopause pressure in the input vector of the NN improves its retrieval capabilities in case of low tropopauses. The conclusions are drawn in Section 2.7.

2.2 The NASA-Aura mission and the OMI instrument

The NASA EOS Aura mission (*Schoeberl et al.*, 2006), started in 2004 with the launch of the homonymous satellite, aims at the study of the atmospheric composition, chemistry and dynamics. The scientific instrumentation onboard the Aura satellite includes the OMI instrument, as well as the Tropospheric Emission Spectrometer (TES), the Microwave Limb Sounder (MLS) and the HIgh Resolution Dynamics Limb Sounder (HIRDLS).

The OMI instrument (*Levelt et al.*, 2006b) is a nadir UV/VIS imag-

ing spectrometer, that measures direct and backscattered solar radiation in three channels; namely, the UV1 channel (270–310 nm), the UV2 channel (310–365 nm) and the VIS channel (365–500 nm). The UV1 and UV2 channels are the most important ones for ozone monitoring, because they cover the Hartley and Huggins absorption bands of the ozone molecule. The VIS channel is used for observations of clouds, aerosols and other atmospheric trace gases (e.g. nitrogen dioxide, formaldehyde). However, it does not cover the most absorbed part of the ozone Chappuis absorption bands (i.e. about 530-610 nm). Therefore, this channel cannot be directly exploited in ozone retrievals.

OMI can observe the Earth's atmosphere in three observation modes. In the main mode – called the Global measurement mode – OMI has a swath width of 2600 km, a nadir pixel size of 13×48 km^2 (along- $\times$ across-track) for the UV1 channel and 13×24 km^2 for the UV2 and VIS channels. The pixel size increases in the swath direction for increasing distances from the satellite ground track. The OMI average spectral resolution is of about 0.4 nm in the UV1 and UV2 channels and about 0.6 nm in the VIS channel. The OMI Global measurement mode provides almost global coverage in one day. In principle, a complete daily global coverage is possible at midlatitudes. However, a complex instrumental effect, called *row anomaly* – which started to appear in the Level 1B data on June 25th of 2007 – creates some gaps in the instrumental coverage. More information on this effect is available from the Royal Dutch Meteorological Institute (KNMI – Koninklijk Nederlands Meteorologisch Instituut) website (www.knmi.nl/omi/research/product/rowanomaly-background.php).

In addition to the Global mode, two so-called "zoom-in" observation modes are available. In both modes the nadir pixel size is reduced to 13×12 km^2. In the Spatial zoom-in mode the pixel size is reduced at the expense of the swath width, which decreases to 725 km; in the Spectral zoom-in mode the reduction comes at the expense of the wavelength range, which is limited to 306–432 nm (*Levelt et al.*, 2006b). Zoom-in observations are only performed during selected orbits.

2.3 The OMI-TOC NN algorithm

Recently, a NN algorithm for tropospheric ozone column retrieval from OMI reflectance measurements has been proposed (*Sellitto et al.*, 2011). Hereinafter, this algorithm will be referred to as OMI-TOC NN. The design and optimization stages of the algorithm are thoroughly discussed in (*Sellitto*

Table 2.1: Summary of the stations used in the training set of the OMI-TOC NN. After *Sellitto et al.* (2011).

Station	Country	Latitude	Longitude	N. co-locations
Barajas (Madrid)	Spain	40.46°N	3.65°W	107
Boulder	United States	40.09°N	105.25°W	95
Bratt's Lake	Canada	50.21°N	104.71°W	108
Churchill	Canada	58.75°N	94.07°W	91
Egbert	Canada	44.23°N	79.78°W	103
Goose Bay	Canada	53.30°N	60.36°W	126
Hohenpeissenberg	Germany	47.80°N	11.02°E	360
Huntsville	United States	34.72°N	86.64°W	82
Isfahan	Iran	32.48°N	51.43°E	36
Kelowna	Canada	49.93°N	119.40°W	116
Legionowo	Poland	52.40°N	20.97°E	179
Lindenberg	Germany	52.21°N	14.12°E	161
Payerne	Switzerland	46.69°N	6.57°E	463
Sapporo	Japan	43.06°N	141.33°E	117
Tateno	Japan	36.06°N	140.10°E	120
Trinidad Head	United States	40.80°N	124.16°W	57
Uccle	Belgium	50.80°N	4.35°E	390
Wallops Island	United States	37.89°N	75.48°W	57

et al., 2011). The OMI-TOC NN was trained and tested with an extended set of ozonesonde measurements taken at the northern midlatitudes between 2004 and 2008. The ozonesonde stations whose data were used in the training set are listed in Table 2.1. The OMI-TOC NN performances were found to be comparable, and in some cases slightly better, with respect to those of the Trajectory enhanced Tropospheric Ozone Residual (TTOR) (*Schoeberl et al.*, 2007) and OE (*Liu et al.*, 2006) algorithms over a set of co-located ozonesonde measurements (*Sellitto et al.*, 2011). These results suggest that the OMI-TOC NN is a valuable alternative method for tropospheric ozone retrievals from OMI data.

The input vector for the OMI-TOC NN consists of OMI spectral reflectances at 19 selected wavelengths, extracted from OMI Level 1b data; the Solar Zenith Angle (SZA) and the total ozone column taken from the operational OMI Level 2 product. Only Global measurement mode data were used, because only this observation mode provides daily global cover-

age. The 19 wavelengths were selected according to an Extended Pruning (EP) technique (*Del Frate et al.*, 2005a). This technique aims at reducing the dimensionality of an input vector for a NN by retaining only the most informative inputs, i.e. those who have the strongest influence on the NN output. 6 of the selected wavelengths belong to the 305-307 nm range (covered by the OMI UV1 channel), while the remaining 13 wavelengths lie in the 322-325 nm range (covered by the OMI UV2 channel). The spectroscopic relevance of these two spectral ranges in the context of ozone retrievals is discussed by *Sellitto et al.* (2012a).

The dimensionality reduction of the reflectance spectra is useful for a number of reasons. First, using full spectra would lead to a very big input vector, which would in turn cause a need for a larger training dataset and longer training times. Second, there would be the risk of including irrelevant information in the input vector, which may compromise the learning capabilities of the NN (e.g. by causing overfitting).

In order to homogenize the spatial resolution of the input spectra, the UV2 reflectances were degraded to the spatial resolution of the OMI UV1 channel (see Section 2.2). The resolution degradation was performed through simple arithmetical averages between pairs of adjacent spatial pixels in the across-track direction.

The output quantity for the NN, i.e. the retrieved parameter, is the integrated ozone column between the surface and the 200 hPa pressure level. From now on, the name Tropospheric Ozone Column (TOC) will be used when referring to this quantity. However, it must be pointed out that the choice of a static upper integration limit in the definition of the TOC – regardless of the actual tropopause height – may be inaccurate. The problems that can arise as a consequence of this choice are shown and critically discussed in Section 2.5.

2.4 Validation set and intercomparison methodology

Six European ozonesonde stations were used in the validation of the OMI-TOC NN: Ankara (Turkey), Izaña (Canary Islands, Spain), Lerwick (Shetland Islands, United Kingdom), Valentia Island (Republic of Ireland), L'Aquila and San Pietro Capofiume (Italy). No data from such stations were used during the training of the OMI-TOC NN. Data acquired between October 2004 and December 2008 were considered in this validation exercise. This is the same period that is covered by the training dataset of the OMI-TOC

NN. This choice was made in order to ensure that eventual problems in the algorithm are not caused by instrumental changes that may have occured after the period covered by the training set.

The data for Ankara, Lerwick and Valentia Observatory were taken from the World Ozone and Ultraviolet Data Center (WOUDC) archive. The data for Izaña were taken from the public archive of the Network for the Detection of Atmospheric Composition Change (NDACC).

In addition to the data available from WOUDC and NDACC, data from the two Italian ozonesonde stations of L'Aquila and San Pietro Capofiume were used.

The L'Aquila ozone soundings were performed by the University of L'Aquila and the Centre of Excellence for the integration of remote sensing techniques and modeling for the forecast of severe weather (CETEMPS – Centro di Eccellenza di Telerilevamento e Modellistica numerica per la Previsione di eventi Severi). The ozonesonde station is located at the CETEMPS atmospheric observatory, Casale Calore di San Vittorino (42.3°N, 13.31°E, 683 m a.s.l.), near the town of L'Aquila. The ozonesondes are SPC-6A type Electrochemical Concentration Cell (ECC) sondes (*Komhyr*, 1969; *Johnson et al.*, 2002), interfaced with Vaisala RS-92 PTH (Pressure, Temperature, Humidity) radiosondes.

The ozone sounding activity at L'Aquila is performed within the framework of a collaboration between CETEMPS, L'Aquila University and the Italian Ministry for the Environment and Territory. The first soundings were performed in 1994. Since 2004, about 2 soundings per month have been regularly carried out on average. In the past, L'Aquila ozonesonde data were used in the validation of ozone profiles retrieved by the Michelson Interferometer for Passive Atmospheric Sounding (MIPAS), onboard Envisat (*Rizi et al.*, 2003; *Cortesi et al.*, 2007).

The San Pietro Capofiume ozone soundings were performed under the responsibility of the Italian National Research Council (CNR – Consiglio Nazionale delle Ricerche) Institute for Atmospheric and Climate Sciences (ISAC – Istituto di Scienze dell'Atmosfera e del Clima). The San Pietro Capofiume ozonesondes are ENSCI-Z type ECC sondes, interfaced with Vaisala RS-80 PTH radiosondes.

In the past, ozone soundings were regularly performed at San Pietro Capofiume from 1991 to 1995 (*Banzi et al.*, 1994), and a specific campaign was organized in 1997 (*Giovanelli et al.*, 2004). In 2004 and 2005, a sporadic sounding activity was carried out. However, it was subsequently interrupted due to scarcity of research funds. The data acquired during 2004 and 2005 were used in this work.

Within the above mentioned set of locations, different climatological characteristics are represented. This allows the geographical generalization capabilities of the OMI-TOC NN algorithm to be assessed, even at the upper and lower boundaries of the latitudinal range covered by the training set. Izaña is close to the African continent and not far from the Tropic of Cancer, and thus can be regarded as an hybrid midlatitude/subtropical station, being influenced by air masses coming from both the midlatitudes and the subtropics (*Oltmans et al.*, 2006). Lerwick and Valentia are characterized by an oceanic climate, and are subjected to advections of both midlatitude and polar air masses (*Mariotti et al.*, 1997). Hence, these stations can either behave as polar or midlatitude stations depending on the location of the polar front. Ankara, L'Aquila and San Pietro Capofiume can be regarded as typical midlatitude stations. Furthermore, all the stations are located in geographical areas which are not covered by the training set of the OMI-TOC NN algorithm. For this reason, validating the algorithm over this set of locations can give a reliable insight on its geographical generalization capabilities, as well as on its limitations.

In order to generate the validation set, the same co-location criteria as those used in the development of the OMI-TOC NN algorithm (*Sellitto et al.*, 2011) were followed. Specifically, an ozone sounding and an OMI pixel were considered as co-located if two criteria were met: (i) the nominal coordinates of the ozonesonde station and those of the pixel center were no more than $\pm 1^\circ$ apart; and (ii) no more than 12 hours had elapsed between the ozone sounding and the Aura overpass on the ozonesonde station.

By using these criteria, a total of 808 input-output pairs for validation were created. The number of co-locations obtained for each station is given in Tab. A.1. An exiguous number of co-locations was obtained for San Pietro Capofiume. However, such data have been included in the present study for sake of completeness.

2.5 Validation results

The validation results from October 2004 to December 2008 are shown in the scatter plot in Fig. 2.1. The retrieved TOCs are given an the abscissa, the true TOCs are given as the ordinate. A Root Mean Square Error (RMSE) of 10.21 DU was found. This value is definitely higher than that found in the validation results shown in *Sellitto et al.* (2011), over a different set of ozonesonde stations. Furthermore, from a visual inspection of the scatter plot, it is evident that the algorithm has a systematic tendency to underes-

Table 2.2: Summary of the stations used in the validation presented in this work.

Station	Country	Latitude	Longitude	N. data
Ankara	Turkey	39.95°N	32.85°E	112
Izaña	Spain	28.29°N	16.49°W	227
L'Aquila	Italy	42.38°N	13.31°E	76
Lerwick	United Kingdom	60.13°N	1.18°W	240
San Pietro Capofiume	Italy	44.65°N	11.62°E	12
Valentia Observatory	Republic of Ireland	51.93°N	10.25°W	141

timate tropospheric ozone values larger than about 60 DU and overestimate values smaller than about 25 DU. Some quantitative statistics confirm this impression: 29 out of 33 TOCs larger than 25 DU are overestimated, and 42 out of 48 TOCs larger than 60 DU are underestimated. In order to assess whether this behaviour displays a geographical dependence, the validation results were separately analyzed for each station.

The scatter plots of true versus retrieved TOCs for each ozonesonde station are shown in Fig. 2.2. It can be noted that, whilst the Ankara and L'Aquila scatterplots have a fairly symmetrical shape, the scatter plots for Izaña, Lerwick and Valentia Observatory exhibit a quite pronounced underestimation tendency throughout the whole dynamical range of the TOC values.

One possible reason for the systematic underestimation of TOCs higher than 60 DU lies in the choice of 200 hPa as a static upper integration limit for the retrieved ozone column. In fact, if this TOC definition is used, extreme TOC values can be expected when the actual tropopause pressure exceeds 200 hPa (i.e., when the actual tropopause height is lower than the upper integration limit used in the OMI-TOC NN), because a large portion of stratospheric air – which is very rich in ozone – is included in the column over which the ozone profile is integrated in order to derive TOC. As a result, including the tropopause pressure in the input vector can help the NN discriminate such cases of enhanced TOC, and hence improve the overall retrieval accuracy.

In order to check the correctness of this hypothesis, an analysis of the retrieval error versus the actual tropopause pressure was carried out for each station. The tropopause pressure data were taken from the NCEP/NCAR Reanalysis 1 (*Kalnay et al.*, 1996). Plots representing the retrieval error against the tropopause pressure for each station are shown in Fig. 2.3. A

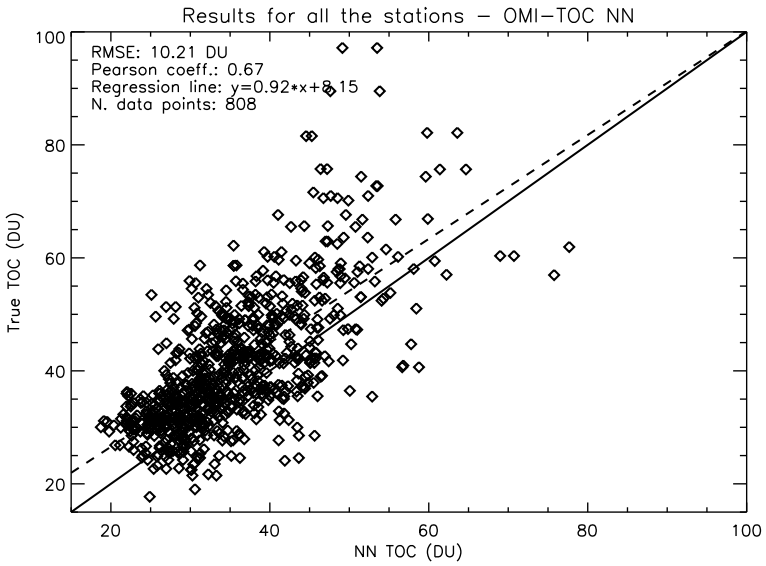

Figure 2.1: Scatter plot of true vs. retrieved TOCs for all the stations considered in this work.

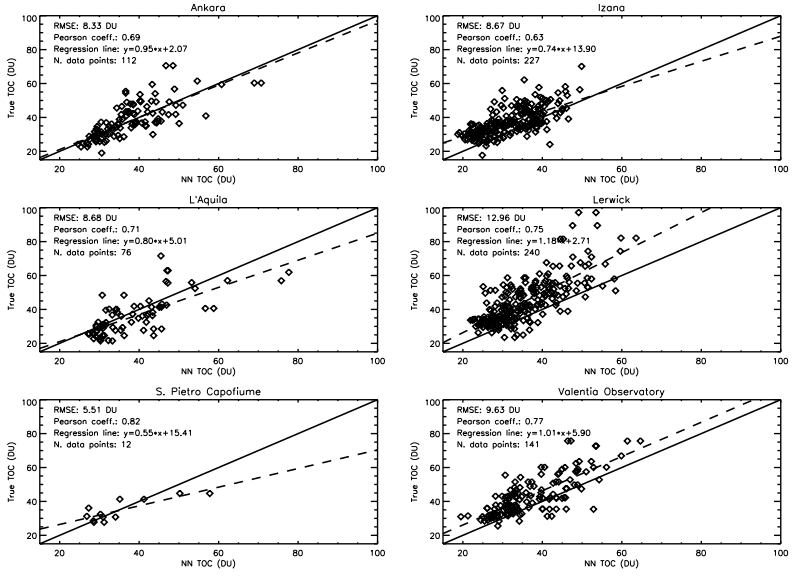

Figure 2.2: Scatter plots of true vs. retrieved TOCs divided by ozonesonde station.

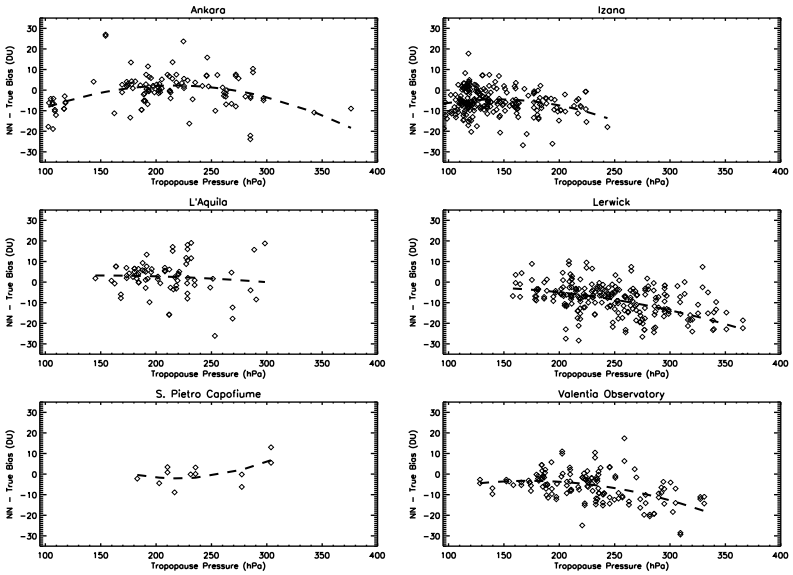

Figure 2.3: TOC retrieval error vs. tropopause pressure for all the ozonesonde stations considered in this work.

trend line, resulting from a quadratic fit of the retrieval error versus the tropopause pressure, is superimposed on each plot. It can be seen that the error trend is particularly clear on Lerwick and Valentia Observatory, where cases of tropopause pressures considerably larger than 200 hPa are most frequent.

2.6 Correction of tropopause related errors

The results shown in Section 2.5 confirm the hypothesis that a relationship between the retrieval accuracy of the OMI-TOC NN and the tropopause pressure exists. Furthermore, they suggest that the use of tropopause information as an input for the algorithm has the potential to enhance the retrieval accuracy. For this reason, a first attempt was made to design a new NN algorithm receiving such information as an input. The OMI Level 1B data were co-located with the NCEP/NCAR tropopause pressure fields in order to generate training, testing and validation sets for the new NN. The same stations used in the OMI-TOC NN were used to train the new NN. A comparison between the two NNs in terms of training, test and validation RMSE is shown in Table 2.3. The standard deviations of the sonde TCOs

Table 2.3: RMSE on training, test and validation sets for the OMI-TOC NN and its modified version.

Dataset	TOC std [DU]	RMSE [DU]	
		OMI-TOC NN	Mod. OMI-TOC NN
Training	11.49	7.43	6.22
Test	11.23	8.03	7.20
Validation	11.83	10.21	8.40

in the three sets are also reported. It can be observed that the new NN has a lower RMSE with respect to the previous one on all the three sets.

The overall results for the set of ozonesonde stations considered in this paper are shown in Fig. 2.4. A significant reduction in the both RMSE and the bias is evident. Particularly significant is the reduction in the underestimation tendency for high values of TCO. Out of the 48 TCOs larger than 60 DU, 25 were found to be underestimated by the modified OMI-TOC NN, in contrast with the 42 underestimations found for the original NN (Section 2.5). In more formal terms, if TOC_{retr} is the retrieved TOC and TOC_{sonde} is the TOC measured by an ozonesonde, we can say that the conditional probability $Prob(TOC_{retr} < 60\,DU | TOC_{sonde} \geq 60\,DU)$ on the validation dataset can be estimated in about 88% for the original OMI-TOC NN described in *Sellitto et al.* (2011) and about 52% for the modified NN proposed in this paper.

Table 2.4 summarizes the performances of both the OMI-TOC NN and its modified version in terms of RMSE and mean bias. Mean and standard deviation of the TOCs measured by the ozonesondes are also reported, in order to facilitate the interpretation of the validation results. The results divided by station are also shown, in form of scatter plots, in Fig. 2.5.

The improvements are evident on Ankara and L'Aquila, and dramatic on Lerwick and Valentia Observatory. Such improvements were not found on Izaña, which still appears to be the most problematic station amongst those shown in this paper. From a visual inspection of the upper right panel of Fig. 2.3, it is evident that the tropopause pressures over Izaña were most often far below 150 hPa (i.e. the tropopause was considerably higher than the corresponding altitude level) with regard to the ozone soundings used in this validation exercise. This suggests that Izaña mostly behaved as a tropical station, and thus portends poor performances of the OMI-TOC NN with air masses of tropical origin. This behaviour appears reasonable, because the OMI-TOC NN was trained using only midlatitude data. Anyway, further

Table 2.4: Error statistics for the OMI-TOC NN and its modified version for all the ozonesonde stations considered in this work.

Station	Station statistics			OMI-TOC NN		Modified OMI-TOC NN	
	N. data	Mean TOC [DU]	Std dev [DU]	RMSE [DU]	Mean bias [DU]	RMSE [DU]	Mean bias [DU]
Ankara	112	38.04	11.54	8.33	−0.21	7.68	0.40
Izaña	227	37.38	8.31	8.67	−5.46	8.71	−5.97
L'Aquila	76	36.00	11.59	8.68	2.50	7.35	1.42
Lerwick	240	44.80	13.41	12.96	−9.28	8.60	−3.46
San Pietro Capofiume	12	34.82	6.55	5.51	0.35	3.91	1.17
Valentia Observatory	141	43.31	11.54	9.63	−6.18	8.88	−5.54
Overall	808	40.54	11.83	10.21	−5.17	8.40	−3.47

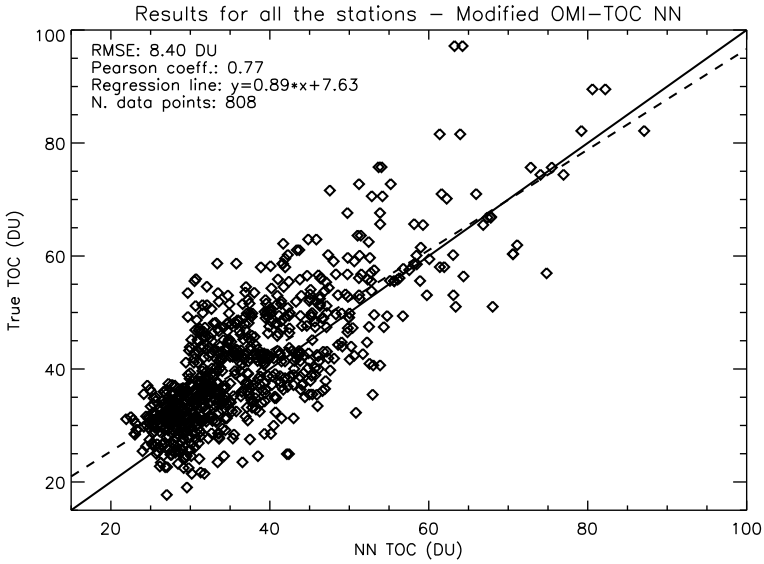

Figure 2.4: Scatter plot of true vs. retrieved TOCs for all the stations considered in this work, for the modified version of the OMI-TOC NN.

investigations are ongoing in order to interpret this result.

In Figs. 2.6 and 2.7, time series of true and retrieved TOC over the six stations considered in this paper are shown for the modified OMI-TOC NN. Apart from the above mentioned case of Izaña, where a strong negative bias of the NN versus the ozonesonde data exists, a slight underestimation tendency can be observed over all the six stations considered in this paper. Such tendency appears to be strongest during the summer months, as evident from the results on Ankara (Fig. 2.6, above panel) and L'Aquila (Fig. 2.6, below panel). Specifically, it appears that the OMI-TOC NN is not able to reproduce situations of enhanced TOCs that occur during the summer. It is still not clear whether this fact is caused by a lack of sensitivity of the algorithm to the lowest atmospheric layers. Appropriate actions, aimed at reducing this effect, should be taken in the development of further versions of the OMI-TOC NN algorithm.

2.7 Outline

In this chapter, the results of a validation of a NN algorithm for tropospheric ozone column retrieval from OMI data – named the OMI-TOC NN

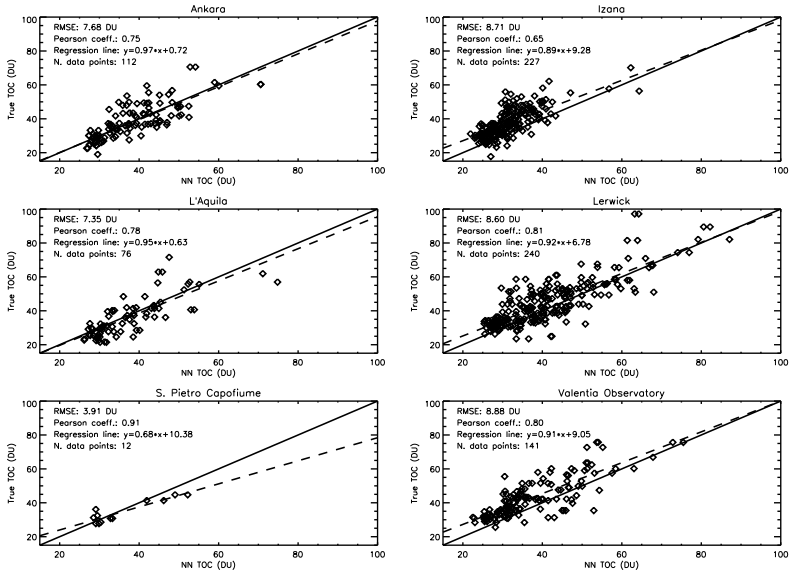

Figure 2.5: Scatter plots of true vs. retrieved TOCs divided by ozonesonde station, for the modified version of the OMI-TOC NN.

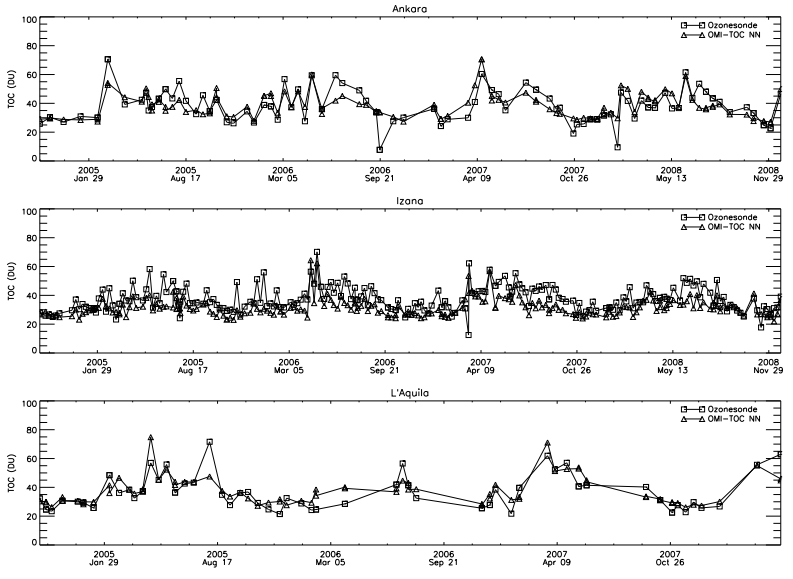

Figure 2.6: Time series of true and retrieved TOCs for Ankara, Izaña and L'Aquila, for the modified version of the OMI-TOC NN.

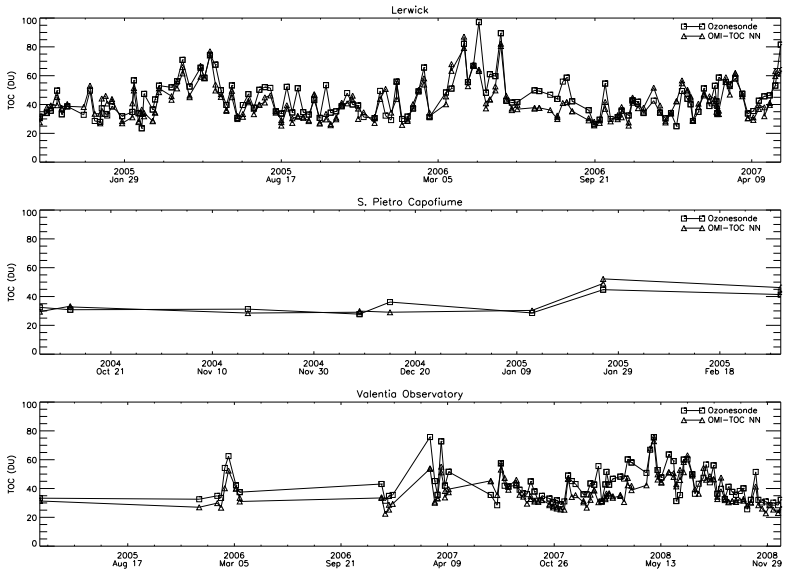

Figure 2.7: Time series of true and retrieved TOCs for Lerwick, San Pietro Capofiume and Valentia Observatory, for the modified version of the OMI-TOC NN.

– are shown. The validation was performed over six ozonesonde stations distributed across the European continent. This validation set is considered as a benchmark for the retrieval performances of the algorithm, as it represents a number of climatological situations that can be encountered over Europe.

A good agreement over Ankara, L'Aquila and San Pietro Capofiume – the most central stations in terms of latitude – was found. However, strong negative biases are present over Lerwick, Valentia Observatory and Izaña, especially in conditions of high TOC values. In order to investigate the reasons for this problem, the retrieval bias of the OMI-TOC NN algorithm was analyzed as a function of the tropopause pressure values taken from the NCEP/NCAR Reanalysis 1. A significant correlation between tropopause pressure and retrieval error was found. As a consequence, a new version of the OMI-TOC NN, having the NCEP/NCAR tropopause pressures in its input vector, was designed, and its results were evaluated over the same validation set.

The modified OMI-TOC NN algorithm exhibited a considerably improved retrieval accuracy, in terms of RMSE, over the whole validation set.

The improvements were found to be most significative on the northernmost stations of Lerwick and Valentia Observatory, where cases of low tropopauses (i.e. high tropopause pressures) are most frequent. However, no improvements were observed on Izaña, where tropopause pressures larger than 200 hPa are quite unlikely. The results of the modified OMI-TOC NN on Izaña also suggest that using the tropopause pressure as an input for the algorithm is still not sufficient to improve the retrieval accuracy in cases of high tropopauses. In the future, this issue will be addressed by including tropical ozonesonde stations in the training set.

A major point that might be raised on the basis of these results is that using 200 hPa as upper integration limit in the TOC definition is not a sensible choice in order to characterize the tropospheric ozone column. Further versions of the OMI-TOC NN algorithm should provide estimates of the ozone column up to the actual tropopause, whether it be defined based on the NCEP/NCAR Reanalysis or by other means (e.g. dynamical tropopause).

Acknowledgements

This work has been carried out in the framework of the ESA Project C1P.2930. All the PIs of the ozonesonde stations whose data were used in this work are gratefully acknowledged. The ozone monitoring activities of CETEMPS are partly funded by the Italian Ministero dell'Ambiente e della Tutela del Territorio e del Mare. The data for Ankara, Lerwick and Valentia Observatory ozonesonde stations were retrieved from the World Ozone and Ultraviolet radiation Data Center (WOUDC) archive (http://www.woudc.org). The data for the Izaña ozonesonde station were obtained as part of the Network for the Detection of Atmospheric Composition Change (NDACC) and are publicly available (see http://www.ndacc.org). The NCEP Reanalysis data are provided by the NOAA/OAR/ESRL PSD, Boulder, Colorado, USA, from their Web site at http://www.esrl.noaa.gov/psd/.

Chapter 3

Global tropospheric ozone retrievals from OMI data by means of neural networks

Parts of this chapter are extracted from the following paper:

Di Noia, A., P. Sellitto, F. Del Frate and J. de Laat (2013), "Global tropospheric ozone retrievals from OMI data by means of neural networks", *Atmos. Meas. Tech.*, 6, 895-915, doi:10.5194/amt-6-895-2013.

3.1 Introduction

Ozone is one of the most important trace gases in the Earth's atmosphere. Ozone is most abundant in the stratosphere, where it shields the troposphere from harmful ultraviolet radiation. In the troposphere, ozone acts as a precursor of the hydroxyl (OH) radical, which is able to remove pollutants from the troposphere via oxidation reactions (*Jacob*, 1999). Furthermore, tropospheric ozone is a pollutant itself, since it is harmful for the biosphere when it reaches high concentrations near the Earth's surface (*Heck et al.*, 1982; *Lippmann*, 1989). Finally, tropospheric ozone acts as a greenhouse gas (*Shindell et al.*, 2006).

Tropospheric ozone variations may occur over relatively small spatial scales. Concentrations of tropospheric ozone are affected by several factors. First, they depend on the concentrations of its precursors – namely, nitrogen oxides (NO_x), carbon monoxide (CO) and Volatile Organic Compounds (VOCs) – which are either emitted as a consequence of human

activities or due to natural causes (e.g. lightnings, which produce NO_x). Since tropospheric ozone is produced from its precursors via photochemical reactions (*Chameides and Walker*, 1973), the intensity of the solar radiation reaching the troposphere is another important factor. A further source of tropospheric ozone is the downward transport of air rich in ozone from the stratosphere, during the so called Stratosphere-Troposphere Exchange (STE) (*Holton et al.*, 1995). This process is particularly significant at mid-latitudes (see, e.g., *Shapiro*, 1980). Long-range transport of tropospheric ozone and its precursors also affects its spatial distribution (*Carmichael et al.*, 1998; *Creilson et al.*, 2003).

Monitoring tropospheric ozone using satellite instruments is important in order to obtain a global picture of its distribution. However, several difficulties are encountered in inferring tropospheric ozone concentrations from satellite observations. First, the contribution of tropospheric ozone to the measured radiances is much weaker than the contribution coming from stratospheric ozone. Second, current ultraviolet or thermal infrared measurements have usually a reduced sensitivity to lower tropospheric ozone (*Natraj et al.*, 2011, and references therein).

The first attempts to derive information on tropospheric ozone from satellite observations date back to the 1980's. *Fishman et al.* (1986, 1987) first suggested that total ozone measurements made from the Total Ozone Mapping Spectrometers (TOMS) could contain information on cases of enhanced tropospheric ozone. In the first algorithms for quantitative tropospheric ozone retrievals, the information on tropospheric ozone was obtained by subtracting a stratospheric ozone column measurement from a co-located total ozone measurement. The stratospheric ozone column was estimated from limb observations (*Fishman and Larsen*, 1987; *Fishman*, 2000, and references therein) or from ozone column measurements above high convective clouds (*Ziemke et al.*, 1998, 2001; *Ahn et al.*, 2003; *Newchurch et al.*, 2003) or high mountains (*Jiang and Yung*, 1996; *Kim and Newchurch*, 1996; *Newchurch et al.*, 2001). An alternative approach, specifically designed for TOMS observations, was to directly infer tropospheric ozone information based on the dependence of TOMS total ozone columns on the scan angle of the instrument (*Kim et al.*, 1996, 2001, 2004).

More recently, after the development of new satellite instruments, with hyperspectral measurement capabilities, the direct determination of tropospheric ozone from the UV/VIS part of the spectrum has become feasible (*Munro et al.*, 1998; *Liu et al.*, 2005, 2006, 2010). Nevertheless, residual techniques similar to those described above for TOMS have been also applied to hyperspectral data. For instance, *Valks et al.* (2003) developed a cloud

slicing algorithm for the Global Ozone Monitoring Experiment (GOME), whereas nadir-limb residual techniques have been used by *Ziemke et al.* (2006); *Schoeberl et al.* (2007) and *Yang et al.* (2007) to estimate tropospheric ozone column by subtracting Microwave Limb Sounder (MLS) limb stratospheric ozone columns from Ozone Monitoring Instrument (OMI) total ozone columns. Recently, *Ebojie et al.* (2013) have developed a residual method for retrieving the tropospheric ozone column from a matching between limb and nadir SCIAMACHY measurements.

Another possibility to directly retrieve tropospheric ozone from satellite hyperspectral observation is the application of Neural Networks (NNs). NN algorithms for tropospheric ozone retrievals from OMI and the Scanning Imaging Absorption spectrometer for Atmospheric Chartography (SCIAMACHY) have been recently developed (*Sellitto et al.*, 2011, 2012a, respectively). In particular, *Sellitto et al.* (2011) developed an algorithm to retrieve tropospheric ozone from OMI data at northern midlatitudes, named the OMI-TOC NN. The algorithm yields daily estimates of the tropospheric ozone column from surface to 200 hPa at the northern midlatitudes, by using OMI reflectance spectra, Solar Zenith Angle (SZA) at 19 wavelengths and the total ozone column from the OMI-TOMS total ozone (OMTO3) Level 2 product (*Bhartia and Wellemeyer*, 2002). The performances of the OMI-TOC NN algorithm were shown to be comparable with those of the physics-based algorithms of *Schoeberl et al.* (2007) and *Liu et al.* (2010) by means of a validation exercise with ozonesonde measurements at northern midlatitudes, with Root Mean Square (RMS) errors around 8 DU and correlation coefficients around 0.60 between the actual and the retrieved tropospheric ozone columns (*Sellitto et al.*, 2011). *Di Noia et al.* (2013a) further validated the OMI-TOC NN over a number of European ozonesonde stations, finding similar results, and pointing out the possible presence of a negative bias in the OMI-TOC NN in cases of low tropopauses (tropopause pressures larger than approximately 250 hPa).

The main limitations of the OMI-TOC NN algorithm are its coverage, which is limited at the northern midlatitudes, and the choice to use the 200 hPa level as upper integration limit for the retrieved ozone columns, regardless of the actual tropopause conditions. In particular, this latter feature raises the question of whether it is legitimate to say that the retrieved ozone columns are "tropospheric", since even at midlatitudes the actual tropopause pressure can be very different from 200 hPa (*Hoinka*, 1998). In order to overcome this problem, a pre-processed tropopause height can be used as upper integration limit for the retrieved ozone columns. By doing so, it is possible to produce estimates that represent the actual "tropospheric"

ozone column more realistically. For this study, the thermal tropopause given by the National Center for Environmental Prediction (NCEP) / National Center for Atmospheric Research (NCAR) Reanalysis (*Kalnay et al.*, 1996) has been used.

In this chapter, the results of an improved NN algorithm for tropospheric ozone retrieval are presented. The improvements can be summarized as follows: (i) the geographical coverage of the algorithm is extended to the entire globe, whereas the OMI-TOC NN was limited to the northern midlatitudes; (ii) an estimate of the ozone column from the surface to the NCEP/NCAR tropopause is produced; (iii) a number of ancillary data are used as additional inputs for the algorithm in order to better constrain the retrieval problem; (iv) the observation geometry is better parameterized in the input vector by including the viewing zenith angle (VZA) and the terrain height; (v) the TOMS total ozone column is not used anymore in the input vector, so as to make the new algorithm independent from other ozone products. The main differences between the two algorithms are summarized in Table 3.1.

Besides these key points, a number of additional technical issues are addressed in the pre-processing of OMI radiance and irradiance spectra (namely, several refinements were introduced in the data quality control and filtering routines). Furthermore a different input dimensionality reduction strategy is adopted, with a simple linear Principal Component Analysis (PCA) used instead of the Extended Pruning (EP) technique. The new algorithm will be henceforth referred to as OMITROPO3-NN.

This chapter is organized as follows. In Section 3.2 the generation of the OMITROPO3-NN dataset is described and all the pre-processing steps are discussed; in Section 3.3 the choices made in the NN training are explained; general validation results are shown in Section 3.4; in Section 3.5 global tropospheric ozone fields retrieved on two dates during August 2006 are used as examples, in order to give further insight into some of the characteristics of the OMITROPO3-NN; Section 3.6 presents conclusions and hypotheses for future work.

3.2 Preparation of the OMITROPO3-NN dataset

3.2.1 Definition of the input vector

The list of the input quantities used in the design of the OMITROPO3-NN is shown in Table 3.1. The OMITROPO3-NN retrieves tropospheric ozone columns from reflectance spectra measured in the range 310-345 nm, covered by the OMI UV-2 channel (*Levelt et al.*, 2006b). Wavelengths longer than

Table 3.1: Differences between the OMITROPO3-NN and the OMI-TOC NN algorithms.

	OMI-TOC NN	OMITROPO3-NN
Output product	O_3 column from surface to 200 hPa	O_3 column from surface to NCEP tropopause
Input data	UV1/UV2 reflectances, SZA, total O_3	UV2 reflectance PCs, SZA, VZA, terrain height, NCEP tropopause pressure & temperature profile, cloud fraction, monthly mean TCO from climatology
Coverage	Northern midlatitudes	Global
Nadir nominal resol.	13×48 km^2	13×24 km^2

about 335 nm are outside the ozone absorption bands, but have been included because they contain information about aerosols and surface albedo (*Kleipool et al.*, 2008). Furthermore, the observation geometry was taken into account by including the Solar Zenith Angle (SZA), the View Zenith Angle (VZA) and the terrain height in the input vector. The Relative Azimuth Angle (RAA) was not used in the final specification of the algorithm, because preliminary experimental work showed that its use does not seem to improve the retrieval performances.

Since the ozone absorption cross sections in the considered spectral range – which covers the ozone Huggins bands – are temperature dependent, the temperature profile from the NCEP/NCAR Reanalysis was used as an additional input. An additional advantage associated with the use of temperature as an input is the possibility of exploiting the correlations between ozone and temperature (*Müller et al.*, 2003).

The tropopause pressure from the NCEP/NCAR Reanalysis was also included in the input vector, in order to signal the upper integration limit for the ozone column to be retrieved. Furthermore, the significant positive correlation between tropopause height and the tropospheric ozone column outside the Tropics (*de Laat et al.*, 2005) can be exploited in order to regularize the retrieval. The radiative cloud fraction from the OMI rotational Raman scattering (OMCLDRR) product (*Joiner and Vasilkov*, 2006) was used to account for the enhanced UV radiances which are measured at the

longer wavelengths of the considered spectral interval because of the presence of clouds around the Field Of View (FOV) of the instrument. Using the cloud pressure in the input vector did not improve the retrieval performances, therefore it was left outside the input vector in the final version of the algorithm.

The choice of using a tropospheric ozone climatological value as an input for the algorithm is worth a discussion. The retrieval of tropospheric ozone from UV satellite measurements is strongly ill-posed, because it is difficult to separate variations in the measured UV spectra caused by ozone variations in the troposphere from variations which are related to changes in stratospheric ozone. Therefore, the information content of radiometric measurements and parameters of the forward problem (i.e. observation geometry, temperature profile, etc.) may be not enough to perform the retrieval. Ill-posed problems are usually addressed by complementing the satellite measurements with ancillary data, a priori information about the retrieved state and/or regularization constraints (*Twomey*, 1977; *Rodgers*, 2000; *Doicu et al.*, 2010a). These quantities are used in retrieval algorithms in order to discard solutions of the inverse problem which are extremely unlikely and/or unphysical. As any other retrieval technique, even a neural algorithm can benefit from this kind of information, when available. In the context of neural algorithms, this role is partly played by the target outputs given in the training set, as they allow an implicit regularization of the inverse problem, by "teaching" the NN to map the radiometric observations into physically meaningful solutions.

However, using this constraint alone may not be enough to account for the local and seasonal variability of the retrieved quantity. This issue can be addressed either by training different NNs, one for each season and/or wide geographical area (e.g. latitude band), or by introducing an input quantity that gives the NN relevant climatological information. The latter approach was preferred in this work, because it leads to a global NN model, flexible enough to perform reasonably well in a broad set of situations. On the contrary, the former approach would have led to specialized NNs, each trained with a reduced number of examples. This would have been especially true for tropics and southern midlatitudes, where the spatial coverage provided by the ozonesonde networks is much sparser than for northern midlatitudes and poles.

In the literature about the NN based algorithms for satellite retrievals, several ways to include a priori or first guess information in the input vector have been proposed. For instance, *Aires et al.* (2001) proposed the use of a first guess in NNs for atmospheric retrievals from microwave observations,

while *Müller et al.* (2003) simply used the latitude as a climatological indicator in their Neural Network Ozone Profile Retrieval System (NNORSY) applied to GOME data. In the present work, the monthly mean tropospheric ozone column – taken from the *Ziemke et al.* (2011) OMI-MLS tropospheric ozone climatology – was used as additional input for the retrieval algorithm. This climatology was preferred to other climatologies – such as *Fortuin and Kelder* (1998) or *Logan* (1998) – because it represents the tropospheric ozone variations with longitude in a finer detail. The horizontal resolution of the *Ziemke et al.* (2011) climatology is 5° in latitude and longitude.

When a priori information is used in a retrieval algorithm, the risk of biasing the retrievals towards the a priori should be monitored. This issue is discussed in Sect. 3.4.3.

3.2.2 Geographical coverage and co-location procedure

A comprehensive dataset of co-locations between OMI data and ozone soundings was created in order to train the NN and to assess its performances.

The dataset covers the time period from 2004 to 2011, and consists of ozone soundings taken from several sources; the archives of the World Ozone and Ultraviolet radiation Data Center (WOUDC), Southern Hemisphere Additional Ozonesondes (SHADOZ) network (*Thompson et al.*, 2003) and the Network for the Detection of Atmospheric Composition Change (NDACC), data from the Intercontinental Chemical Transport Experiment-B (INTEX-B) Ozonesonde Network Study 2006 (IONS06) and the Arctic Intensive Ozonesonde Network Study (ARCIONS) campaigns, performed during 2006 and 2008 respectively (*Tarasick et al.*, 2010), and data from ozone soundings performed over Italy, provided by the Center for Integration of remote sensing techniques and numerical modeling for the prediction of severe weather (CETEMPS) of L'Aquila University, the Institute of Atmospheric Sciences and Climate (ISAC) of the Italian National Research Council (CNR) and the Italian Air Force Centre of Aeronautical Meteorological Experimentation (ReSMA).

The geographical distribution of the ozonesonde stations whose data were used to create the dataset is shown in Fig. 3.1.

The ozone soundings were co-located with OML1BRUG data according to the overpass info provided by the Aura Validation Data Center (AVDC) for the OMTO3 Level 2 product. The following procedure was followed in performing the co-locations:

1. For each ozone sounding, the OML1BRUG files corresponding to the overpass orbits indicated in the AVDC info were selected;

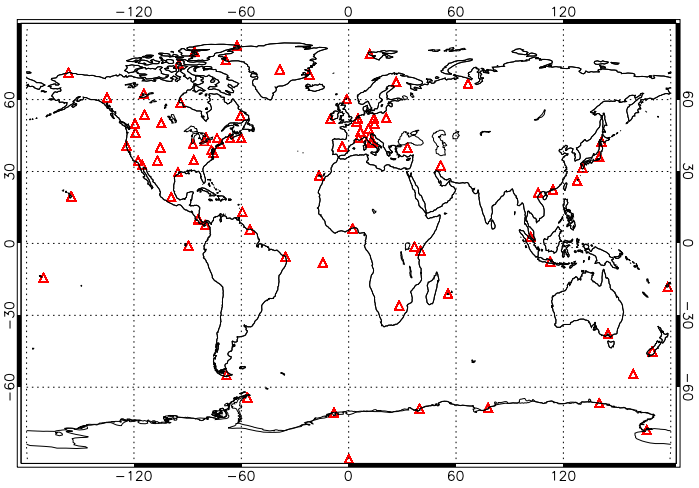

Figure 3.1: Spatial distribution of the ozonesonde stations used to construct the dataset to train and test the NN.

2. For each OML1BRUG file, the OMI pixel having its center closest to the ozonesonde station was selected as a candidate for the co-location;

3. The candidate pixel was discarded if its center and the station coordinates were more than 1° apart, in latitude or longitude or separated by more than 6 hours in time.

Such co-location criteria were adopted in order to be reasonably sure that the tropospheric air volumes sampled by OMI were representative of the volume actually covered by the corresponding ozone soundings.

3.2.3 Pre-processing of OMI spectral measurements

The OML1BRUG radiance spectra were converted in Top Of Atmosphere (TOA) reflectance spectra by normalization to OML1BIRR irradiance spectra and cosine of the Solar Zenith Angle (SZA). A natural logarithm was then applied to the computed reflectances. The following pre-processing steps were applied in order to compute the TOA reflectance spectra:

1. The quality of each radiance and irradiance spectral pixel was checked with respect to the OMI L1B quality flags, according to the guidelines given in *van den Oord and Veefkind* (2002). The spectral pixels that failed the quality test were discarded from the subsequent computations.

2. The spectra whose number of discarded wavelengths exceeded the 5% of the total were discarded, and were not used in the co-location procedure.

3. The radiance and irradiance spectra which survived this screening procedure were linearly interpolated on a 0.1 nm wide common spectral grid. The linear interpolation has been chosen over more sophisticated techniques (e.g., cubic spline interpolation) because it is computationally less demanding.

4. The TOA reflectance spectra were computed using the interpolated radiance and irradiance spectra, and the natural logarithm of the resulting values was computed.

As for the quality flag based filtering, particular care was taken in order to exclude pixels affected by row anomaly from the dataset. According to the information available from the Royal Dutch Meteorological Institute (KNMI), the row anomaly started to appear on June 25th, 2007, affecting the rows 53-54 (0 based) in the OMI across-track direction. After about one year, it expanded to the rows 37-44, and began to assume an erratic behaviour after January 24th, 2009, randomly affecting subsets of the rows 24-59. Additional information about the row anomaly effect in OMI can be found at the webpage www.knmi.nl/omi/research/product/rowanomaly-background.php. According to this information, the flagging of row anomaly events in the OMI Level 1B products has not been complete until February 1st, 2010. Therefore, it was decided to exclude from the dataset all the OMI measurements over the rows 24-59 starting from January 24th, 2009, in order to be reasonably sure that the test statistics were not compromised by contaminated pixels.

Apart from the filtering based on the quality flags, other screening actions were performed in order to strengthen the quality of the dataset. Specifically, pixels having cloud fractions larger than 0.3 were discarded. The choice of 0.3 as a threshold for the cloud fraction was made to establish a trade-off between the need of excluding pixels which are excessively affected by clouds and the need of ensuring an adequate number of samples to train the NN and assess its performances in a wide range of situations.

The spectral interpolation procedure led to log-reflectances computed at 351 wavelengths. As pointed out by several studies, the spectral features of UV radiances or reflectances usually exhibit a considerable correlation, and a spectral resolution of 0.1 nm is more than necessary for ozone retrievals (*Chance et al.*, 1997; *Richter and Wagner*, 2011). Therefore, the information

content of the computed log-reflectance spectra can be considerably compressed through a data dimensionality reduction technique. In this work, a simple linear Principal Component Analysis (PCA) was used. In order to choose an appropriate value for the number of Principal Components (PCs) to retain after the PCA procedure, the error in the reconstruction of the log-reflectance spectra from the compressed spectra was monitored as a function of the number of retained PCs. This procedure led to retain 20 PCs, since adding further PCs did not improve the reconstruction significantly (reflectance reconstruction RMS error of about 0.01%).

3.2.4 Processing of ozonesonde data

The ozonesonde stations were co-located with the NCEP/NCAR tropopause pressure fields according to a nearest neighbour criterion, i.e. each ozonesonde profile was co-located with the closest reanalysis grid point. The ozone profiles were screened with respect to data affected by measurement errors.

The ozone profiles were then processed in order to compute the Tropospheric Columnar Ozone (TCO) according to the following equation, that can be found at the ESA Tropospheric Emission Monitoring Internet Service (TEMIS) webpage (www.temis.nl):

$$\mathrm{TCO} = 10 \cdot \frac{RT_0}{g_0 p_0} \sum_{i=1}^{N-1} 0.5 \cdot [\mathrm{VMR}_{\mathrm{O}_3}(p_i) + \mathrm{VMR}_{\mathrm{O}_3}(p_{i+1})] \cdot (p_i - p_{i+1}) \quad (3.1)$$

using the NCEP/NCAR tropopause pressure as p_N. In Eq. (3.1), TCO is the tropospheric ozone column expressed in Dobson Units, $R = 287.3\ \mathrm{J\,kg^{-1}\,K^{-1}}$ is the specific gas constant for air, $T_0 = 273.15$ K was assumed as standard surface temperature, $g_0 = 9.80665\ \mathrm{m\,s^{-2}}$ was assumed as gravity acceleration at sea level, $p_0 = 1013.25$ hPa was used as standard surface pressure, p_i is the i-th pressure level in hPa, and $\mathrm{VMR}_{\mathrm{O}_3}(p_i)$ is the ozone volume mixing ratio at the level p_i.

3.3 Design of the neural network

3.3.1 Training, validation and test subsets

The co-location procedure described in the previous section has led to the generation of 10,017 input-output pairs. Such pairs were used to train the NN algorithm and assess its performances with data not used during the training phase. The network was trained using only co-locations which cover

the period from 2004 to 2008. This choice was made in order to set aside enough data to test the NN behaviour outside the training period. The dataset was split into four subsets: *i*) 5,489 pairs were used to train the NN; *ii*) 1,737 pairs were used to determine when to stop the training process via early stopping cross-validation (see Sect. 1.4.3.4); *iii*) 2,071 pairs were used to evaluate the generalization of the trained NN *during* the training period; *iv*) 720 pairs were used to evaluate the trained NN generalization *outside* the training period.

From now on, these four datasets will be referred to as $\mathcal{D}_{\text{train}}$, $\mathcal{D}_{\text{valid}}$, $\mathcal{D}_{\text{test1}}$ and $\mathcal{D}_{\text{test2}}$, respectively. The union between $\mathcal{D}_{\text{test1}}$ and $\mathcal{D}_{\text{test2}}$ will be indicated as $\mathcal{D}_{\text{test}}$.

In order to ensure the independence between the datasets, without affecting their comprehensiveness, the data were assigned to each set based on the ozonesonde station they referred to. Stations used in the training dataset were not used for the test and validation datasets. A significant number of co-locations pertaining to the different latitudinal bands were present in each subset.

3.3.2 Input pre-processing

The input vector of the OMITROPO3-NN consists of 43 inputs: 20 PCs of the reflectance spectra, SZA, VZA, terrain height, NCEP/NCAR temperature profiles at 17 pressure levels, NCEP/NCAR tropopause pressure, radiative cloud fraction and monthly mean TCO. A logistic activation function was chosen for the hidden and the output layers of the NN.

Before proceeding with the NN training, a further pre-processing step was applied to the input and target data in order to make them compatible with the mathematical properties of the logistic function. Specifically, since the output of the logistic function lies between 0 and 1, a linear scaling between these values was applied to the TCO data. Similarly, all the input data were linearly scaled between -1 and 1, in order to avoid the saturation of the hidden neurons after the initialization of the NN weights.

3.3.3 Training and architecture selection

The NN was trained using the Scaled Conjugate Gradient (SCG) learning algorithm (*Møller*, 1993). An heuristic procedure, as described in Sect. 1.4.3.4, was adopted to select the number of hidden layers and neurons. The selected NN architecture has one hidden layer with 5 neurons inside. For this architecture, the training was stopped after about 1,000 cycles, using early

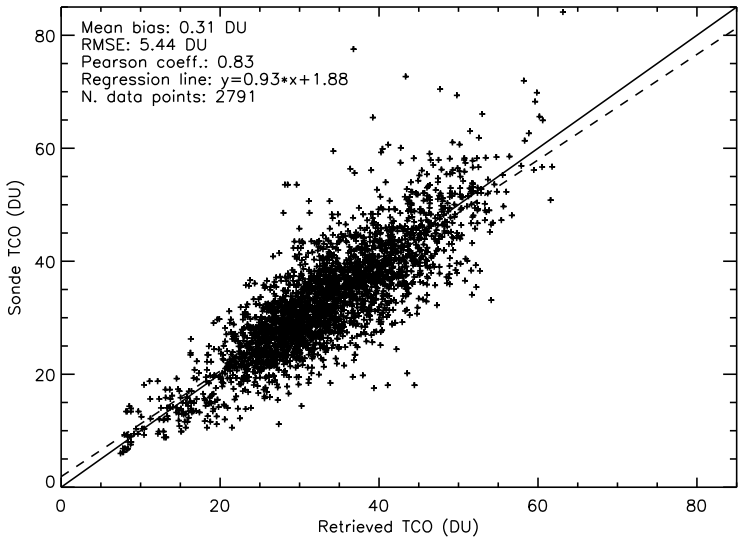

Figure 3.2: Overall validation results, obtained both during and after the time period covered by the training set.

stopping cross-validation.

3.4 Results

The results obtained over the whole $\mathcal{D}_{\text{test}}$ set are shown in Fig. 3.2, where the performances of the algorithm are summarized through the mean bias, the Root Mean Square Error (RMSE) and the Pearson correlation coefficient between the reference values of TCO and those retrieved by the NN. A more detailed insight on the error distribution is given in Figs. 3.3 and 3.4, where the histograms of the absolute and the relative differences between the retrieved and the "true" TCOs, respectively, are shown, together with some of the relevant statistical parameter. It can be seen that the retrievals have a small bias (0.31 DU), and that the error histograms are fairly symmetrical (skewness of -0.41 for the absolute differences and 1.38 for the relative differences).

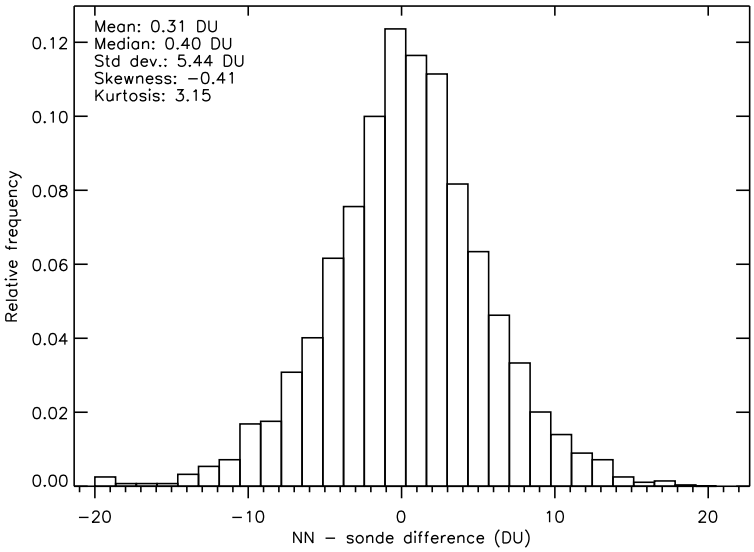

Figure 3.3: Histogram of the differences between the retrieved and the target tropospheric ozone column.

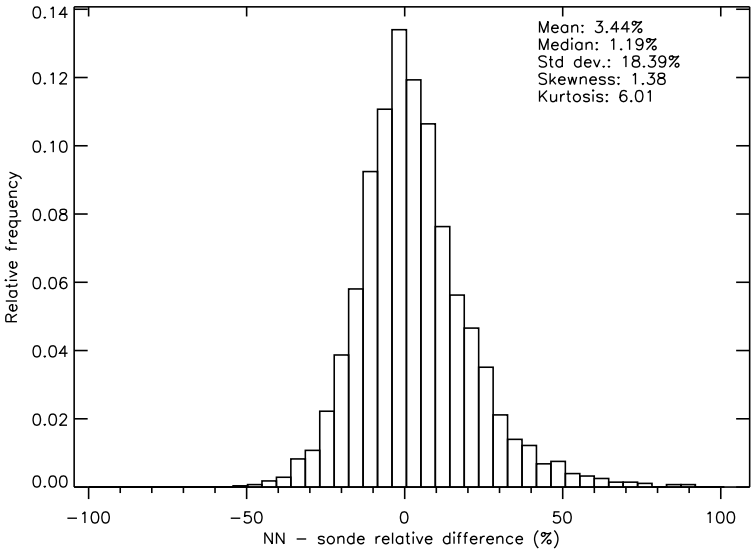

Figure 3.4: Histogram of the percent differences between the retrieved and the target tropospheric ozone column.

Table 3.2: Retrieval results during and after the period covered by the training set. The training set covers the period from 2004 to 2008.

Period	Mean Bias (DU)	RMSE (DU)	Pearson coeff.	N. data
2004-2008	0.08	5.26	0.82	2071
2009-2011	0.96	5.93	0.86	720

3.4.1 Generalization during and after the training period

It is important to understand whether there are any differences in the performances of the algorithm between the years covered by the training set and those not covered by it, as this may provide an indication on the degree of robustness of the NN with respect to changes of the instrumental response. Separate error statistics were computed for the $\mathcal{D}_{\text{test1}}$, containing examples pertaining to the period between 2004 and 2008 and the $\mathcal{D}_{\text{test2}}$ sets, consisting of examples acquired after 2008. The results are summarized in Table 3.2.

The statistics of the comparison between the NN results and the sonde observations are similar to the results for the training period (bias smaller than 1 DU, RMSE smaller than 6 DU, correlation coefficient larger than 0.8). These results indicate that applying the NN to OMI data acquired after the period covered by the training set should not result in a significant performance degradation of the algorithm. This is consistent with the very good radiometric stability displayed by OMI throughout its operational lifetime. Details about the OMI calibration status can be found at the webpage www.knmi.nl/omi/research/calibration/instrument_status_v3/perf_plots/index.html.

3.4.2 Geographical features in the retrieval algorithm

The performances of the algorithm were evaluated after stratifying the $\mathcal{D}_{\text{test}}$ set by latitude zone. Five zones were defined: Antarctica (latitude between 90°S and 60°S), southern midlatitudes (60°S to 30°S), tropics (30°S to 30°N), northern midlatitudes (30°N to 60°N) and Arctic (60°N to 90°N).

Maps of mean biases, Pearson correlation coefficients and RMSEs found over the ozonesonde stations having at least 35 data included in the test dataset are shown in Fig. 3.5.

The performances of the algorithm, in terms of mean bias, RMSE and Pearson coefficient, are comparable for four of the five zones. Only for the

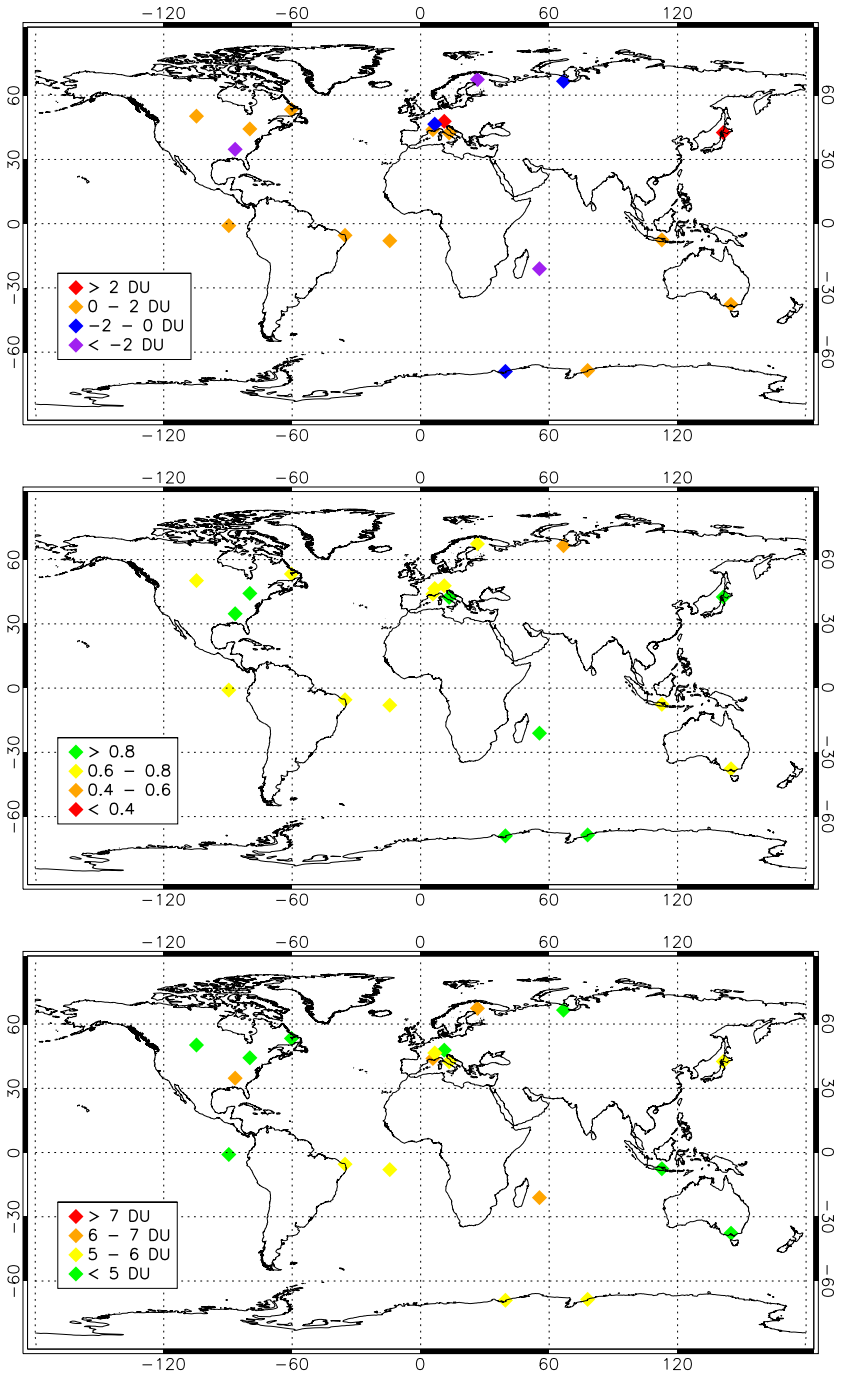

Figure 3.5: Mean bias (*top*), Pearson correlation coefficient (*middle*) and RMS difference (*bottom*) between ozonesonde measurements and retrievals for all the measurement stations having at least 35 measurements in the test dataset.

Table 3.3: Summary of the comparisons between OMITROPO3-NN and ozonesondes

Latitude band	Mean bias (DU)	RMSE (DU)	Pearson coeff.	N. data
90°S–60°S	1.99	5.63	0.86	271
60°S–30°S	1.45	5.22	0.76	181
30°S–30°N	0.59	5.65	0.80	611
30°N–60°N	0.52	5.28	0.82	1357
60°N–90°N	−2.69	5.66	0.54	371

Arctic region the bias was larger. The causes of this bias are currently under study. A possible reason might line in artifacts related to the occasionally difficult definition of the tropopause in this region.The results are summarized in Table 3.3.

Table 3.4 presents a summary of the comparison statistics for each of the stations with at least 20 measurements included in the $\mathcal{D}_{\text{test}}$ set. The stations are sorted in order of increasing latitude. For most stations the NN results agree quite well with the sonde observations (correlations between 0.72 and 0.88, biases between −3 and 2 DU). The latest 5 entries in Table 3.4 are the Arctic stations. It can be noticed that the OMITROPO3-NN has a negative bias over all these stations. Such bias is particularly significant at Sodankyla (−3.68 DU).

Scatter plots and time series of the "true" and retrieved TCO as a function of the Day Of Year (DOY) for the stations Broadmeadows (Australia) and Goose Bay (Canada) are shown in Figs. 3.6 and 3.7 as examples.

3.4.3 Non-climatological features

An important question is to what extent is the algorithm capable of recognize anomalous events, i.e. cases of large departures of the actual TCO from its climatological value used as an a priori for the retrieval. In order to investigate this aspect, a TCO relative anomaly was defined as the percent difference between the actual TCO and its climatological value taken from the Ziemke climatology, and the difference between the retrieved and the actual TCO anomalies was analyzed. The results on the $\mathcal{D}_{\text{test}}$ set are plotted in Fig. 3.8. The correlation coefficient between the actual and the retrieved TCO anomalies is smaller than the correlation found between the TCO absolute values. Nevertheless, there still exists a reasonable agreement between the actual and the retrieved anomalies, as correlations decreased

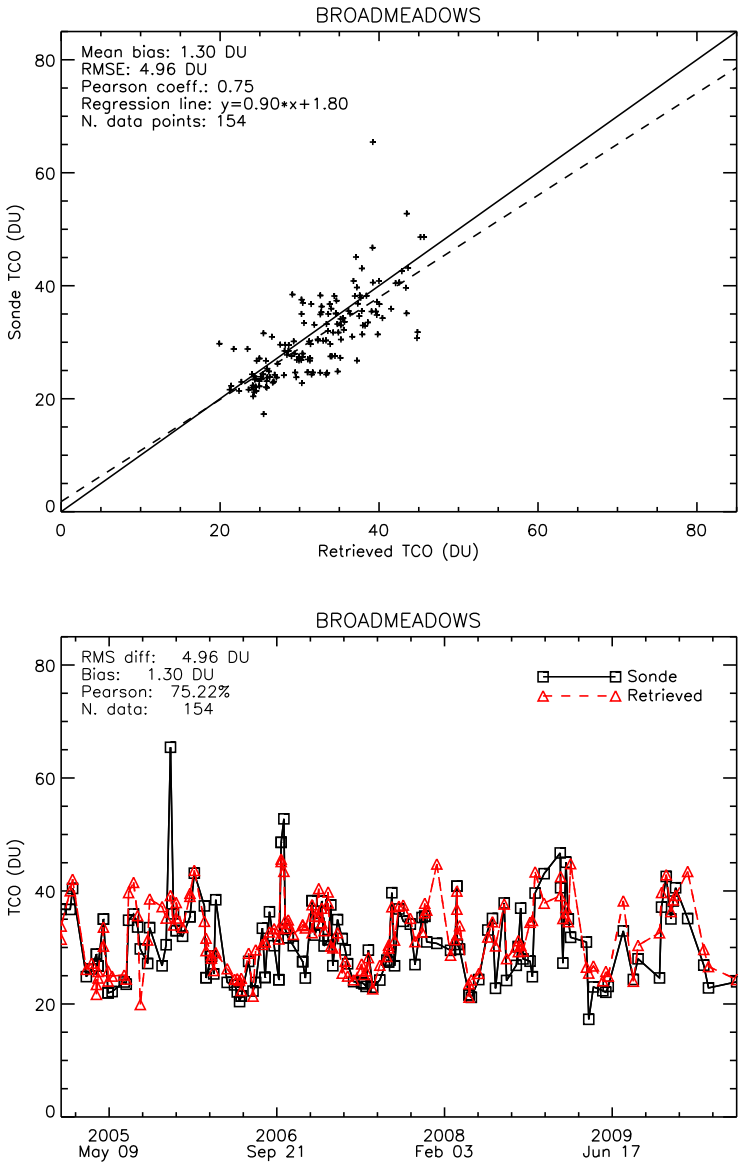

Figure 3.6: Scatter plot (*above*) and time series (*below*) of retrieved and ozonesonde TCO at Broadmeadows (Australia).

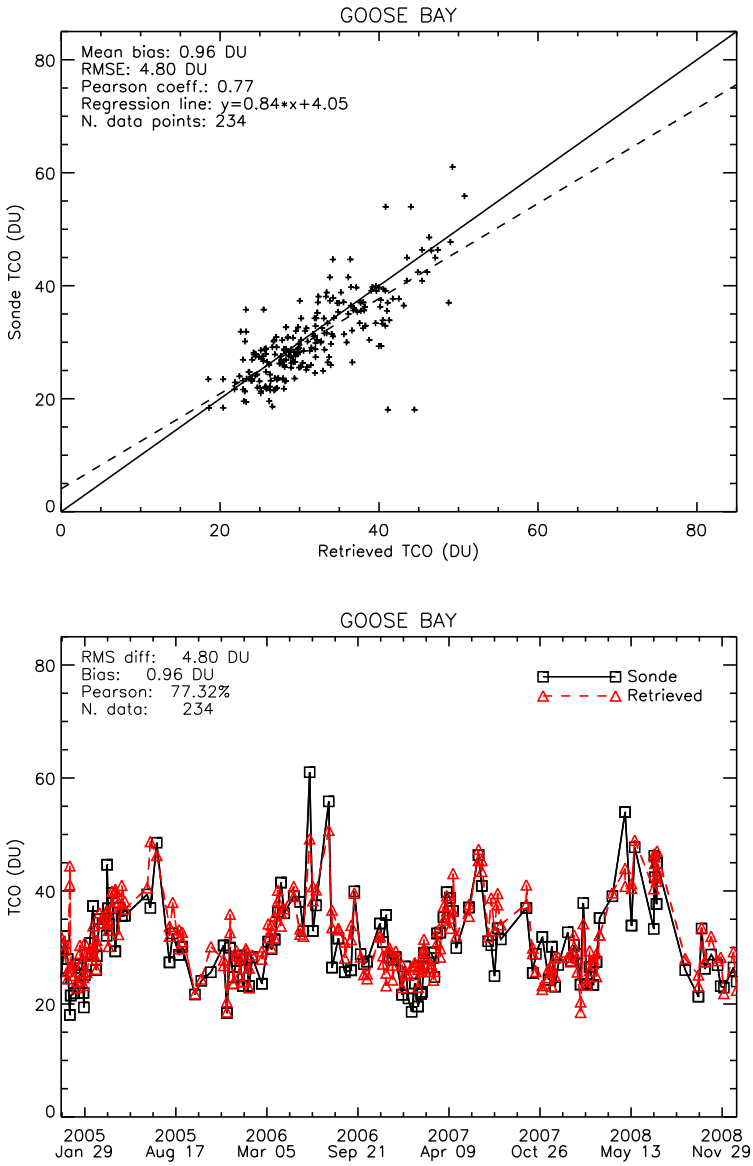

Figure 3.7: Scatter plot (*above*) and time series (*below*) of retrieved and ozonesonde TCO at Goose Bay (Canada).

Table 3.4: Retrieval results divided by station, sorted by increasing latitude. Only stations with at least 20 measurements included in the $\mathcal{D}_{\text{test}}$ set were considered.

Station name	Lat.	Lon.	Bias (DU)	RMSE (DU)	Pearson	N. data
Amundsen (South Pole)	-89.98	0.00	0.48	2.24	0.94	26
Syowa	-69.00	39.58	-0.28	5.35	0.90	41
Davis	-68.58	77.97	1.93	5.16	0.87	169
Broadmeadows	-37.69	144.95	1.30	4.96	0.75	154
La Reunion	-21.08	55.48	-2.66	6.71	0.80	64
Suva	-18.13	178.32	0.70	4.98	0.59	28
Ascension Island	-7.98	-14.42	0.86	5.54	0.72	144
Watukosek (Java)	-7.57	112.65	1.09	4.58	0.74	37
Maxaranguape (Natal)	-5.45	-35.33	0.66	5.37	0.74	121
Nairobi	-1.27	36.80	2.30	4.17	0.76	23
San Cristobal	-0.92	-89.60	1.79	4.82	0.73	44
Barbados	13.16	-59.43	1.77	5.81	0.38	21
Hong Kong Observatory	22.31	114.16	0.94	6.29	0.67	21
Naha	26.20	127.68	1.00	6.06	0.75	28
Huntsville	34.72	-86.64	-2.69	6.07	0.83	143
Tateno-Tsukuba	36.06	140.10	0.59	7.36	0.88	24
Madrid (Barajas)	40.46	-3.65	2.09	5.46	0.80	33
L'Aquila	42.38	13.31	0.94	5.30	0.81	35
Sapporo	42.56	141.33	2.21	5.94	0.87	130
Haute Provence	43.93	5.70	1.66	6.70	0.73	146
Egbert	44.23	-79.78	0.50	4.89	0.83	136
Payerne	46.49	6.57	-0.66	5.42	0.71	60
Hohenpeissenberg	47.80	11.02	2.12	4.79	0.71	52
Regina (Bratt's Lake)	50.21	-104.71	0.86	4.24	0.78	212
Valentia Observatory	51.93	-10.25	-2.35	3.94	0.89	22
Lindenberg	52.16	14.12	-1.68	4.47	0.57	22
Goose Bay	53.30	-60.36	0.96	4.80	0.77	234
Whitehorse	60.70	-135.07	-3.27	6.66	0.37	34
Yellowknife	62.50	-114.48	-1.90	4.13	0.67	21
Salekhard	66.50	66.70	-0.28	4.46	0.47	84
Sodankyla	67.34	26.51	-3.68	6.03	0.61	207
Scoresbysund	70.49	-21.98	-2.50	5.67	0.58	25

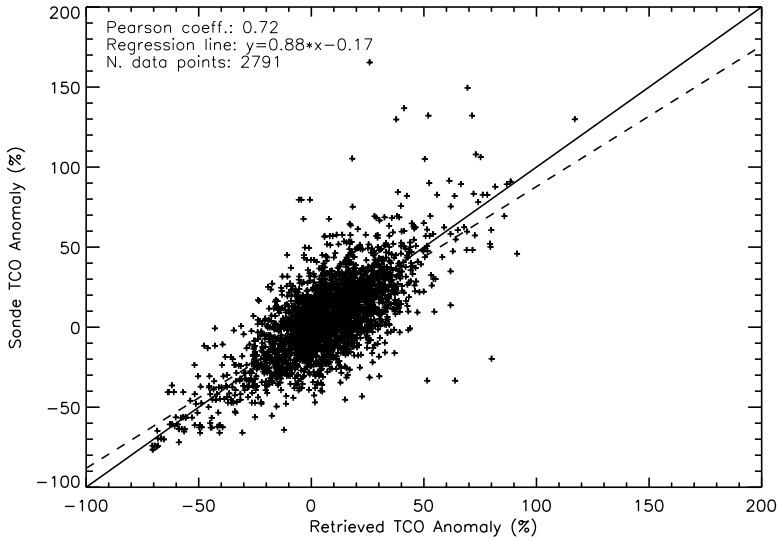

Figure 3.8: Comparison between actual and estimated TCO anomaly.

only from 0.83 to 0.72, indicating that the algorithm uses information other than the a priori in order to perform its retrievals. Such information comes from the satellite measurements as well as from the reanalysis data provided as inputs for the NN. An attempt to investigate the relative contribution of satellite measurements and satellite data to the retrieved TCOs is made in the next subsection.

The geographical dependence of the algorithm performances with TCO anomalies is shown in Fig. 3.9, where a map of the Pearson correlation coefficient between actual and retrieved TCO anomalies, over the ozonesonde stations having at least 35 measurements included in the test set, is shown. The map indicates that the anomaly detection capability of the NN at Tropics is worse than at mid- and polar latitudes. This could be related to the limited availability of training data in the tropics. However, it must be kept in mind that a precise TCO anomaly estimation in the tropics is a challenging task, because the range of the anomalies over this area is usually small.

3.4.4 Contribution of OMI reflectances to the retrieved TCO

Given the large amount of ancillary data used by the OMITROPO3-NN, many of which are correlated with the TCO, it is important to evaluate

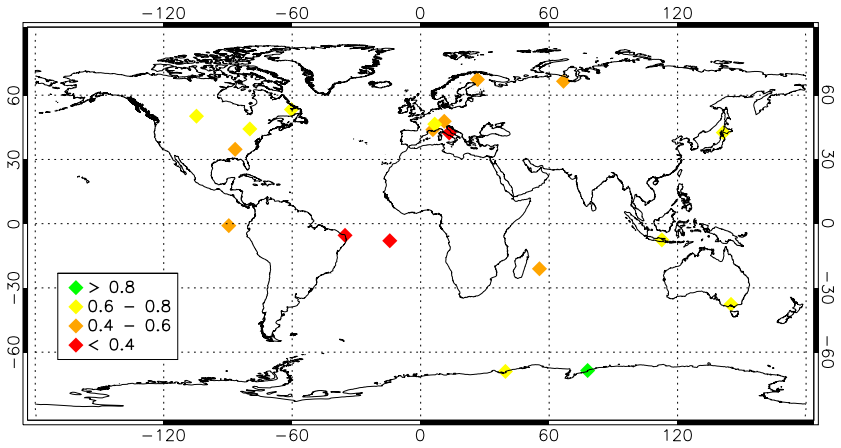

Figure 3.9: Pearson correlation coefficient between actual and estimated TCO anomalies for all the measurement stations having at least 35 data included in the test set.

to what extent using OMI reflectances improves the results with respect to using only the ancillary data themselves in a regression. Some insight on this point can be obtained by training a second NN using only the ancillary data as inputs. This second network achieved a RMSE of 6.11 DU on the test set, with a correlation coefficient of 0.78. The results divided by station are shown in Tab. 3.5. It can be seen that NN trained only the ancillary data performs worse than the OMITROPO3-NN over most of the ozonesonde stations. The use of OMI reflectances seems to produce the most significant improvements at high latitudes, whereas the differences between the two NNs are less significant over the tropics. The difference between the OMITROPO3-NN and the NN trained using only ancillary data becomes more evident if the performances of the two NNs are evaluated with respect to the TCO anomaly. Figure 3.10 shows the TCO anomalies estimated by this second NN, compared with those measured by the ozonesondes. The correlation coefficient between the actual and the estimated TCO anomalies decreases from 0.72 to 0.58. Comparing Fig. 3.10 with Fig. 3.8, it can be seen that the NN trained without OMI data has a tendency to drastically underestimate TCO anomalies larger than about 30%, whereas this tendency does not seem to be present in the OMITROPO3-NN. Table 3.6 summarizes the differences in the anomaly correlation coefficients between the two NNs for all the ozonesonde stations with at least 20 measurements. Again, it can be seen that the performances of the OMITROPO3-NN with respect to

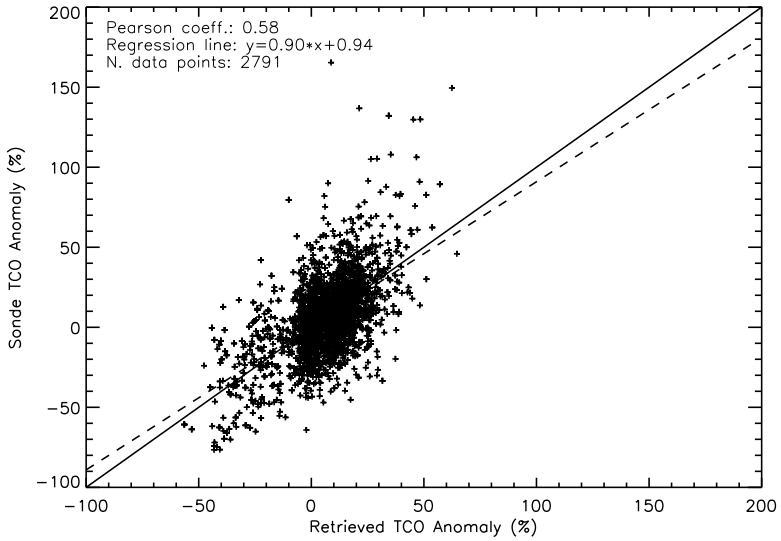

Figure 3.10: Comparison between actual and estimated TCO anomaly for the NN trained only with ancillary data.

this parameter are considerably better than those of the NN trained without OMI reflectances for almost all the ozonesonde stations.

Table 3.5: Results for the NN trained without OMI reflectances, divided by station, sorted by increasing latitude. Only stations with at least 20 measurements included in the $\mathcal{D}_{\text{test}}$ set were considered.

Station name	Lat.	Lon.	Bias (DU)	RMSE (DU)	Pearson	N. data
Amundsen (South Pole)	-89.98	0.00	0.48	6.55	0.83	26
Syowa	-69.00	39.58	-1.27	7.37	0.84	41
Davis	-68.58	77.97	1.62	5.90	0.81	169
Broadmeadows	-37.69	144.95	2.85	5.78	0.72	154
La Réunion	-21.08	55.48	-2.12	7.09	0.74	64
Suva (Fiji)	-18.13	178.32	1.21	4.80	0.56	28
Ascension Island	-7.98	-14.42	-2.15	5.73	0.73	144
Watukosek (Java)	-7.57	112.65	0.32	5.95	0.42	37
Maxaranguape (Natal)	-5.45	-35.33	-0.57	5.04	0.77	121
Nairobi	-1.27	36.80	-1.83	4.68	0.64	23
San Cristobal	-0.92	-89.60	3.05	5.83	0.66	44
Barbados	13.16	-59.43	-2.21	6.19	-0.06	21
Hong Kong Observatory	22.31	114.16	-0.13	7.37	0.47	21
Naha	26.20	127.68	-1.33	6.37	0.72	28
Huntsville	34.72	-86.64	-0.69	5.31	0.85	143
Tateno-Tsukuba	36.06	140.10	-2.56	10.08	0.81	24
Madrid (Barajas)	40.46	-3.65	0.04	5.31	0.78	33
L'Aquila	42.38	13.31	1.09	5.99	0.75	35
Sapporo	42.56	141.33	1.60	5.49	0.87	130
Haute Provence	43.93	5.70	2.09	7.19	0.69	146
Egbert	44.23	-79.78	1.16	5.73	0.77	136
Payerne	46.49	6.57	-2.00	6.85	0.51	60
Hohenpeissenberg	47.80	11.02	-0.26	3.88	0.75	52
Regina (Bratt's Lake)	50.21	-104.71	0.36	4.74	0.64	212
Valentia Observatory	51.93	-10.25	-2.83	5.02	0.74	22
Lindenberg	52.16	14.12	-4.19	5.77	0.60	22
Goose Bay	53.30	-60.36	1.12	5.28	0.70	234
Whitehorse	60.70	-135.07	-3.24	7.05	0.33	34
Yellowknife	62.50	-114.48	-2.63	5.13	0.43	21
Salekhard	66.50	66.70	-5.55	7.76	0.47	84
Sodankyla	67.34	26.51	-4.43	7.15	0.45	207
Scoresbysund	70.49	-21.98	-8.27	10.14	0.32	25

Table 3.6: Pearson correlation coefficients between observed and estimated TCO anomalies for the OMITROPO3-NN and for the NN trained without OMI reflectances, divided by station, sorted by increasing latitude. Only stations with at least 20 measurements included in the $\mathcal{D}_{\text{test}}$ set were considered.

Station name	Lat.	Lon.	OMI-NN	Ancillary NN	N. data
Amundsen (South Pole)	-89.98	0.00	0.93	0.42	26
Syowa	-69.00	39.58	0.78	0.65	41
Davis	-68.58	77.97	0.82	0.73	169
Broadmeadows	-37.69	144.95	0.68	0.63	154
La Réunion	-21.08	55.48	0.51	0.30	64
Suva (Fiji)	-18.13	178.32	0.15	0.06	28
Ascension Island	-7.98	-14.42	0.29	0.12	144
Watukosek (Java)	-7.57	112.65	0.64	-0.13	37
Maxaranguape (Natal)	-5.45	-35.33	0.27	0.11	121
Nairobi	-1.27	36.80	0.52	-0.12	23
San Cristobal	-0.92	-89.60	0.54	0.27	44
Barbados	13.16	-59.43	0.40	0.00	21
Hong Kong Observatory	22.31	114.16	0.58	0.21	21
Naha	26.20	127.68	0.58	0.57	28
Huntsville	34.72	-86.64	0.58	0.37	143
Tateno-Tsukuba	36.06	140.10	0.81	0.60	24
Madrid (Barajas)	40.46	-3.65	0.61	0.55	33
L'Aquila	42.38	13.31	0.33	0.00	35
Sapporo	42.56	141.33	0.70	0.71	130
Haute Provence	43.93	5.70	0.42	0.25	146
Egbert	44.23	-79.78	0.67	0.53	136
Payerne	46.49	6.57	0.65	0.33	60
Hohenpeissenberg	47.80	11.02	0.46	0.47	52
Regina (Bratt's Lake)	50.21	-104.71	0.72	0.54	212
Valentia Observatory	51.93	-10.25	0.80	0.59	22
Lindenberg	52.16	14.12	0.30	0.27	22
Goose Bay	53.30	-60.36	0.65	0.56	234
Whitehorse	60.70	-135.07	0.49	0.50	34
Yellowknife	62.50	-114.48	0.61	0.35	21
Salekhard	66.50	66.70	0.50	0.51	84
Sodankyla	67.34	26.51	0.57	0.40	207
Scoresbysund	70.49	-21.98	0.53	0.25	25

3.5 Case studies: 17th and 26th August 2006

3.5.1 Global retrievals

Besides carrying out a validation against ozonesondes, it is important to see how reasonable are the TCO spatial patterns obtained by applying the OMITROPO3-NN to an extended area (e.g. an OMI orbit, or the entire globe). In this section, two examples of global TCO retrievals are discussed.

In Fig. 3.11, global TCO fields retrieved by the OMITROPO3-NN algorithm on 17th (top) and 26th (bottom) August 2006 – expressed in Dobson Units – are shown. The grey areas – where no retrieval is provided – are either non-sunlit areas, areas where the cloud fraction exceeded the 30% threshold, or areas over which the quality criteria imposed on the OMI spectra (Sect. 3.2.3) were not satisfied. Apart from a striping effect that can be noticed in the along-track direction, a visual inspection of the results indicates that reasonable synoptic patterns can be identified. It is likely that the stripes are caused by several types of noise in the irradiance data, and that the effect can be partly mitigated by replacing standard irradiance products with composite products such as multi-year means, as explained by *Veihelmann and Kleipool* (2006). It must be noted, however, that in the ozone profile retrieval algorithm by *Liu et al.* (2010) the use of multi-year mean irradiance did not solve the problem completely, because also the radiometric calibration of the OMI radiances contributes to the striping effect.

Another feature that sometimes appears is represented by some abrupt meridional gradients in the retrieved TCOs (see, e.g., the northern edge of the "red" region in the Central Asia on 17th August 2006, above panel in Fig. 3.11). This might be due to the coarse resolution of either the tropopause or the *a priori* fields used as inputs in the OMITROPO3-NN.

The day of 26th August has been chosen as a sample date also because it allows a visual comparison with a TCO map shown in the paper by *Liu et al.* (2010). For the reader's convenience, such map is reported in Fig. 3.12. A similar color scale was used in Figures 3.11 and 3.12 in order to facilitate visual comparisons. For instance, it can be noticed that the ozone peak between southern Brazil, northern Argentina and Paraguay is reproduced quite well by the OMITROPO3-NN algorithm. The same holds for the high ozone areas around the Azores, the Eastern coast of the United States, the Black Sea, off the coast of the southwestern Africa and south of the Madagascar. Also the ozone patterns over Australia look similar. The main differences exist over North Africa, where the OMITROPO3-NN seems to

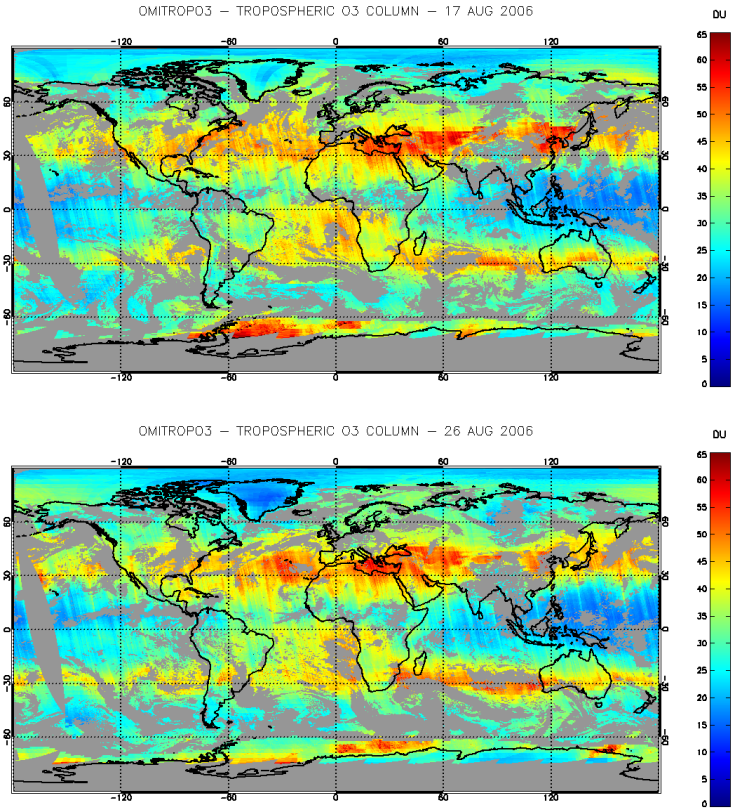

Figure 3.11: Global tropospheric ozone fields retrieved by the OMITROPO3-NN algorithm on August 17th (*top*) and 26th (*bottom*), 2006. No retrieval was performed on pixels with cloud fraction greater than 30%.

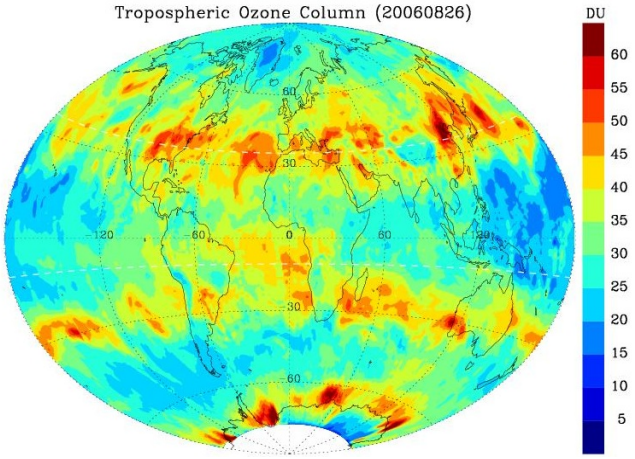

Figure 3.12: Global tropospheric ozone field on 26th August 2006 as shown in *Liu et al.* (2010). From http://www.cfa.harvard.edu/atmosphere/ozone_tropo.html.

yield larger ozone values, and over central Asia, where the OMITROPO3-NN seems to yield a more extended area of large TCO than *Liu et al.* (2010). Unfortunately, no correlative measurements over these areas were found to assess which of the two algorithms performed better.

3.5.2 Comparisons with the TM5 Chemistry and Transport Model

In order to have a more quantitative assessment, the TCO fields retrieved on 17th and 26th August 2006 were compared to TCO fields simulated using the Chemistry and Transport Model (CTM) TM5 (*Krol et al.*, 2005; *Williams et al.*, 2012). The model provided simulated ozone fields at 34 pressure levels, on a grid of 3° in longitude by 2° in latitude. In order to perform the comparison, both the NCEP tropopause pressure and the TCO fields retrieved by the OMITROPO3-NN were mapped on the same grid. The remapping has been done by selecting all the OMI pixels whose center lie within each TM5 grid cell, and associating the median non-missing TCO to the cell. The NCEP tropopause pressure was used as upper integration limit for the TM5 simulated ozone profiles.

The TCO fields simulated using TM5 on the two dates are shown in Fig. 3.13 and scatter plots of modeled versus retrieved TCOs are shown in

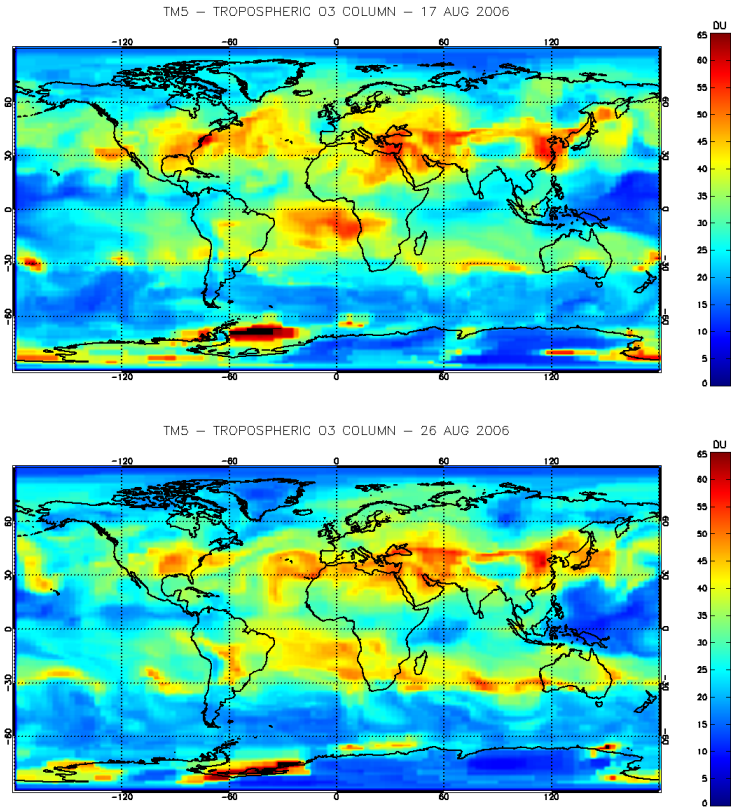

Figure 3.13: Global tropospheric ozone fields simulated by the TM5 CTM on August 17th (*top*) and 26th (*bottom*), 2006.

Fig. 3.14. Such statistics show that the OMITROPO3-NN has a positive bias of about 4 DU with respect to TM5. The Pearson correlation coefficient between the TCO fields is slightly larger than 0.80 for both the dates.

The structure of the differences between the OMITROPO3-NN and the TM5 estimates is shown with more detail in Figs. 3.15 and 3.16, where the histograms of the absolute and the relative differences are depicted, respectively.

Figure 3.17 shows a map of the NN − TM5 absolute differences for the two dates under study.

It can be noticed that spatial patterns in the differences between OMITROPO3-NN and TM5 exist. In particular, higher TCO values than TM5 are regularly retrieved by the OMITROPO3-NN over the southern midlatitudes. The underestimations are mostly concentrated between the Tropics and,

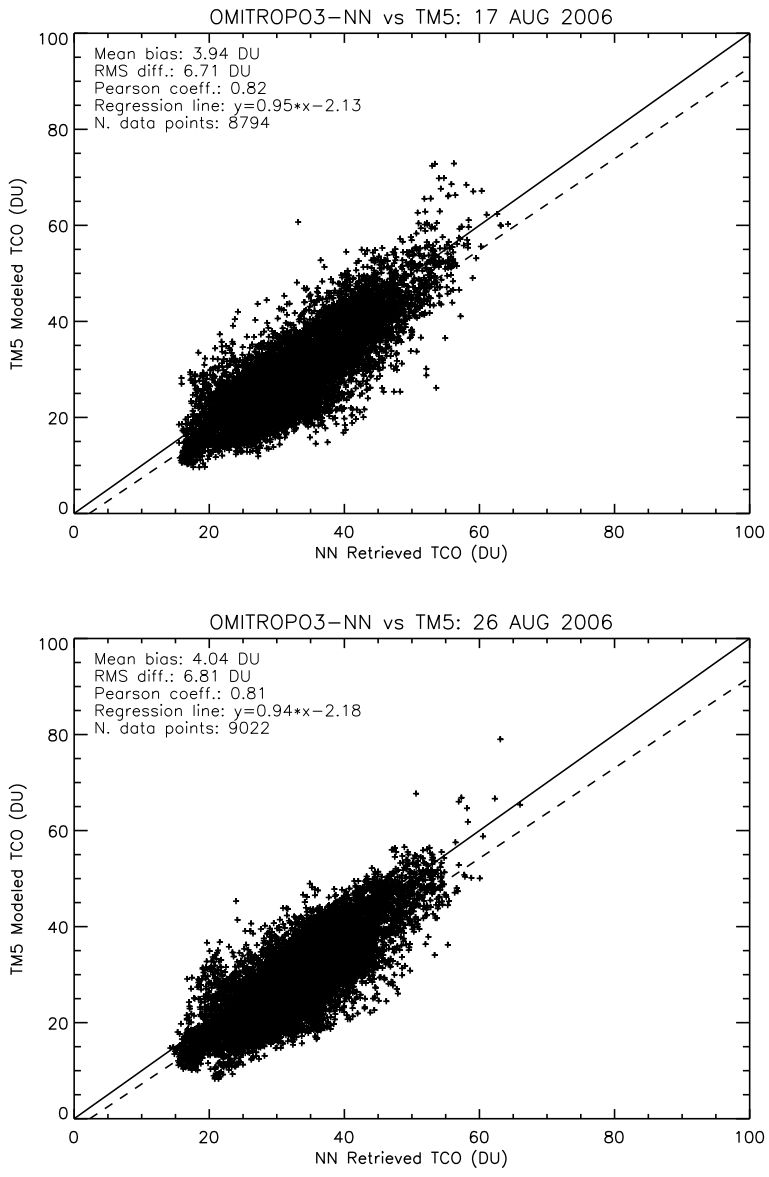

Figure 3.14: Scatter plots of the OMITROPO3-NN retrievals versus the TM5 TCO simulations on August 17th (*top*) and 26th (*bottom*), 2006. The OMITROPO3-NN TCO fields were remapped on the TM5 grid.

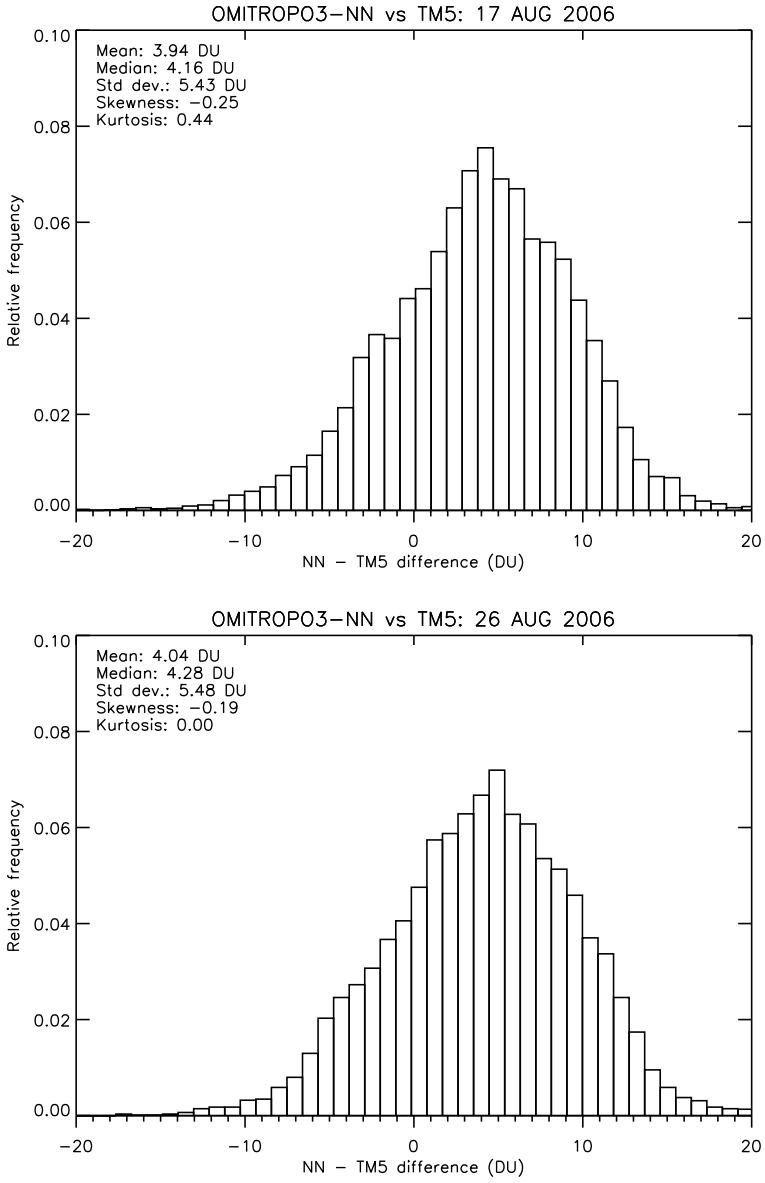

Figure 3.15: Histograms of the absolute differences between the OMITROPO3-NN retrievals and the TM5 TCO simulations on August 17th (*top*) and 26th (*bottom*), 2006. The OMITROPO3-NN TCO fields were remapped on the TM5 grid.

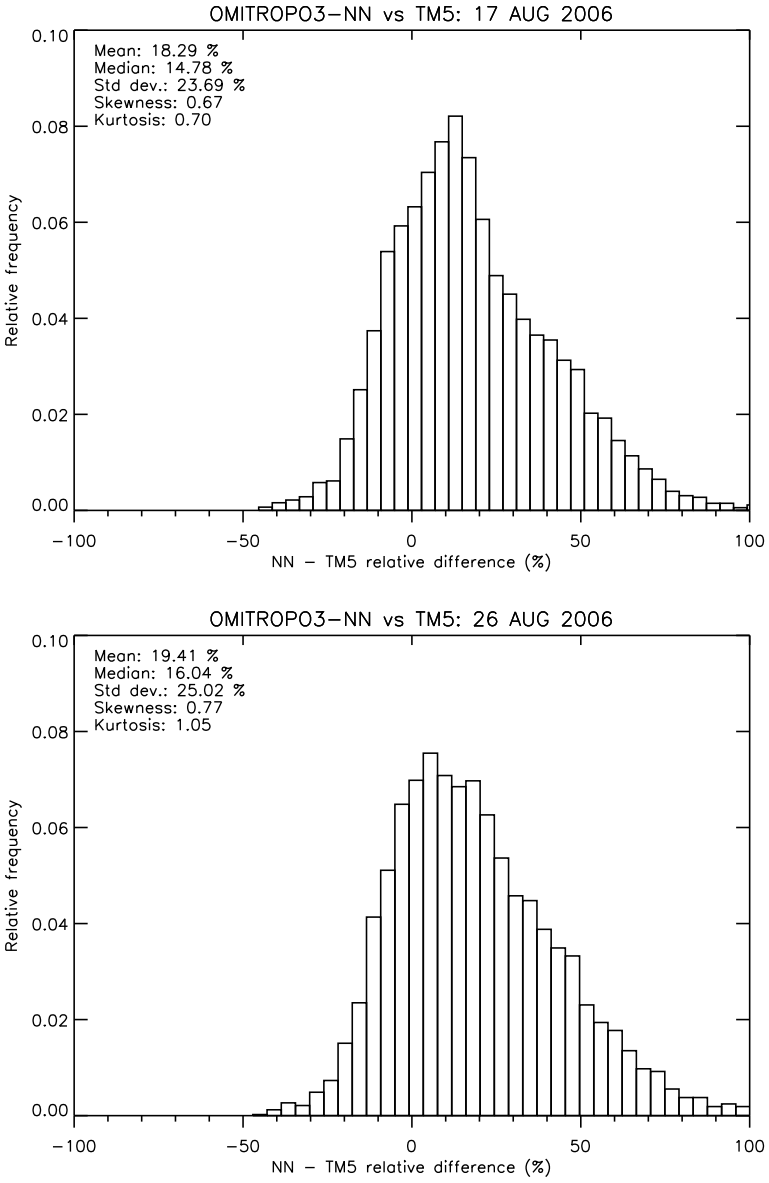

Figure 3.16: Histograms of the relative differences between the OMITROPO3-NN retrievals and the TM5 TCO simulations on August 17th (*top*) and 26th (*bottom*), 2006. The OMITROPO3-NN TCO fields were remapped on the TM5 grid.

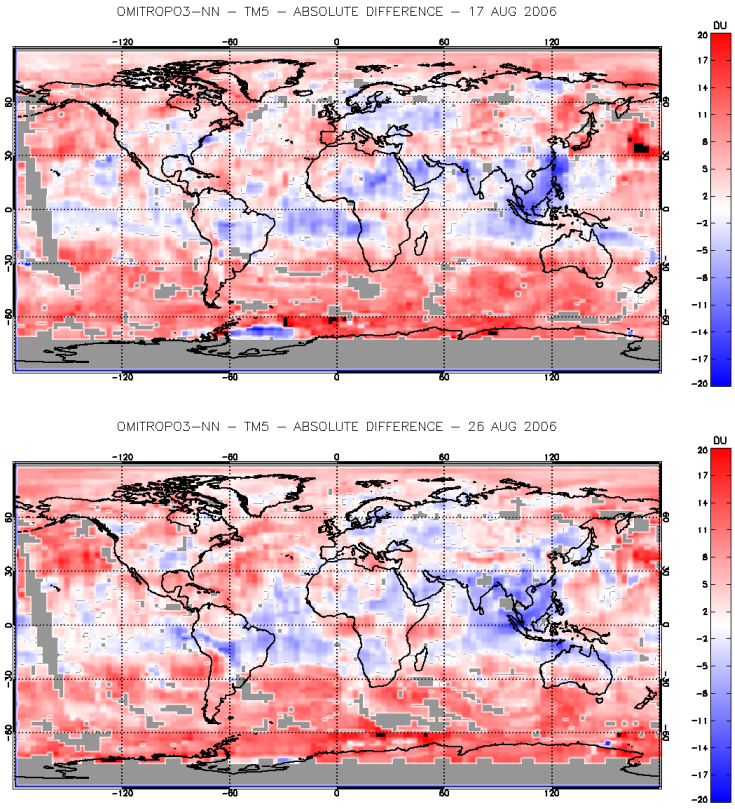

Figure 3.17: Maps of the absolute differences between OMITROPO3-NN and TM5 TCO fields on August 17th (*top*) and 26th (*bottom*), 2006. The OMITROPO3-NN TCO fields were remapped on the TM5 grid.

to a lesser extent, over central Europe and eastern United States. Large underestimations occur over Southeastern Asia.

Similar analyses performed during individual days in October 2006 gave similar results (*Di Noia et al.*, 2012a,b).

3.5.3 Retrieval sensitivity to tropopause pressure

Whenever a retrieval algorithm is developed, it is important to assess its sensitivity to its input quantities. In the case of NNs, a powerful way to do this is represented by the analysis of the NN input Jacobians, i.e. the derivatives of the NN model $\Phi_{\mathbf{W}^*}$ with respect to its inputs $\vec{x}$. An important property of single hidden layer NNs is that their input Jacobians can be

written analytically (*Blackwell and Chen*, 2009).

Since NN mappings are nonlinear, a difficulty in using their Jacobians for sensitivity analyses lies in the fact that they are input dependent. One method to overcome this difficulty is to use the Jacobian to define a NN Sensitivity Factor (SF) of an output y_j with respect to an input x_i as the ratio between the fractional change of y_j with respect to its actual value, and the corresponding fractional change of x_i:

$$\mathrm{SF}_j(x_i) = \frac{dy_j/y_j}{dx_i/x_i} = \frac{x_i}{y_j} \cdot \frac{dy_j}{dx_i}. \tag{3.2}$$

As an example of the application of the NN Jacobians to the OMITROPO3-NN, its derivative with respect to the tropopause pressure was derived. It can be expected that the tropopause information plays an important role in the tropospheric ozone retrieval, especially outside the Tropics, given the appreciable degree of correlation between the tropopause height and the TCO (*de Laat et al.*, 2005). Thus, it is interesting to assess whether this kind of knowledge is well incorporated in the OMITROPO3-NN.

Two maps of the algorithm SF with respect to the tropopause pressure – for 17th and 26th August 2006 – are shown in Fig. 3.18. It can be seen that the SF always assumes negative values. This result is reasonable, because it indicates that the negative correlation between tropopause pressure and TCO is captured by the NN model. Furthermore, the SF absolute values tend to increase going from Tropics toward Poles. An increase of |SF| indicates a larger sensitivity of the retrieved TCO to the tropopause pressure. The increase in |SF| is not symmetric with respect to the Equator, because of the motion of the Intertropical Convergence Zone (ITCZ) with the season. This could be an indication that the retrievals at midlatitudes are more sensitive to the tropopause pressure during winter.

3.6 Outline

A new neural network algorithm to retrieve tropospheric ozone from OMI data at global scale – named OMITROPO3-NN – has been presented. The OMITROPO3-NN inherits from previous work and adds novel characteristics like the global coverage, the use of tropopause information to better demarcate the actual troposphere, and the incorporation of ancillary data and a priori information into the NN input vector, in order to improve the retrieval accuracy. As a result, the OMITROPO3-NN provides daily global estimates of the tropospheric ozone column.

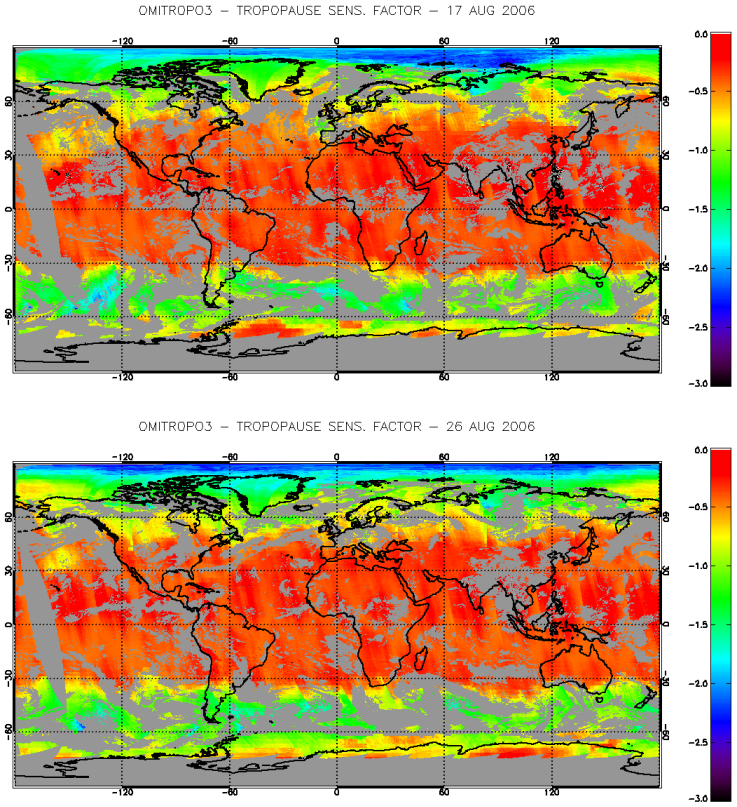

Figure 3.18: Global fields of the tropopause sensitivity factor computed for the OMITROPO3-NN algorithm on August 17th (*top*) and 26th (*bottom*), 2006.

The algorithm has been validated against ozonesondes and CTM simulations, and encouraging results have been obtained. Overall, the NN appears to be capable of determining the spatial and temporal TCO variability.

The OMITROPO3-NN retrievals were first compared to ozonesonde measurements collected in several geographical locations around the globe, both during and after the time period covered by the training set. As for the latter point, it was found that the OMITROPO3-NN performs reasonably well also after the training period, even though a slight increase in the global retrieval bias seems to be present.

Over all the latitude bands except the Arctic, a relatively low bias against the ozonesonde measurements was noticed. The correlation coefficients between retrieved and measured tropospheric ozone columns range approximately between 0.75 and 0.85, and the RMS errors are between 5 and 6 DU. On the other hand, over the Arctic a larger negative bias was detected, whose cause is a topic of ongoing research.

The ozonesonde data were also used in order to assess the capability of the OMITROPO3-NN to detect and estimate departures of the tropospheric ozone columns from their climatological values. A global correlation coefficient of about 0.70 was found between the actual and the retrieved relative anomalies. A geographical analysis of this correlation coefficient seems to suggest that the anomaly estimation capability of the OMITROPO3-NN over the Tropics is worse than at other latitudes. This may indicate that an insufficient training was obtained in this latitude band, due to the relatively low number of available ozonesonde data. Future versions of the algorithm will have to address this problem properly. A possible approach may consist in complementing ozonesonde data with radiative transfer simulations in tropical scenarios. Another alternative is the relaxation of co-location criteria over the Tropics.

In order to assess the contribution of OMI reflectances to the retrievals, a second NN was trained using only the ancillary data. The estimation capabilities of this second NN were shown to be worse than those of the OMITROPO3-NN, especially in the estimation of TCO anomalies.

After the comparison with ozonesonde data, examples of operational use of the OMITROPO3-NN were provided. The tropospheric ozone fields retrieved by the OMITROPO3-NN in two dates during August 2006 were compared with simulations made with the TM5 CTM. Such comparisons suggest that the OMITROPO3-NN has a bias of about 4 DU with respect to TM5. However, the differences between retrieved and simulated tropospheric ozone fields exhibit a peculiar geographic pattern, with the OMITROPO3-NN that overestimates TM5 simulations over southern midlatitudes and underesti-

mates between the Tropics. Despite this, the simulated global spatial patterns are fairly well reproduced by the OMITROPO3-NN, as shown by the correlation coefficients, which are higher than 0.80.

In addition to providing daily fields of the tropospheric ozone column, the OMITROPO3-NN product also stores the input Jacobians of the neural model, which can be useful to evaluate its sensitivity to the input variables, as well as to assess how well the NN is incorporating the knowledge of the relationships between the input and output variables. Examples of the retrieval derivative with respect to the tropopause pressure show that the OMITROPO3-NN seems to capture the tropospheric ozone sensitivity to the tropopause pressure in a physically meaningful way. A similar procedure can be applied to evaluate the NN sensitivity to all the input quantities for every retrieval.

While the OMITROPO3-NN generally shows high correlations and low RMS errors with respect to ozonesondes compared to other existing satellite products (*Schoeberl et al.*, 2007; *Thompson et al.*, 2012), a possible drawback of the current version of the algorithm is its massive use of ancillary information to complement the OMI radiometric measurements. This was necessary in order to constrain the retrieval problem properly, as UV measurements may not have enough sensitivity to directly retrieve tropospheric ozone without a priori constraints.

Acknowledgements

All the PIs of the ozonesonde stations whose data were used in this work are gratefully acknowledged. WOUDC, NDACC and SHADOZ data have been downloaded from the respective websites, and are publicly available. The NCEP Reanalysis data are provided by the NOAA/OAR/ESRL PSD, Boulder, Colorado, USA, from their website at http://www.esrl.noaa.gov/psd/. ISAC-CNR, ReSMA-Italian Air Force and CETEMPS are acknowledged for the provision of Italian ozonesonde data. The ozone monitoring activities of CETEMPS are partly funded by the Italian Ministero dell'Ambiente e della Tutela del Territorio e del Mare.
Marco Iarlori (CETEMPS) is gratefully acknowledged for his help with L'Aquila ozonesonde station data, Marco Cervino (ISAC-CNR) is gratefully acknowledged for his help with San Pietro Capofiume ozonesonde station data. Stefania Vergari and Emanuele Vuerich (ReSMA, Italian Air Force) are gratefully acknowledged for their help with Vigna di Valle ozonesonde data. Michael Yan (NASA Aura Validation Data Center) is gratefully ac-

knowledged for providing the OMTO3 overpass files for the stations Barbados, Maxaranguape, Whitehorse and Yellowknife upon request.
Several people from the Climate Observations Department of the Royal Netherlands Meteorological Institute are acknowledged for valuable discussions that helped improve this work significantly.

Chapter 4

A neural network algorithm to retrieve ozone profiles from OMI data

4.1 Introduction

The most widespread methods to extract ozone profile information from spectral reflectance measurements involve an iterative fitting of a modeled reflectance spectrum, aimed at selecting the ozone profile that minimizes a cost function that takes into account the difference between the modeled and the observed spectrum, as well as additional information. Such additional information may have the form of a measure of the "likelihood" of the retrieved profile, according to prior knowledge about the local and seasonal statistics of the ozone profile, as in the case of optimal estimation (OE) methods (*Rodgers*, 2000); or a measure of its "smoothness", as in the Phillips-Tikhonov regularization (PTR) method (*Hasekamp and Landgraf*, 2001; *Doicu et al.*, 2010b).

These retrieval techniques have a sound theoretical foundation, but they are computationally intensive, because they require multiple runs of a radiative transfer model (RTM) for each retrieval. This is a limiting factor for the processing of the large wealth of data provided by the most recent hyperspectral sounders. For example, the Ozone Monitoring Instrument (OMI, *Levelt et al.*, 2006b) observes the Earth's atmosphere with a nominal nadir spatial resolution of 13×24 km^2 and a swath of 2400 km^2. As a consequence, each orbit of OMI data consists of 60 cross-track pixels multiplied by more than 1600 swaths. The current processing capabilities make it difficult to apply

the above mentioned retrieval techniques to all the pixels of an OMI orbit with a reasonable computation time. In fact, in the official ozone profile Level 2 product for OMI, only one every five swaths is processed (*Kroon et al.*, 2011).

In this chapter, an alternative algorithm for the retrieval of ozone profiles from OMI data is proposed. Such algorithm is based on Neural Networks (NNs). The main advantage of NNs in the framework of atmospheric sounding is their computational speed. Since the use of NNs avoids the need for iterated RTM simulations during the operational phase, it is possible to generate an ozone profile product that exploits the full spatial resolution of OMI, and has also the potential of being delivered in near real time.

In this first experimental version, we trained our NN with OMI reflectance spectra and ozonesonde data. As a consequence, the output of our product is not the entire ozone profile, because the top pressure level is limited to 10 hPa. In the operational version of this product, the full ozone profile should be given as output. This can be accomplished either by training the NN with synthetic data or by complementing ozonesonde profiles with high vertical resolution stratospheric profiles measured by satellite limb sounders. Microwave Limb Sounder (MLS) Level 2 data would be particularly well suited for the latter purpose, because the MLS is installed on the same satellite platform as OMI.

This chapter is organized as follows. In Section 4.2 the general setup of the NN algorithm is discussed. In Section 4.3 retrieved ozone profiles are compared to ozonesonde data not used during the NN training phase, in order to obtain an insight on the algorithm performances with respect to ozone profile and ozone column retrievals. The analysis is split by latitude and season, and also results over some individual locations are shown. In Section 4.4 conclusions are drawn, and further ideas for future work are pointed out.

4.2 Methodology

The NN algorithm proposed here has some similarities with the Neural Network Ozone Retrieval System (NNORSY) approach proposed by *Müller et al.* (2003) for Global Ozone Monitoring Experiment (GOME) data, as well as some differences. The main similarity is the fact that OMI spectral measurements are combined with external information about the temperature profile. The main difference lies in the fact that in our algorithm the OMI reflectance spectra are preliminarly compressed via a Principal Com-

Table 4.1: Definition of the output layers for the ozone profile retrieval NN.

Layer Nr.	Bottom pressure (hPa)	Top pressure (hPa)
1	1000	700
2	700	600
3	600	500
4	500	400
5	400	300
6	300	250
7	250	200
8	200	150
9	150	100
10	100	70
11	70	50
12	50	30
13	30	20
14	20	10

ponent Analysis (PCA) before being used as inputs for the NN, whereas in the NNORSY approach the full spectral information is directly fed to the NN. Furthermore, in our algorithm we do not use any time information in the input vector to correct for drifts in the instrument calibration. Neither do we use latitude and season as climatological inputs for the NN.

The input variables for the NN algorithm are 8 Principal Components (PCs) of the UV1 channel reflectance (280-308 nm), 20 PCs of the UV2 reflectance (312-345 nm), Solar Zenith Angle (SZA), View Zenith Angle (VZA), Relative Azimuth Angle (RAA), cloud fraction, cloud top pressure, reflectivity at 360 nm and NCEP/NCAR temperature profile. The output vector consists of ozone partial columns in 14 pressure layers – listed in Tab. 4.1 – measured in DU divided by $\Delta \ln p$, where p is the pressure and $\Delta \ln p$ is the difference in $\ln p$ between the bottom and the top pressure level of a layer.

The training, validation and test datasets for the NN were created by co-locating OMI reflectance spectra with ozonesonde measurements taken from WOUDC, SHADOZ, NDACC and several campaigns between October 2004 and April 2008. Later periods have not been considered because extracting the relevant data from the OMI dataset for co-locations would have required too much time.

In order to partially compensate for the unevenness in the latitudinal distribution of ozonesonde data, a latitude-dependent maximum tolerated co-location distance $d_{\max}$ has been set. In particular, $d_{\max}$ has been set to 100 km at the tropics and 50 km at the poles, and the following empirical relationship has been used

$$d_{\max}(\Lambda) = a \cdot \exp(-b\Lambda^2) \tag{4.1}$$

where Λ is the latitude of the ozonesonde station, $a = 100\,\text{km}$ and $b = 90/\sqrt{\ln 2}$.

The co-location procedure explained above has led to the generation of 259,880 input-output pairs, that were randomly split between the training, validation and test sets using a 70-15-15% subdivision.

During this preliminary phase of the development of the algorithm, we did not make the effort of optimizing the NN architecture in terms of the number of hidden layers and neurons. We just selected a reasonable architecture, with a single hidden layer and 25 neurons using an hyperbolic tangent activation function and a linear output layer. In the operational version of the algorithm, a more careful choice can be made.

4.3 Results

4.3.1 Profiles

Figures from 4.1 to 4.5 show plots of the median relative biases and the error standard deviations for the comparison with the ozonesonde profiles included in the test set. The relative errors have been defined as (OMI–Sonde)/Sonde*100%. Since the NN retrievals do not provide any formal Averaging Kernel (AK) information, no smoothing has been applied to the ozonesonde data before making the comparison. Nonetheless, defining the retrieved quantities as partial columns already implies a certain amount of smoothing. However, it is possible that convolving the computed partial column profiles with some smoothing function – e.g. following a similar approach to *Müller et al.* (2003) – can improve the comparisons to some extent, thereby giving an idea of the amount of smoothing that occurs during the inversion phase.

Separate statistics have been computed for different latitude bands and seasons. The following latitude bands have been defined: Antarctica (latitude lower than $-60°$), Arctic (latitude larger $60°$), northern midlatitudes (between $30°$ and $60°$), southern midlatitudes (between $-60°$ and $-30°$),

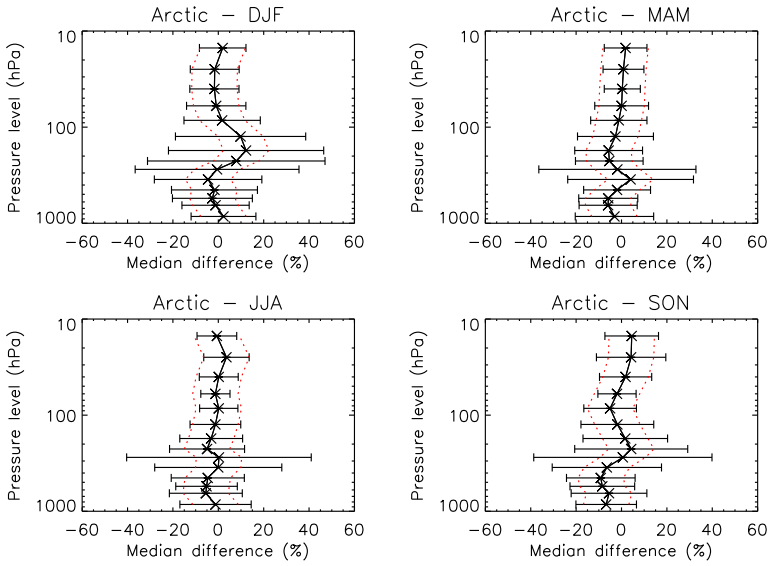

Figure 4.1: Profile of relative bias and error standard deviation for the comparison with Arctic ozonesondes, during the four seasons.

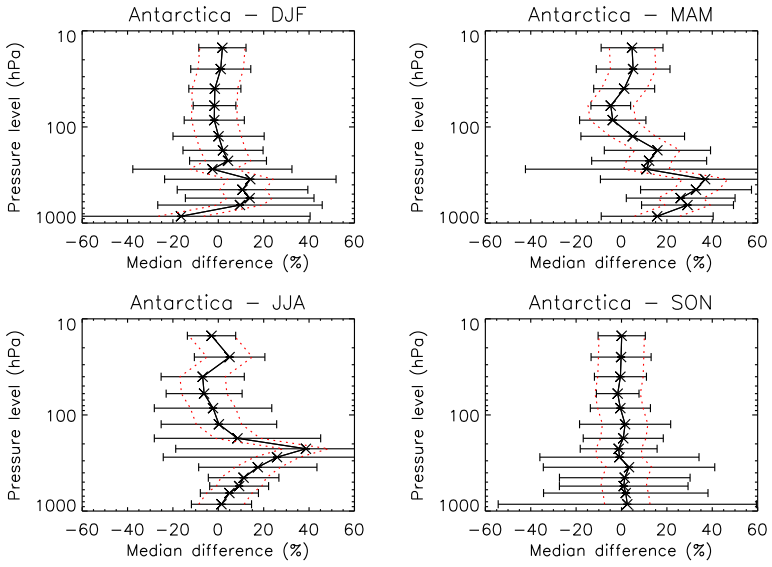

Figure 4.2: Profile of relative bias and error standard deviation for the comparison with Antarctic ozonesondes, during the four seasons.

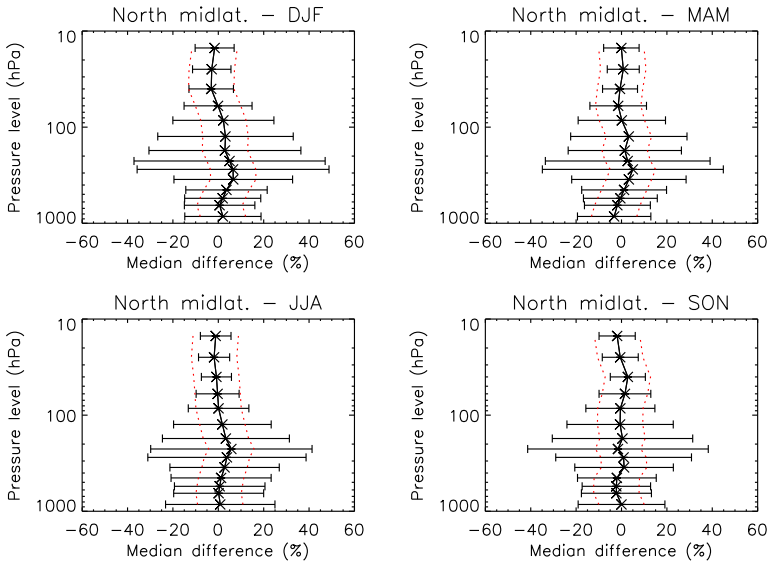

Figure 4.3: Profile of relative bias and error standard deviation for the comparison with ozonesonde at northern midlatitudes, during the four seasons.

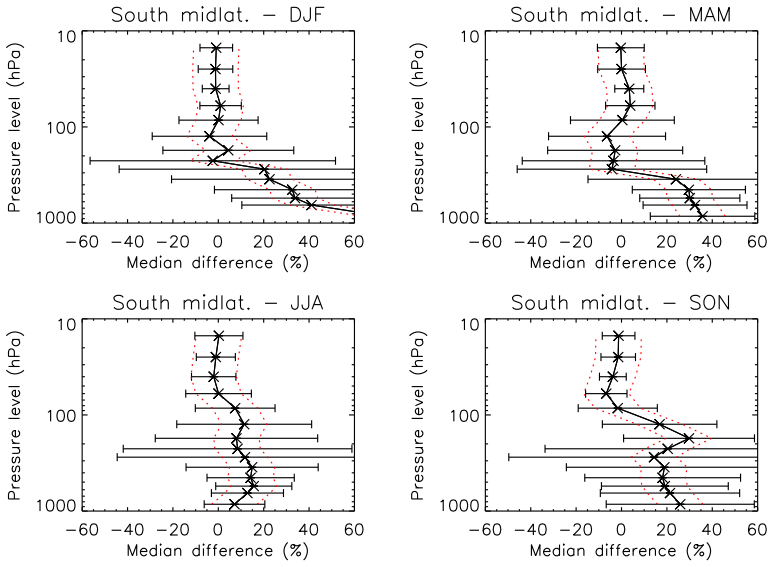

Figure 4.4: Profile of relative bias and error standard deviation for the comparison with ozonesonde at southern midlatitudes, during the four seasons.

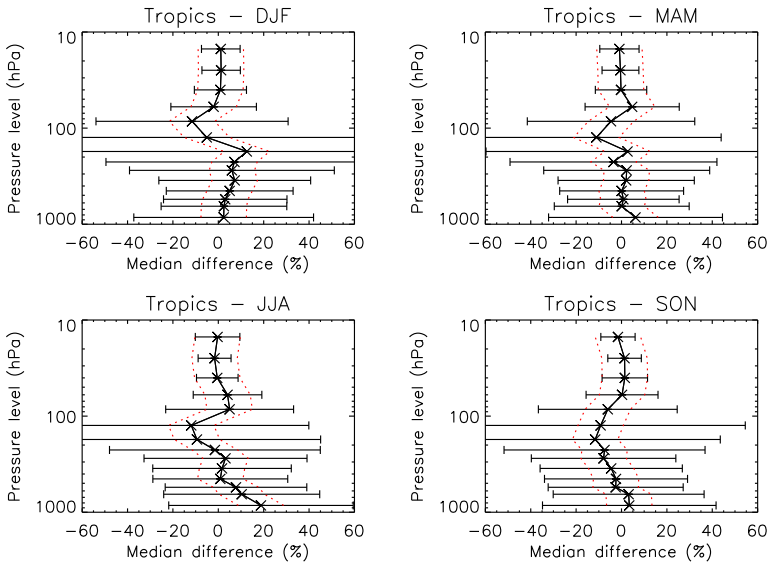

Figure 4.5: Profile of relative bias and error standard deviation for the comparison with tropical ozonesondes, during the four seasons.

and Tropics (between $-30°$ and $30°$). As for the definition of seasons, the months of the year have been grouped as follows: DJF (December, January, February), MAM (March, April, May), JJA (June, July, August) and SON (September, October, November). Overplotted are red dotted lines corresponding to deviations of $\pm 10\%$ with respect to the median errors.

As expected, the retrieval accuracy in the stratosphere is much better than in the troposphere in all cases. The accuracies in the four uppermost stratospheric levels – that is, above the 70 hPa pressure level – usually range between 10% and 15%, whereas larger errors are found in the troposphere and especially in the UTLS. In particular, large biases and uncertainties are observed in the troposphere over southern midlatitudes (except for JJA) and Tropics. It must be kept in mind, however, that low tropospheric ozone values are often observed over these areas (especially southern midlatitudes), and this makes large relative errors more likely. As for the stratosphere, the results seem to indicate a potential problem over Antarctica during JJA (relative accuracies considerably worse than 10%). This can be due to the rather high SZAs encountered over Antarctica during this period (almost always larger than $75°$).

The biases seem quite small in the stratosphere in almost all cases. For

the troposphere, instead, the results are dependent on latitude and season. For instance, very small biases are observed over Antarctica during SON and over northern midlatitudes in all the seasons, whereas very large biases are seen over southern midlatitudes (especially during DJF and MAM), and over the tropics during JJA. Moderate negative biases are seen over the Arctic, especially around 500 hPa. This might be an analogy with the results found for the tropospheric ozone NN algorithm OMITROPO3-NN (*Di Noia et al.*, 2013b), and could also clarify that such bias comes from that region of the troposphere, although the exact reasons for this behaviour are still unknown.

Looking at the error profiles, it is evident that the tropopause variability is a large source of uncertainty for the retrieved ozone values in the UTLS. This is a well known issue in most of the satellite ozone profile products (see, e.g., the results shown by *Liu et al.* (2005) for GOME, *Kroon et al.* (2011) for OMI, and *Delcloo and Tuinder* (2011) for GOME-2). A further evidence for this can be observed by comparing the plots in Figs. 4.1–4.5 with those in Figs. 4.6–4.10, that show histograms of the NCEP/NCAR tropopause pressure associated to the test ozonesonde data. It can be seen that the layers where the error bars are largest are approximately associated with the regions within which most of the tropopause variations occur. This is the case even for the Tropics, where the tropopause is quite stable between about 90 and about 120 hPa; however, it is possible that in this latter case the real reason for the large relative errors around the tropopause is represented by the low ozone concentrations that are often found in the tropical UTLS (*Kley et al.*, 1996). Furthermore, the existence of ozonesonde calibration issues in the tropical UTLS for low ozone values (*Vömel and Diaz*, 2010) suggests that care should be exercised in the interpretation of these ozonesonde data. Unfortunately, since the NN algorithm presented here is trained with ozonesonde data, this can also have an impact on the retrieved profiles. Should an operational NN ozone profile product be developed in the future, this issue should be considered with great care.

The aforementioned behaviour might be a further evidence for the fact that including tropopause information in ozone profile retrievals could reduce the retrieval uncertainties in the UTLS. In the context of NN retrievals, this could be achieved by directly feeding the tropopause pressure as an additional input to the NN, whereas for OE retrievals the use of a tropopause based ozone climatology as an *a priori* might play a similar role. This principle has been already demonstrated for OE ozone profile retrievals from Atmospheric Infrared Sounder (AIRS) observations (*Wei et al.*, 2010). For OMI, the results shown by *Bak et al.* (2013) seem to indicate that the use of a tropopause based climatology can significantly improve OMI ozone profile

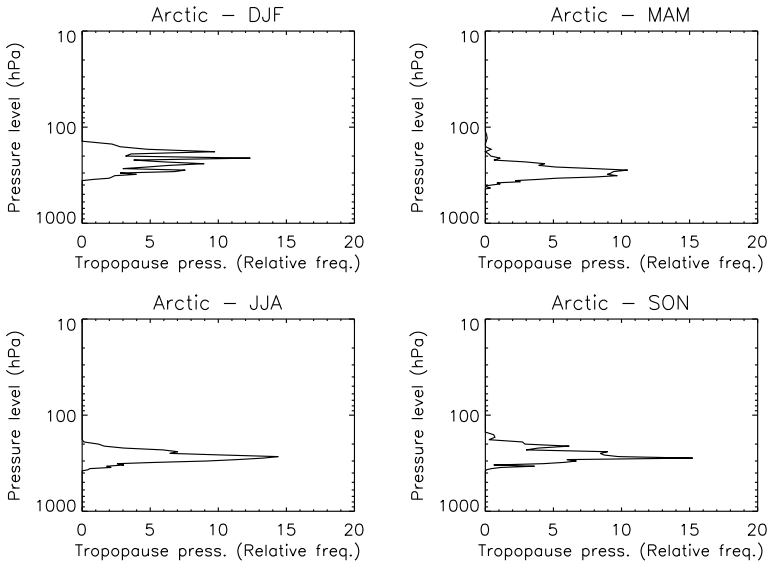

Figure 4.6: Histograms of the tropopause pressure for the Arctic ozonesondes, during the four seasons.

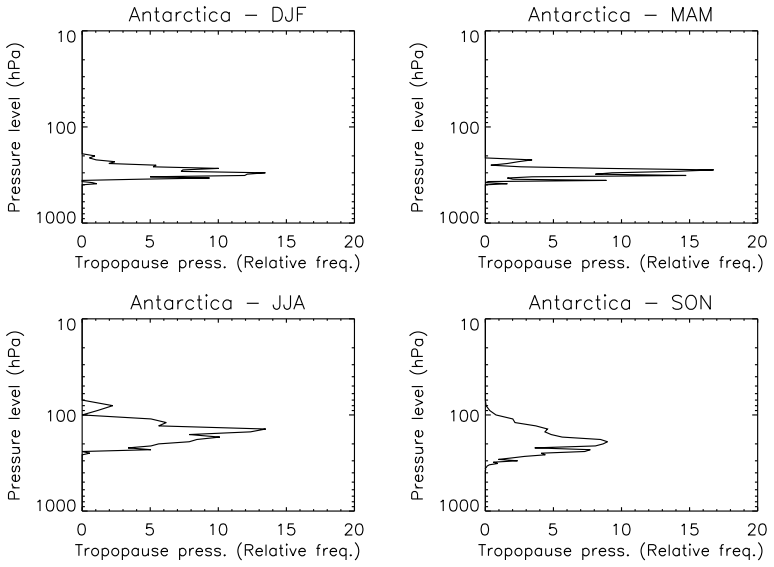

Figure 4.7: Histograms of the tropopause pressure for the Antarctic ozonesondes, during the four seasons.

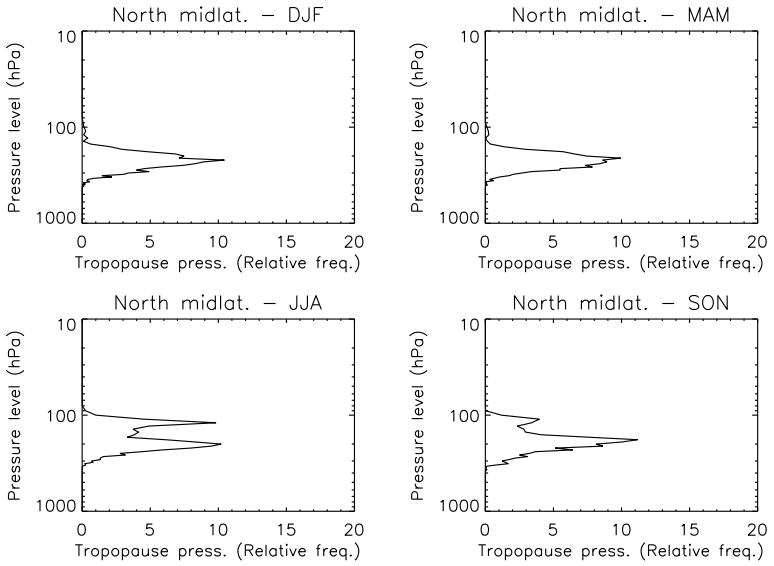

Figure 4.8: Histograms of the tropopause pressure for the northern midlatitude ozonesondes, during the four seasons.

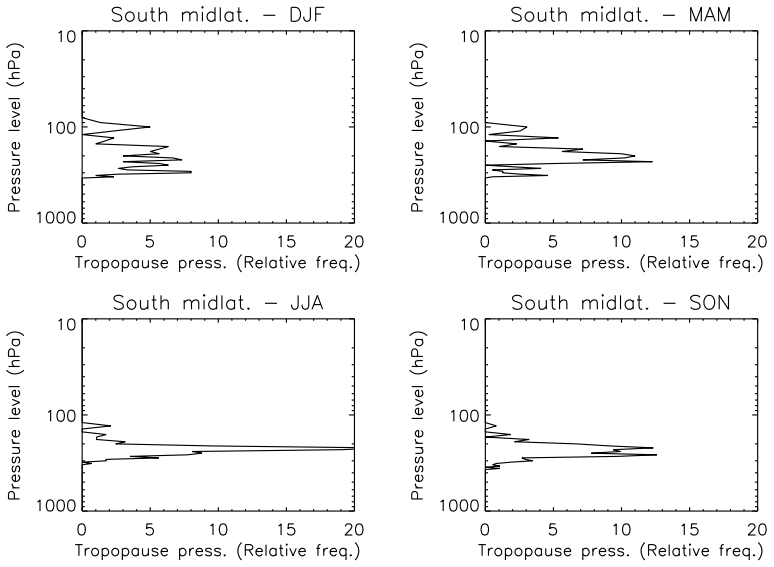

Figure 4.9: Histograms of the tropopause pressure for southern midlatitude ozonesondes, during the four seasons.

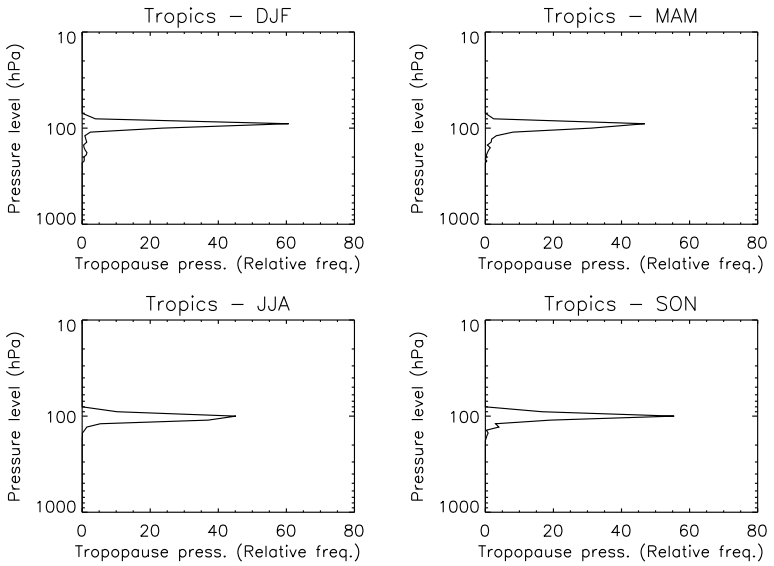

Figure 4.10: Histograms of the tropopause pressure for tropical ozonesondes, during the four seasons.

retrievals in the extratropical UTLS.

Figures from 4.11 to 4.20 show plots of the median relative biases and the error standard deviations over 10 individual stations (two per latitude band). Also red dotted lines corresponding to deviations of $\pm 10\%$ with respect to the median errors are plotted. The validation data seem to indicate that this requirement is approximately fulfilled, at least in the uppermost 4 layers (that is, for altitudes above the 70 hPa pressure level). Even looking at single Arctic stations (Figs. 4.11 and 4.12), the existence of a negative bias in the troposphere seems to be confirmed.

4.3.2 Integrated columns

Figures from 4.21 to 4.25 show scatter plots of retrieved versus measured integrated ozone columns from surface to 10 hPa, divided by latitude band and season. In most cases, small biases are observed, although variations with latitude and season exist.

In order to evaluate the quality of the integrated columns, a comparison with L2 total ozone columns may be useful. In Figs. from 4.26 to 4.30, scatter plots of the retrieved columns from 10 hPa against OMTO3 total ozone columns are shown. Also in this case, the results are stratified by latitude

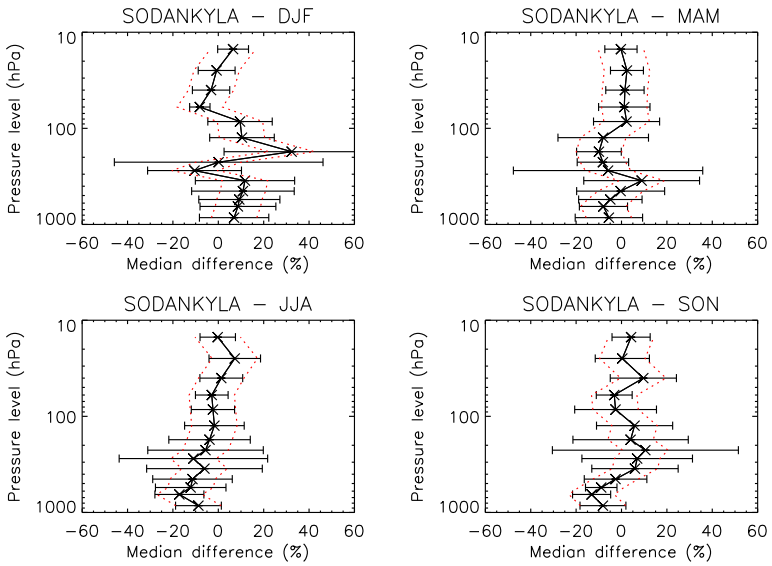

Figure 4.11: Profile of relative bias and error standard deviation for Sodankylä (Finland), during the four seasons.

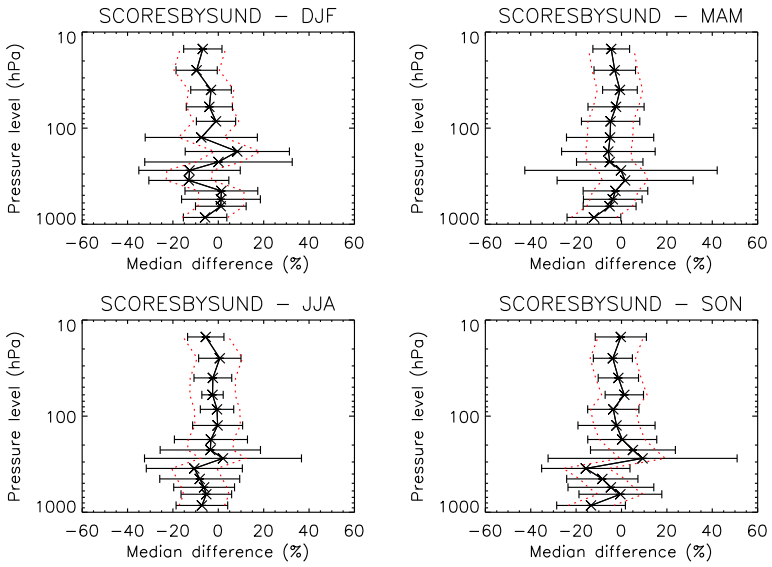

Figure 4.12: Profile of relative bias and error standard deviation for Scoresbysund (Greenland), during the four seasons.

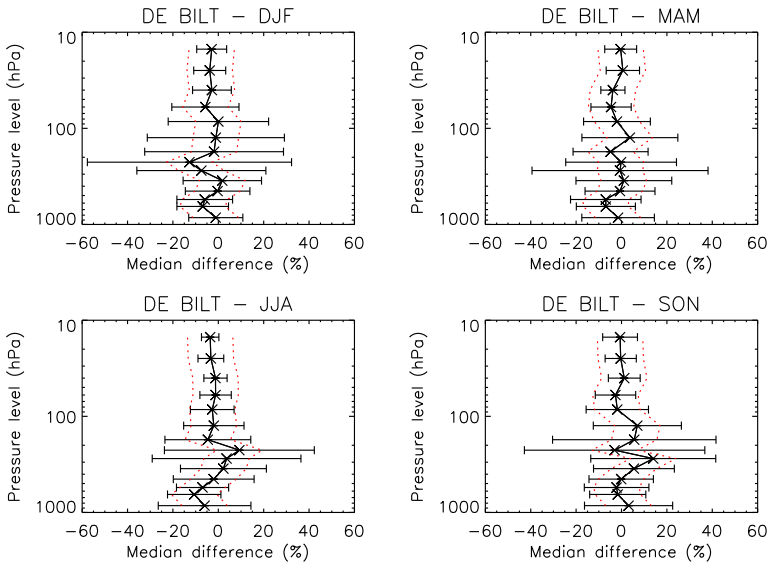

Figure 4.13: Profile of relative bias and error standard deviation for De Bilt (Netherlands), during the four seasons.

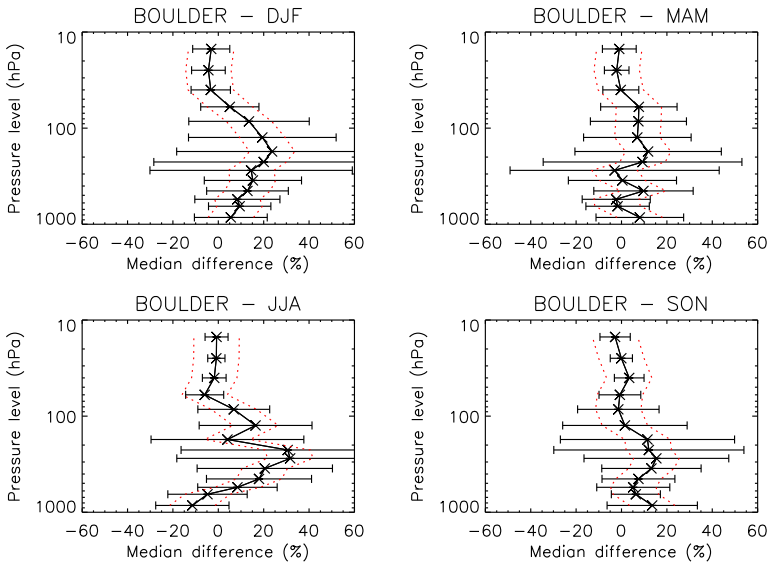

Figure 4.14: Profile of relative bias and error standard deviation for Boulder (United States), during the four seasons.

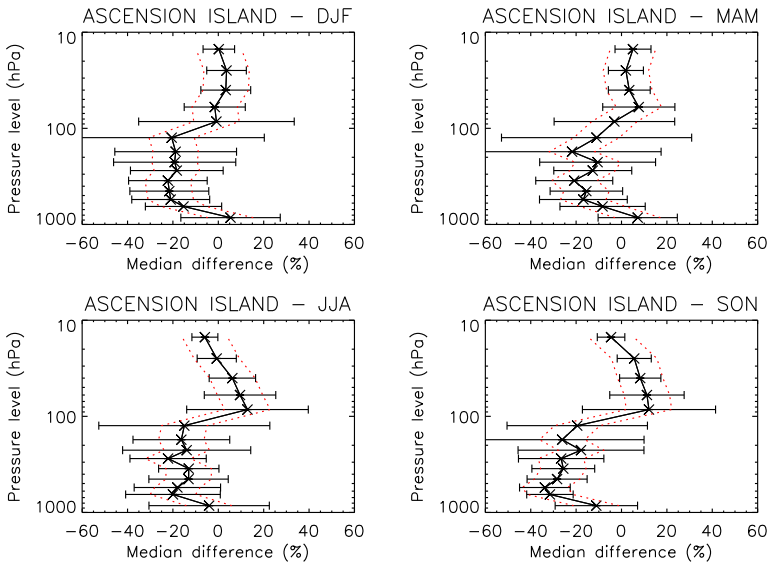

Figure 4.15: Profile of relative bias and error standard deviation for Ascension Island (Atlantic Ocean), during the four seasons.

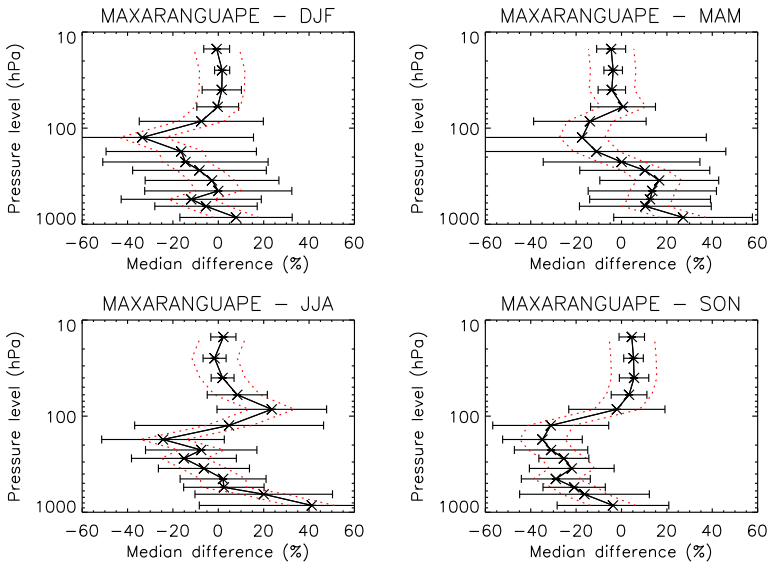

Figure 4.16: Profile of relative bias and error standard deviation for Maxaranguape (Brazil), during the four seasons.

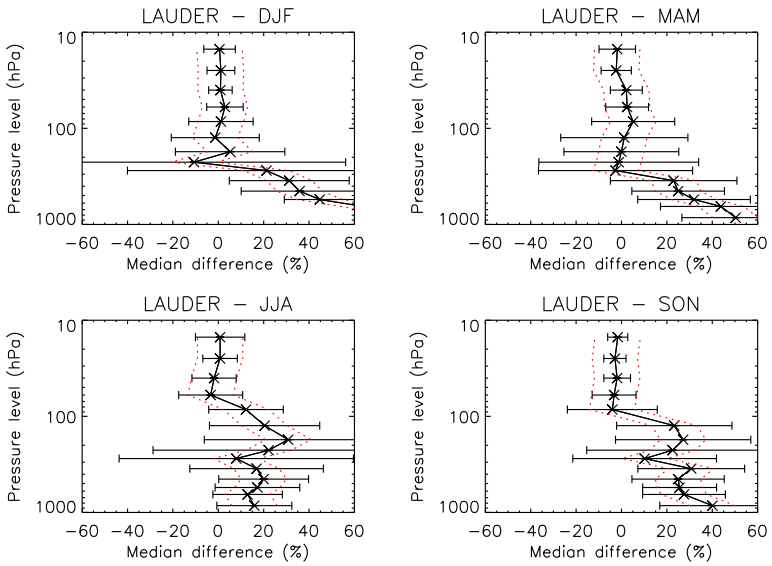

Figure 4.17: Profile of relative bias and error standard deviation for Lauder (New Zealand), during the four seasons.

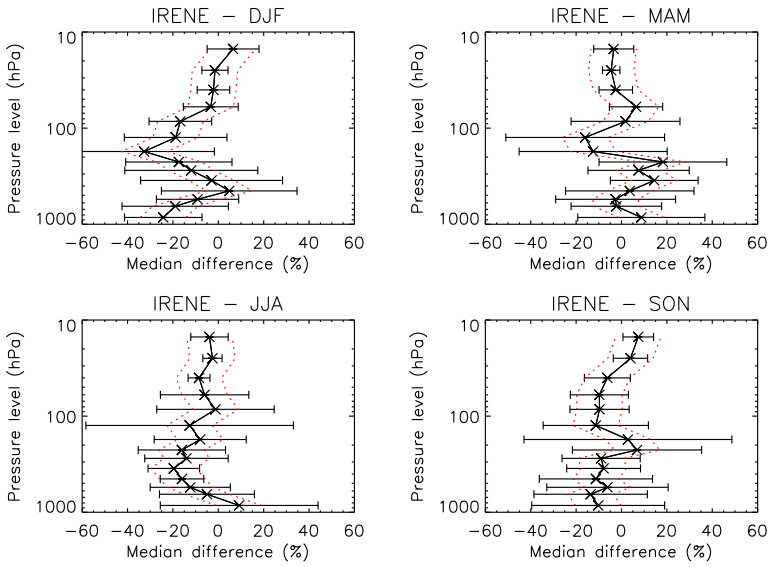

Figure 4.18: Profile of relative bias and error standard deviation for Irene (South Africa), during the four seasons.

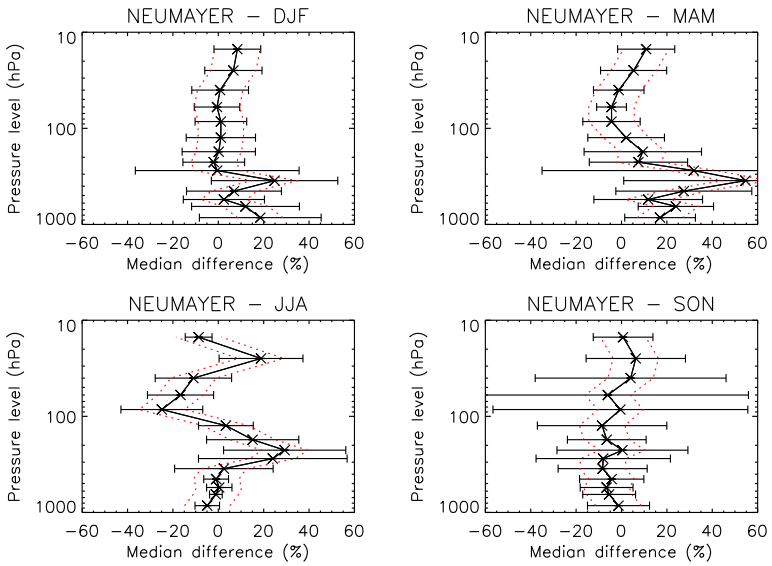

Figure 4.19: Profile of relative bias and error standard deviation for Neumayer (Antarctica), during the four seasons.

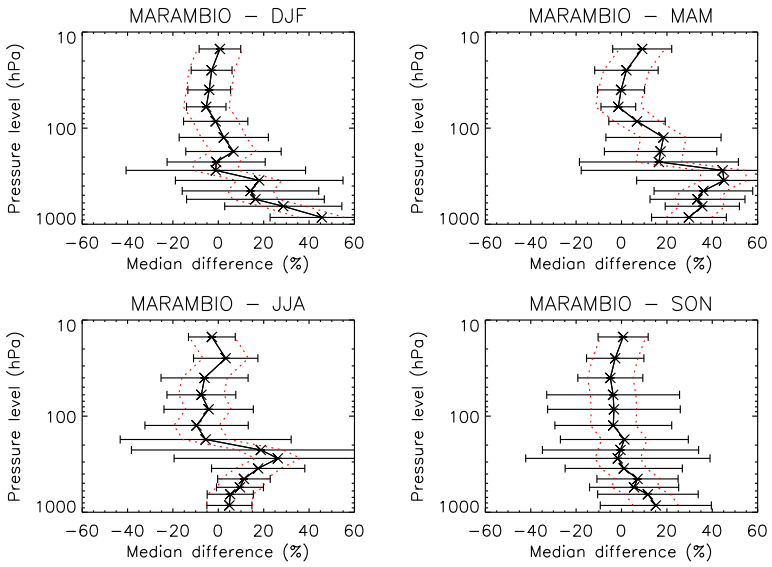

Figure 4.20: Profile of relative bias and error standard deviation for Marambio (Antarctica), during the four seasons.

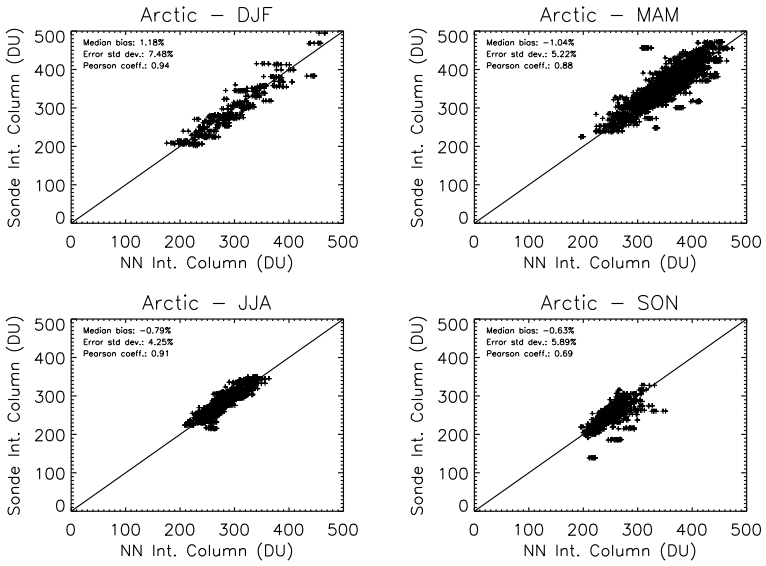

Figure 4.21: Scatter plots of retrieved versus ozonesonde columns from surface to 10 hPa for Arctic ozonesondes, during the four seasons.

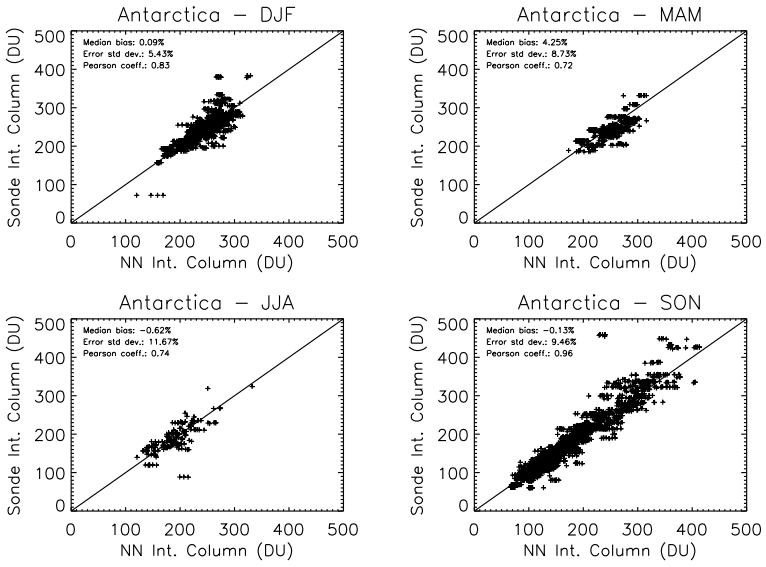

Figure 4.22: Scatter plots of retrieved versus ozonesonde columns from surface to 10 hPa for Antarctic ozonesondes, during the four seasons.

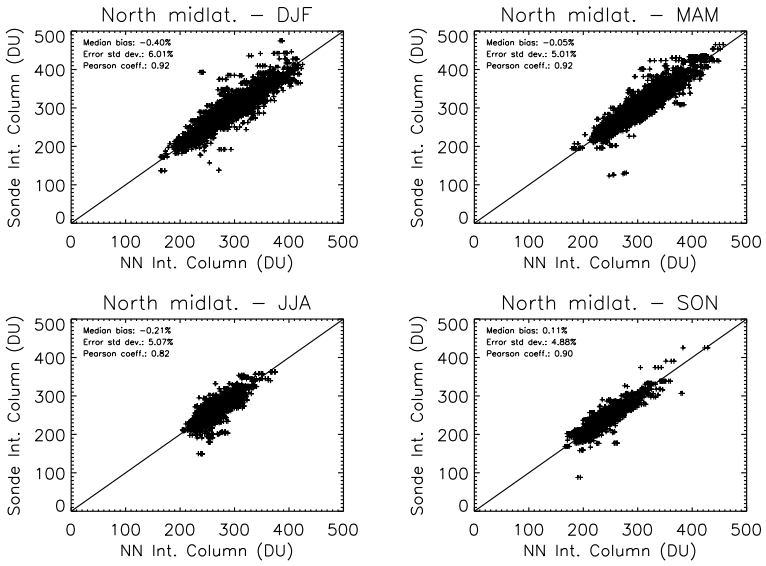

Figure 4.23: Scatter plots of retrieved versus ozonesonde columns from surface to 10 hPa for northern midlatitudes, during the four seasons.

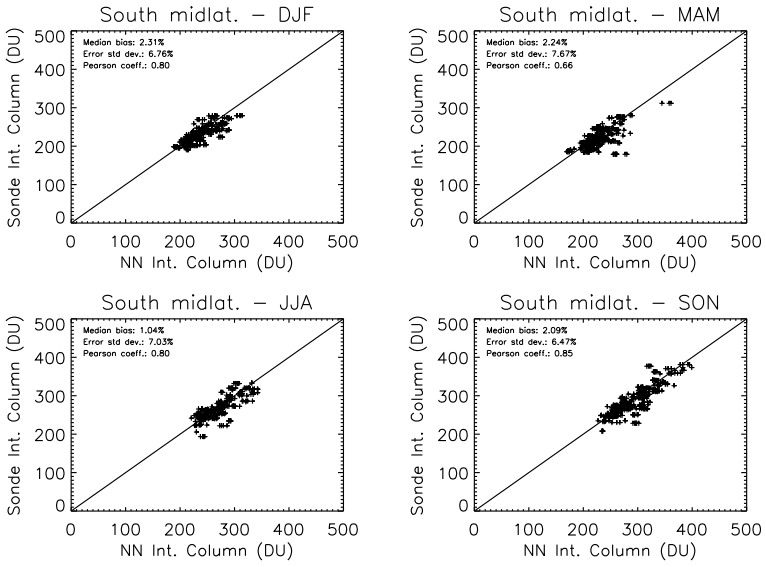

Figure 4.24: Scatter plots of retrieved versus ozonesonde columns from surface to 10 hPa for southern midlatitudes, during the four seasons.

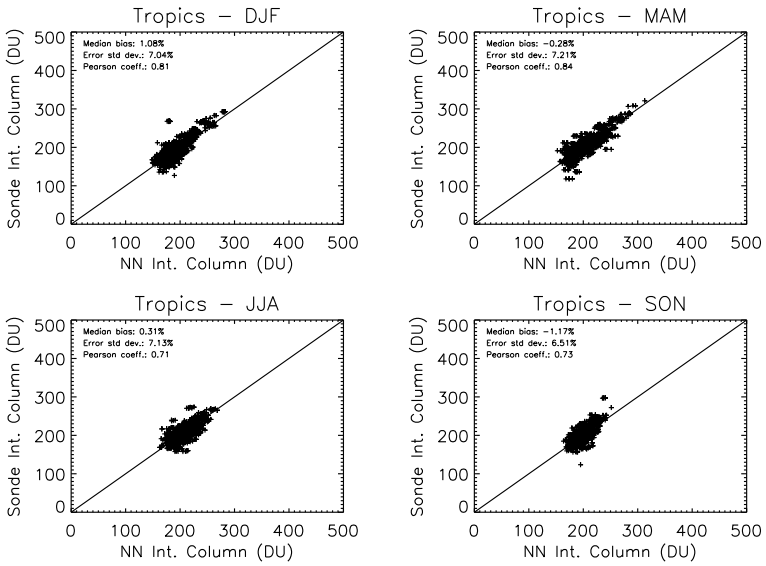

Figure 4.25: Scatter plots of retrieved versus ozonesonde columns from surface to 10 hPa for tropical ozonesondes, during the four seasons.

band and season. Since the two quantities are physically different – in that our columns only reach the 10 hPa level, whereas OMTO3 columns cover the whole atmosphere – only the Pearson correlation coefficient has been used as a measure of similarity between the two columns, and no differences have been computed. It can be noticed that in most cases the correlations between NN and OMTO3 columns are better than those between NN and sonde columns (see Tab. 4.2 for a complete comparison). This is particularly evident over Tropics and southern midlatitudes, over Arctic during SON and over Antarctica during JJA. The reason for this behaviour – that seems systematic – is probably a combination of three factors: (*i*) while the co-location criteria described in Section 4.2 are such that an ozone sounding may be co-located with multiple pixels (thereby giving rise to a certain degree of co-location mismatch), NN and OMTO3 columns are associated to the same pixels, i.e. they sample the same atmospheric portion; (*ii*) even though we do not have formal AKs for the NN algorithm, it might be reasonable to think that the NN and the OMTO3 algorithm "look through the atmosphere" in similar ways (i.e., they inherently have similar smoothing characteristics), which makes NN and OMTO3 columns more directly comparable than NN and sonde columns; (*iii*) although care has been taken

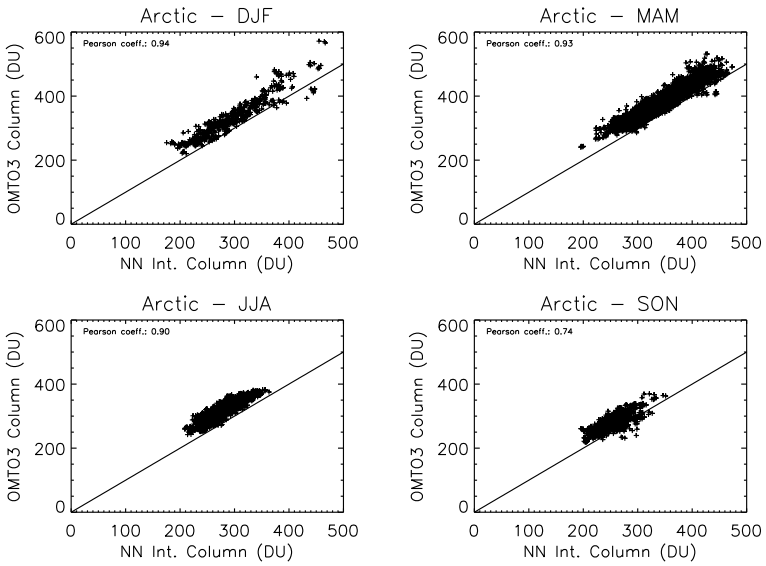

Figure 4.26: Scatter plots of retrieved surface to 10 hPa ozone columns versus OMTO3 total ozone columns over Arctic, during the four seasons.

in order to discard poor quality ozonesonde profiles, it is still possible that some bad profiles have not been detected, so that they are included in the comparison statistics. The third factor, however, should have a very limited impact.

Figures 4.31, 4.32 and 4.33 show global maps of the integrated ozone column from surface to 10 hPa (TOC_{10}) retrieved by the NN and OMTO3 total ozone columns (TOC) on 26 August and 25 October 2006, and 27 October 2010. It can be seen that on all the three dates the spatial patterns of the ozone columns look fairly consistent. A pixel by pixel comparison has shown a correlation coefficient of about 0.97 for all the dates. On 26 August 2006 (Fig. 4.31), the most relevant differences seem to be encountered over the northeastern Greenland and the eastern Siberian sea, where the NN seems to see some "hot spots" in TOC_{10}, and between the Equator and the Tropic of Capricorn, where the spatial pattern of TOC_{10} is slightly more irregular than the TOC pattern. Interestingly, in the OMTO3 map there seem to be some strange periodic features over Siberia, that are not present in NN retrievals. On 25 October 2006 (Fig. 4.32), the spatial irregularities in tropical TOC_{10} are also present north of the Equator. Furthermore, a strong hot spot in TOC_{10} is observed in the stretch of sea between Greenland and

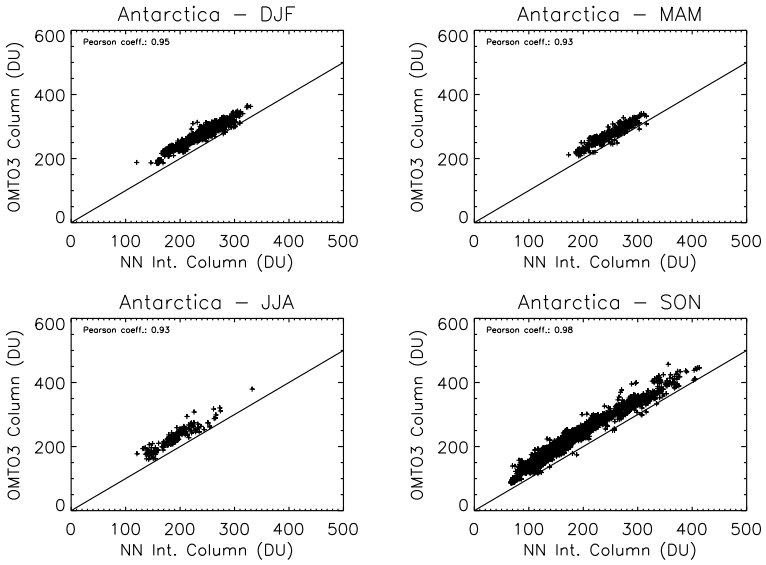

Figure 4.27: Scatter plots of retrieved surface to 10 hPa ozone columns versus OMTO3 total ozone columns over Antarctica, during the four seasons.

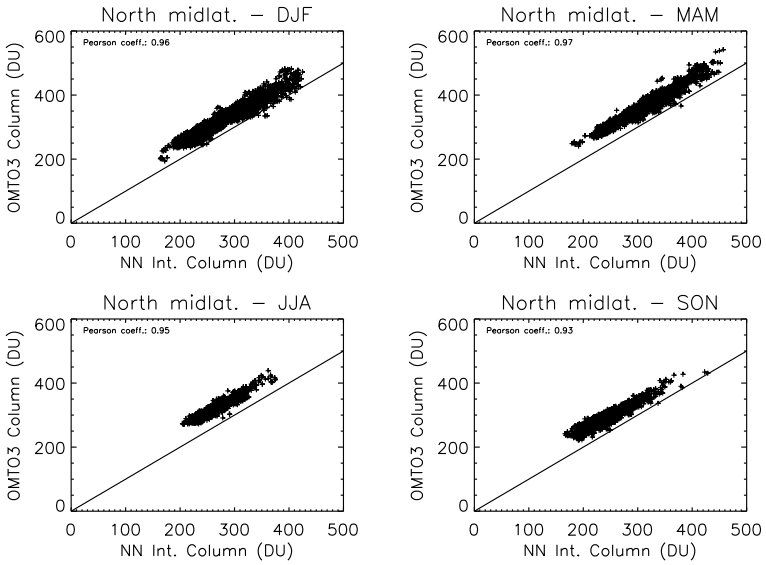

Figure 4.28: Scatter plots of retrieved surface to 10 hPa ozone columns versus OMTO3 total ozone columns over northern midlatitudes, during the four seasons.

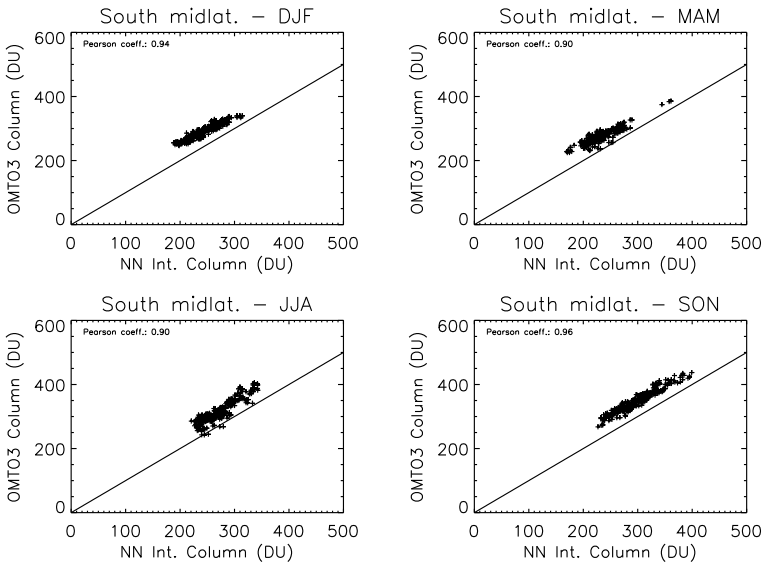

Figure 4.29: Scatter plots of retrieved surface to 10 hPa ozone columns versus OMTO3 total ozone columns over southern midlatitudes, during the four seasons.

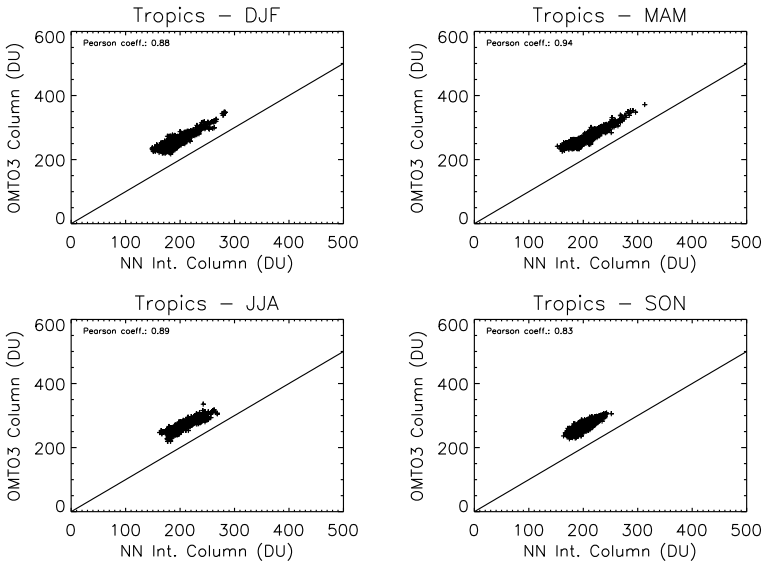

Figure 4.30: Scatter plots of retrieved surface to 10 hPa ozone columns versus OMTO3 total ozone columns over Tropics, during the four seasons.

Table 4.2: Pearson correlation coefficient between NN retrieved surface to 10 hPa ozone columns and ozonesonde columns (ρ_{sonde}), and OMTO3 columns (ρ_{omto3}).

Zone	DJF		MAM		JJA		SON	
	ρ_{sonde}	ρ_{omto3}	ρ_{sonde}	ρ_{omto3}	ρ_{sonde}	ρ_{omto3}	ρ_{sonde}	ρ_{omto3}
Arctic	0.94	0.94	0.88	0.93	0.91	0.90	0.69	0.74
Antarctica	0.83	0.95	0.72	0.93	0.74	0.93	0.96	0.98
North ML	0.92	0.96	0.92	0.97	0.82	0.95	0.90	0.93
South ML	0.80	0.94	0.66	0.90	0.80	0.90	0.85	0.96
Tropics	0.81	0.88	0.84	0.94	0.71	0.89	0.73	0.83

Norway, north of the Iceland. Such hot spot is absent from the OMTO3 TOC map, and needs to be investigated. This is the most significant dissimilarity between NN TOC_{10} and OMTO3 TOC observed so far. The map for 27 October 2010 is interesting, because this date is well outside the period covered by the NN training set. The world coverage is not global, because the row anomaly led to discard most of the pixels on the eastern part of each OMI swath. Also on this date, the most important spatial structures in the OMTO3 TOC are visible in the NN TOC_{10}. However, a more pronounced along-track striping effect is seen in the NN TOC_{10}.

A rough estimate of the algorithm performances with regard to stratospheric and tropospheric columns has been obtained by integrating ozonesonde and retrieved ozone profiles from surface to the NCEP/NCAR tropopause and from there to 10 hPa. Scatter plots of retrieved versus measured stratospheric ozone columns are shown in Figs. 4.34 to 4.38. Analogous plots for the tropospheric columns are shown in Figs. 4.39 to 4.43. As expected, stratospheric column retrievals are more accurate than tropospheric columns. While the performances for stratospheric columns look fairly uniform among all latitudes and seasons (small relative biases and error standard deviations ranging from about 4% to about 10%), the algorithm behaviour with respect to tropospheric columns seems variable with latitude and season. In particular, significant negative biases are observed over the Arctic (except, perhaps, for DJF, when the calculated bias is only about -1%), whereas the biases are most often positive in the other latitude bands (again an analogy with *Di Noia et al.*, 2013b). Exceptions are Tropics and northern midlatitudes during SON and MAM (but in MAM the biases are quite low, so that their significance is questionable).

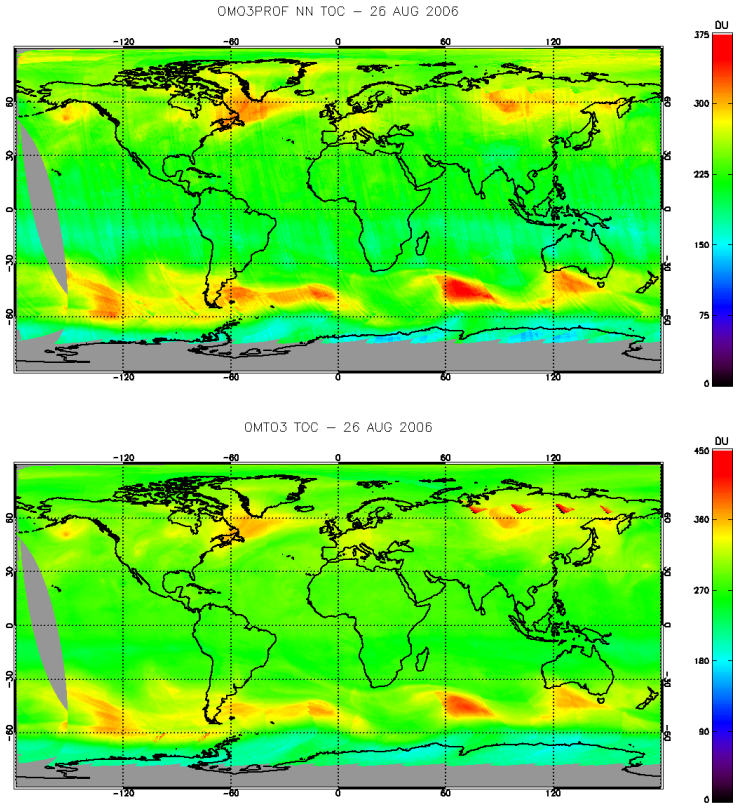

Figure 4.31: Integrated ozone columns up to 10 hPa as retrieved by the ozone profile NN (*above*) and total ozone column taken from the OMTO3 L2 product (*below*) on 26th August 2006.

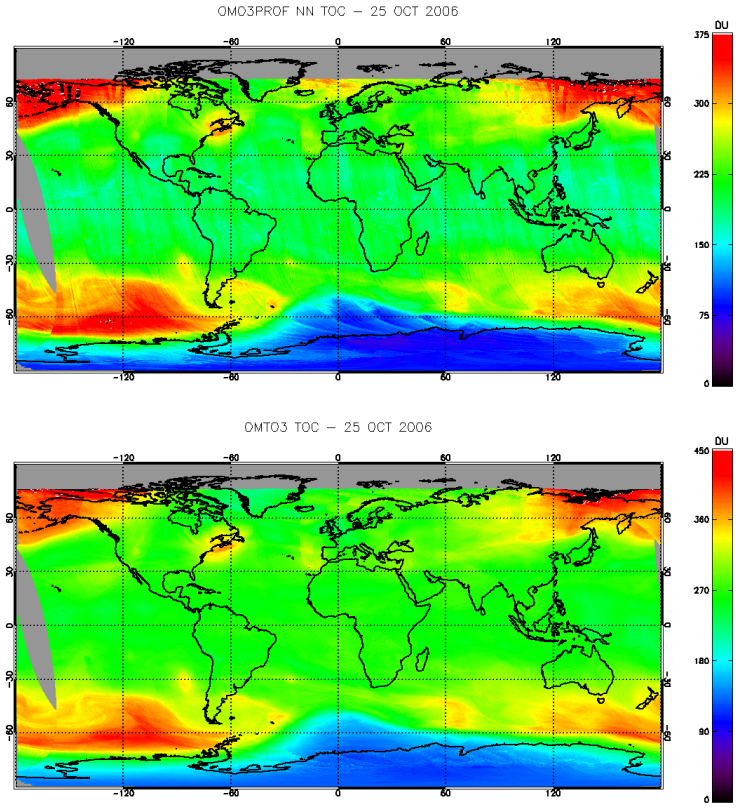

Figure 4.32: Integrated ozone columns up to 10 hPa as retrieved by the ozone profile NN (*above*) and total ozone column taken from the OMTO3 L2 product (*below*) on 25th October 2006.

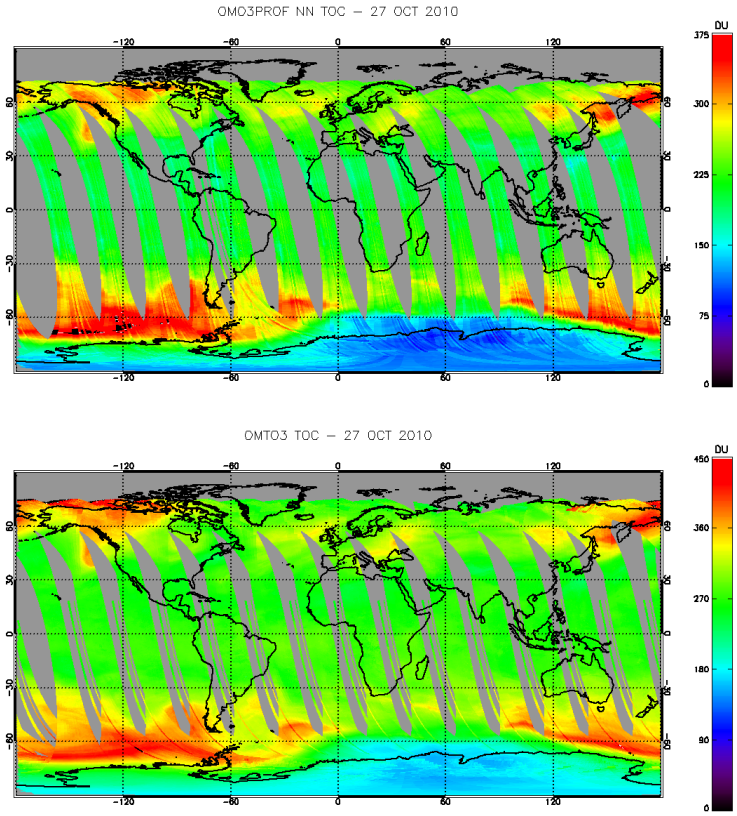

Figure 4.33: Integrated ozone columns up to 10 hPa as retrieved by the ozone profile NN (*above*) and total ozone column taken from the OMTO3 L2 product (*below*) on 27th October 2010.

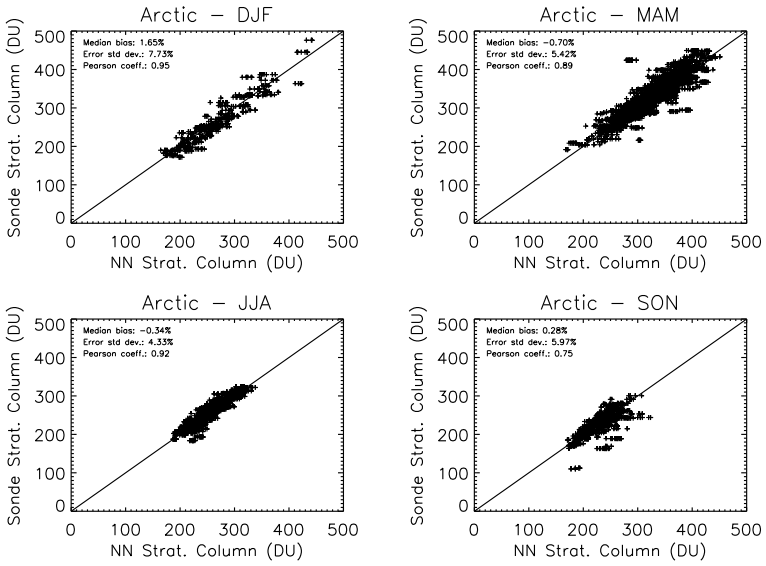

Figure 4.34: Scatter plots of retrieved versus ozonesonde columns from the tropopause to 10 hPa for Arctic ozonesondes, during the four seasons.

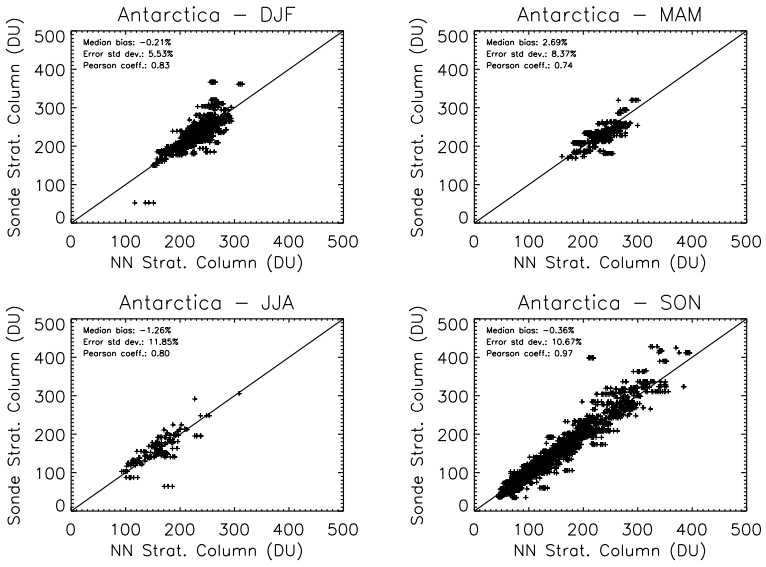

Figure 4.35: Scatter plots of retrieved versus ozonesonde columns from the tropopause to 10 hPa for Antarctic ozonesondes, during the four seasons.

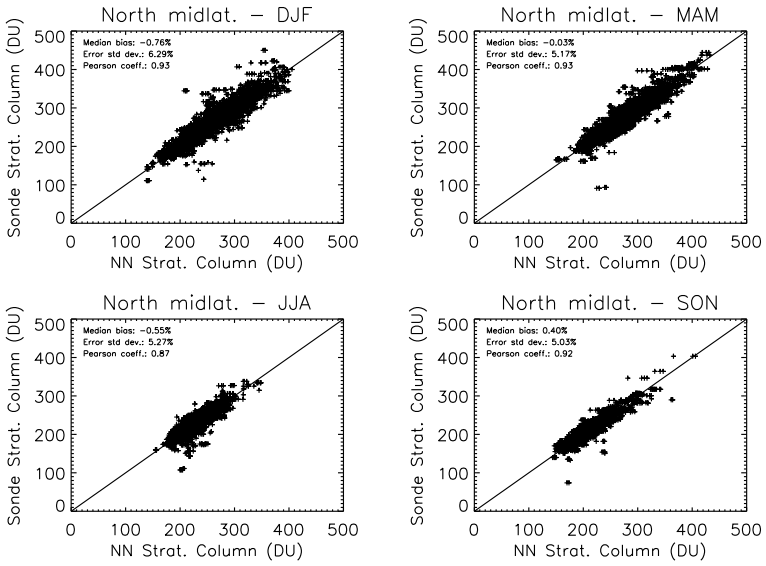

Figure 4.36: Scatter plots of retrieved versus ozonesonde columns from the tropopause to 10 hPa for northern midlatitudes, during the four seasons.

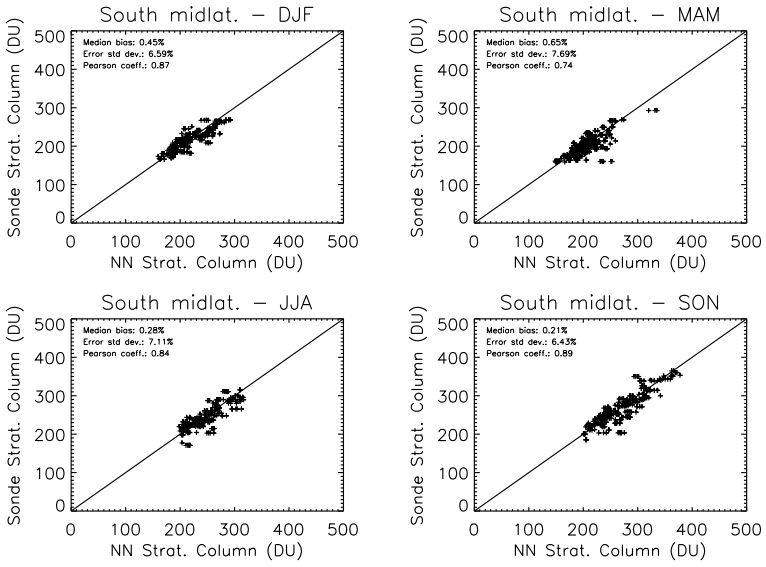

Figure 4.37: Scatter plots of retrieved versus ozonesonde columns from the tropopause to 10 hPa for southern midlatitudes, during the four seasons.

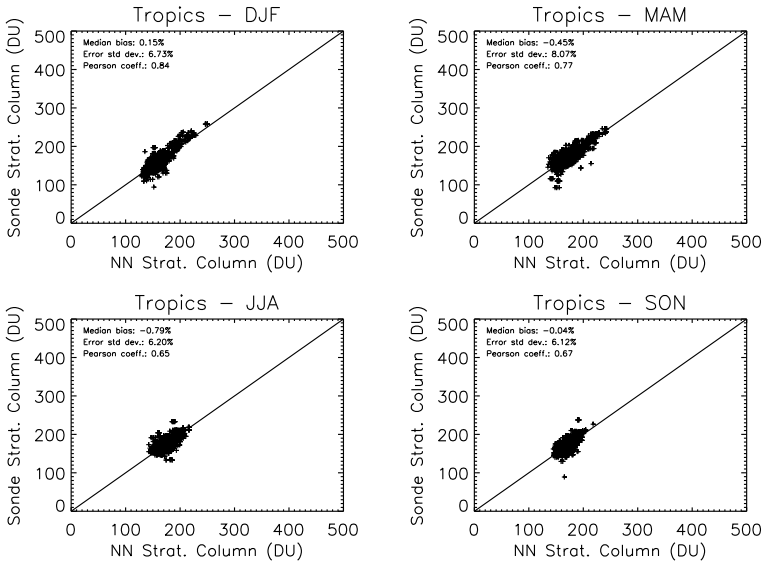

Figure 4.38: Scatter plots of retrieved versus ozonesonde columns from the tropopause to 10 hPa for tropical ozonesondes, during the four seasons.

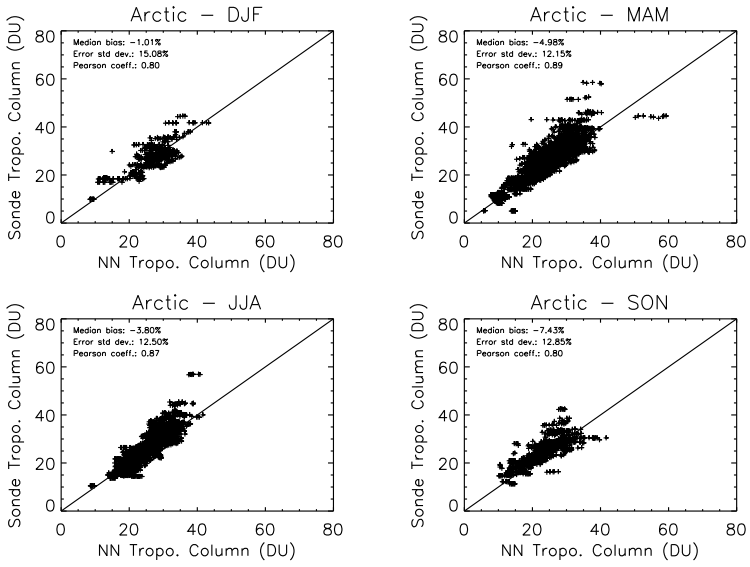

Figure 4.39: Scatter plots of retrieved versus ozonesonde columns from surface to the tropopause for Arctic ozonesondes, during the four seasons.

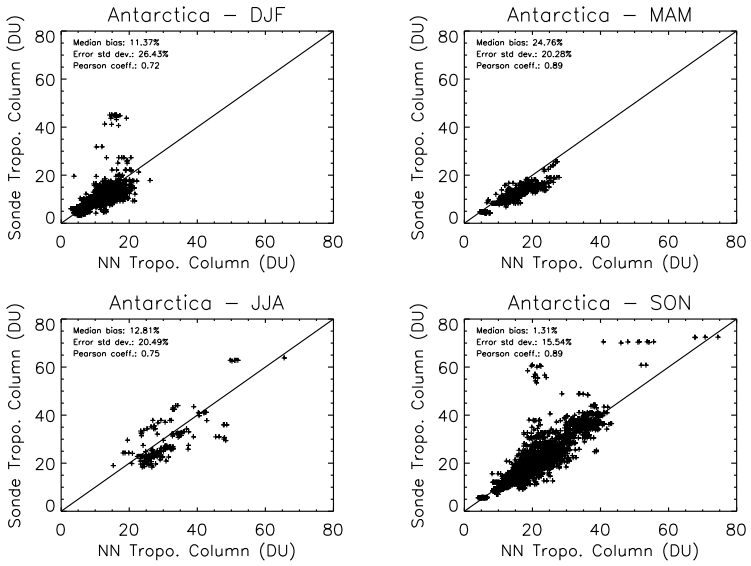

Figure 4.40: Scatter plots of retrieved versus ozonesonde columns from surface to the tropopause for Antarctic ozonesondes, during the four seasons.

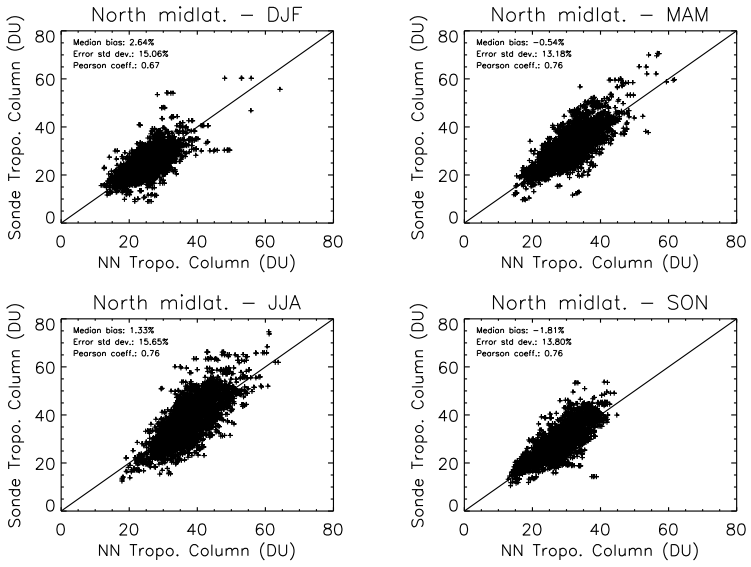

Figure 4.41: Scatter plots of retrieved versus ozonesonde columns from surface to the tropopause for northern midlatitudes, during the four seasons.

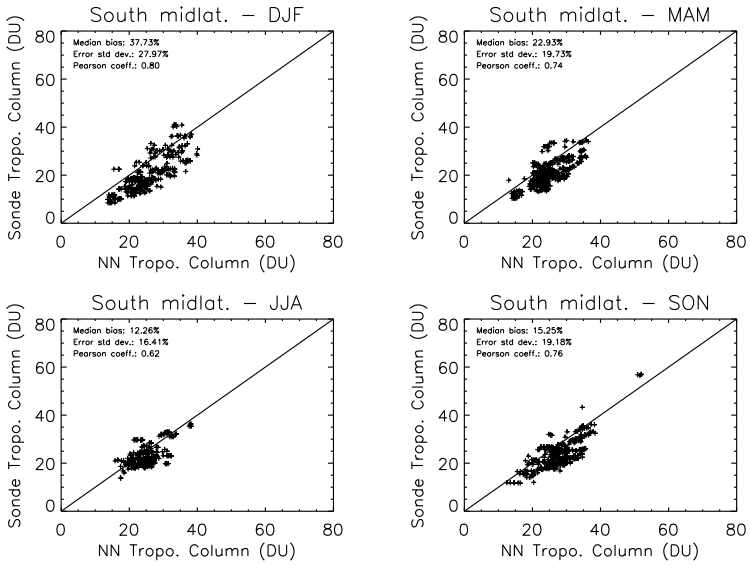

Figure 4.42: Scatter plots of retrieved versus ozonesonde columns from surface to the tropopause for southern midlatitudes, during the four seasons.

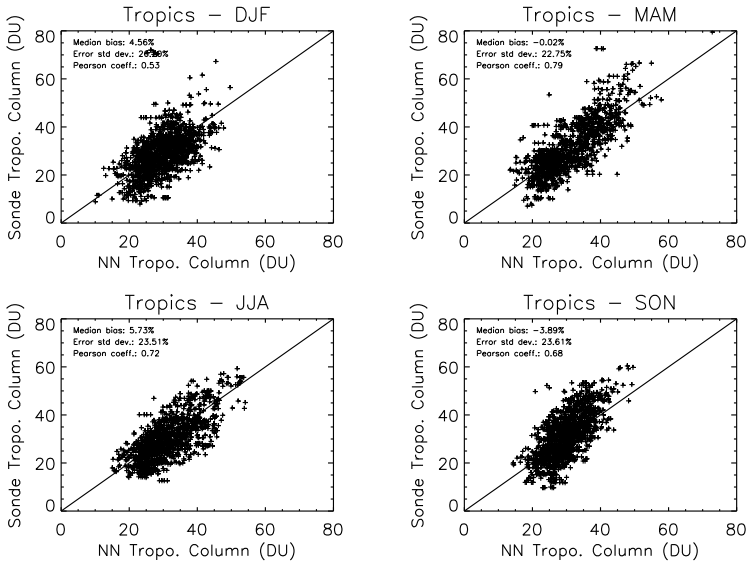

Figure 4.43: Scatter plots of retrieved versus ozonesonde columns from surface to the tropopause for tropical ozonesondes, during the four seasons.

4.4 Outline

In this chapter, a NN approach to ozone profile retrievals from OMI has been proposed. As a proof of concept, a NN was trained with OMI UV reflectance spectra, observation angles, cloud fraction, cloud top height, and NCEP/NCAR temperature profiles as input variables; and with ozone profiles measured by ozonesondes as output quantities, without making any assumptions on the upper atmospheric ozone profile. As a result, the NN does not retrieve the full ozone profile, but retrieves the profile between the surface and 10 hPa. Partial ozone columns in 14 atmospheric layers are the outputs of the algorithm.

The algorithm has been validated against ozonesonde data that have not been used during the training. Separate statistics have been computed for five latitude bands and four seasons. Not surprisingly, the best performances are generally attained in the stratosphere, where the observed accuracies are in most cases around 10%, especially far from the tropopause. More problems are found in the UTLS and in the troposphere, especially over the Tropics. In most cases, small biases are observed in the stratosphere, whereas larger biases are occasionally found in the troposphere, especially over the Tropics during JJA and SON, and over southern midlatitudes during all the season except JJA. The smallest tropospheric biases are found over northern midlatitudes. Moderate negative biases have been observed in the Arctic troposphere, consistently with previous work on tropospheric ozone.

The integrated ozone columns from surface to 10 hPa show a good agreement with ozonesondes, and an even better agreement (expressed in terms of the Pearson correlation coefficient) with OMTO3 total ozone columns. The most plausible explanation for this is that, while each ozone sounding may be co-located with multiple pixels due to the chosen co-location criteria, each pixel of the NN ozone profile algorithm is co-located with only one OMTO3 pixels, making the sampled atmospheric portion more directly comparable. The quality of the tropospheric columns is partially satisfactory, but generally worse than the quality of the retrievals obtained with the dedicated tropospheric ozone NN (*Di Noia et al.*, 2013b), probably because no tropopause information is used as an input in the ozone profile NN, and possibly also because the co-location criteria for the ozone profile NN are looser than those for the OMITROPO3-NN. Furthermore, since no cloud screening has been performed in the dataset for the ozone profile NN, it is possible that this has an impact on the retrieved tropospheric columns.

While the use of a dataset purely consisting of ozonesonde data to train

the NN might be acceptable for a prototype ozone profile product, different choices should be considered if an operational NN is to be developed, because ozonesonde data do not cover the entire vertical range of the atmosphere. Other ozone profile products based on NNs have solved this problem by either matching ozonesonde data with limb ozone profile retrievals (*Müller et al.*, 2003) or using other nadir ozone profiles as target values for the NN (*Del Frate et al.*, 2002, 2005a). However, both these methods have pitfalls. In particular, the limb-ozonesonde matching can suffer from biases between limb and sonde profiles that have to be adjusted in some way. On the other hand, the use of another nadir ozone profile product retrieved with the same instrument creates a sort of "feedback loop" in the NN, and in any case makes it so that the NN retrieved profiles will not be better than those retrieved by the algorithm used as a reference. In view of this, a viable alternative could consist in using simulated data. A possible approach could consist in selecting ozone profiles from a reanalysis product – such as the European Center for Medium-range Weather Forecast (ECMWF) ERA-Interim ozone mass mixing ratios, given at 37 pressure levels from 1000 to 1 hPa (*Dragani*, 2011) – and using such profiles as an input for RTM simulations that also account for the instrument noise features. This approach seems attractive for at least four reasons. First, it leads to a full ozone profile product, overcoming the shortcoming of ozonesonde data covering only a portion of the atmosphere. Second, it avoids the problems that would be associated with the matching between ozonesonde and limb profiles. Third, the availability of a temporally extended (from 1979 to 2012) global dataset would make it possible to create a large and comprehensive training set for a NN. Fourth, the quality of the reanalysis data would not be a severe limiting factor, because such data would not be used as target data to be co-located with real reflectance measurements, but only as inputs for RTM calculations, that would automatically produce consistent matching between ozone profiles and reflectances.

Chapter 5

Conclusions

5.1 Summary of the work

In this dissertation, neural networks (NNs) have been applied to the problem of tropospheric ozone and ozone profile retrievals from OMI ultraviolet reflectance spectra.

The first initial part of the work has concerned the validation of the OMI-TOC NN algorithm, developed by *Sellitto et al.* (2011), whose aim was the estimation of the tropospheric ozone column at northern midlatitudes. The results of this validation activity, discussed in Chapter 2, have pointed out that the OMI-TOC NN suffers from two main problems:

(i) It assumes 200 hPa as a static demarcation line between the troposphere and the stratosphere. This assumption is often incorrect at northern midlatitudes, where the complex dynamics of weather systems makes the tropopause height highly variable.

(ii) The OMI-TOC NN suffers from a considerable bias when the tropopause pressure is larger than about 250 hPa. Such values of the tropopause pressure, normally associated to low pressure systems, are not rare at northern midlatitudes, especially on the northeastern Atlantic Ocean.

These problems have led to the design of a new NN for tropospheric ozone retrieval, named OMITROPO3 NN, presented in Chapter 3. This new NN is able to overcome the aforementioned problems thanks to the use of the NCEP/NCAR tropopause pressure as the top of the troposphere. Furthermore, the training set for the new NN algorithm has been extended so as to cover all the latitude bands, and ancillary data (tropopause pressure, temperature profile, first guess tropospheric ozone column from a satellite

climatology) have been introduced into the input vector of the NN, in order to make the tropospheric ozone estimates as accurate as possible. A validation against ozonesonde data, and a number of comparisons with Chemistry/Transport Model (CTM) simulation have shown satisfactory results. In particular, the OMITROPO3 NN seems to be able to estimate the tropospheric ozone column with root mean square errors between 5 and 6 DU over all the latitude bands.

The NN technique has been then applied to the retrieval of the ozone profile from OMI data. Also this NN, designed and trained in a similar way to the OMITROPO3 NN, has been validated against a large number of ozonesonde data, showing promising results. The design and the validation of this algorithm are discussed in Chapter 4. The goal of this work was to demonstrate the effectiveness of the NN technique in the design of an ozone profile product that overcomes the computational limitation of the operational ozone profile product, thereby allowing a full exploitation of the spatial resolution of the OMI instrument.

5.2 Future work: error characterization

The most serious gap of NN retrieval algorithms with respect to more established methods like OE and regularization is their difficulty in providing a predictive error characterization, i.e. to provide an estimate of the error covariance matrix associated with each retrieved profile and to quantify the vertical resolution of the measurements through averaging kernels (AKs). Such quantities are extremely important when the retrieved ozone profiles have to be used in a data assimilation system, and when such profiles have to be compared with profiles retrieved by other satellite instruments (*Rodgers and Connor*, 2003). In this section we will try to review the possible methods to incorporate similar information in NN retrievals, discussing advantages and limitations of each method.

An important feature of NN models – that can be useful in error characterization – is the fact that the Jacobian matrix of a NN model can be computed analytically. In fact, a NN input-output function is a nested superposition of C^{∞} functions, i.e. functions that are continuously differentiable infinite times. When a NN is used as a retrieval model, this means that the gain matrix $\mathbf{G}$ of the retrieval algorithm can be directly computed for any given input vector. This fact is important for the estimation of covariance matrices as well as for the estimation of the averaging kernels. In the next two subsections we will discuss these two issues separately.

5.2.1 NNs and averaging kernels

In a work concerning operational trace gas retrievals from the Infrared Atmospheric Sounding Interferometer (IASI), *Turquety et al.* (2004) proposed to combine gain matrices computed in this way with weighting functions computed by using a radiative transfer model (RTM). In their work, they computed the weighting functions by using a simple perturbation approach, but this may be avoided if RTMs providing analytical weighting functions are used. While this seems a reasonable approach, it must be kept in mind that it requires many radiative transfer calculations, especially if the perturbation method is to be used. If each retrieved profile in an orbit has to be accompanied by its averaging kernel, the generation of a L2 product with this approach would become very time consuming, thereby canceling the main advantage associated with the use of NNs in profile retrievals. This issue is known to have prevented this method from being used in operational assimilations of IASI ozone data (*Massart et al.*, 2009).

One way to overcome the limitation associated with the need for radiative transfer calculations in order to estimate the weighting functions could consist in approximating also the forward model with another NN. In principle, the approximation of a forward model via NNs has an even more solid theoretical foundation than the use of NNs in retrieval models, because the forward problem is well posed, i.e., once the state of the atmosphere and surface and the observation conditions are assigned, the solution of the radiative transfer equation (RTE) is unique. Since NNs can approximate any continuous function to an arbitrary accuracy (*Hornik et al.*, 1989), solving the RTE using NNs is, in principle, feasible. Fast RTMs based on NNs have been demonstrated by several authors, even though their purposes were different from the estimation of retrieval AKs (and such thing has an impact, as we are going to discuss). For instance, *Chevallier et al.* (1998) developed a NN to compute spectrally integrated IR upward and downward radiative fluxes from temperature, water vapour, ozone and cloud effective emissivity profiles, as well as CO_2 columns and surface emissivities. They compared the cooling rates computed from these simulated fluxes and those computed using two different RTMs, and found error standard deviations of about 0.03 K/day and biases as small as 0.01 K/day, with a reduction in the computation time of a factor 22 with respect to a wide band RTM and 10^6 with respect to a line-by-line RTM. *Schwander et al.* (2001) developed a NN to map UV/VIS transmittances at seven wavelengths – simulated with a RTM – onto high spectral resolution transmittances, using the total ozone amount and the solar zenith angle as additional inputs. They found very small er-

rors between 315 and 700 nm, but from their paper it is not completely clear how they derive full spectral information from such a limited number of input quantities. *Krasnopolsky and Schiller* (2003) proposed the use of a fast forward model based on NN in order to check for the physical consistency of NN retrieved atmospheric parameters from the Special Sensor Microwave Imager (SSM/I).

While NNs can guarantee good performances in simulating radiances from atmospheric parameters, the reproduction of weighting functions is a more difficult task. Although, in theory, NNs are able to approximate reasonably smooth continuous functions together with all their derivatives (*Hornik et al.*, 1990), selecting a NN model with good capabilities in estimating such derivatives is challenging. If learning algorithms like the standard backpropagation or the Scaled Conjugate Gradient (SCG) are used to train the NN, then strong oscillations in the simulated weighting functions are to be expected. This would have a negative impact on the evaluation of the NN AKs. In order to mitigate these problems it is necessary to introduce some regularization in the learning algorithms to penalize NN models that exhibit such oscillations. The most elementary form of regularization is to replicate the training patterns by corrupting the input vectors with several realizations of a white noise process and mapping such vectors to the correct output (*Bishop*, 1995b). Another method, proposed and demonstrated by *Aires et al.* (1999) for RTM simulations in the 11 temperature channels of the TIROS Operational Vertical Sounder (TOVS), is called "weight smoothing", and consists in modifying the learning cost function by applying a constraint matrix to the NN Jacobian, in a way that pretty much resembles the Phillips-Tikhonov regularization. It should be kept in mind, however, that the differentiation of the modified cost function – necessary to compute the weight updates – would require the computation of the NN Hessian matrix (i.e., the NN second derivatives). This might add considerable computational complexity to the training algorithm. A different alternative is the NN ensemble approach, proposed by *Krasnopolsky* (2007). In this approach, several NNs are trained (with different architectures or initializations), and their results are combined together to filter out random errors (due, e.g., to noise or imperfect learning) on the NN Jacobians.

5.2.2 NNs and error covariance matrix

OE and Phillips-Tikhonov retrievals provide a measure of how trustworthy a retrieved ozone profile is, in the form of an error covariance matrix. *Rodgers* (1990) provides the most widespread framework for the evaluation of the

error sources in a profile retrieval algorithm. He distinguishes three basic error sources: (*i*) the null-space error (or smoothing error), caused by the fact that some parts of the true profile cannot be measured by the observing system, and directly related to the AKs; (*ii*) the measurement error, that is simply the radiometric noise propagated through the retrieval gain matrix; (*iii*) the model parameter errors, i.e. random (e.g. measurement uncertainty) or systematic errors (e.g. model errors, wrong assumptions) in the model parameters, that are propagated to the retrieval similarly to measurement errors. Since these errors are mutually independent, their associated covariance matrices can be summed up, to give the total error covariance matrix. In principle, estimating the covariance matrices for the last two error components is possible also for a NN, by simply propagating input and parameter uncertainties through the NN retrieval Jacobians. The assessment of null-space errors, that are related to the AKs, is more problematic, because of the problems in estimating AKs for a NN, that have been discussed in the previous subsection.

Aires et al. (2004a) propose an alternative error decomposition, more suitable for NN algorithms. Specifically, they suggest that the retrieval error covariance can be decomposed in an inversion term, that accounts for all the errors that are related to the retrieval process (imperfections in the training set, non-optimality of the NN architecture, suboptimal learning due to convergence towards a weight vector that differs from the global minimum of the error surface) and depends on the NN Jacobian and Hessian matrices (with respect to the weights); and an "intrinsic noise" term, that accounts for all the other sources of error. *Aires et al.* (2004a) derive this decomposition starting from a Bayesian formulation of the NN training process.

Dybowski and Roberts (2009) give a comprehensive review of the methods that have been proposed to associate error estimates to the outputs of a NN. Among these methods, a remarkable one is based on the fact that – as shown by *Bishop* (1995a) – a NN trained with error cost function

$$\mathcal{E} = \frac{1}{2} \sum_{n=1}^{N} \left[\varphi(\mathbf{x}^{(n)}, \mathbf{w}) - y^{(n)} \right]^2$$

where φ is the NN input-output function and $\mathbf{w}$ is the NN weight vector, approximates the conditional mean $\mathrm{E}[y|\mathbf{x}]$. Then it follows that a NN trained using the squared residuals as target values should approximate the conditional variance $\mathrm{var}(y|\mathbf{x})$. This method has been applied to ozone profile retrievals from GOME by *Müller et al.* (2003).

Appendix A

Satellite TCO retrievals: An useful tool to quantify surface ozone pollution? An experiment using OMI observations

A.1 Introduction

One of the reason why the quantification of ozone concentration in the troposphere is an important task is that ozone is toxic for the living beings. Therefore, high ozone concentrations near the Earth's surface are hazardous (*Anenberg et al.*, 2009; *Booker et al.*, 2009). Despite the difficulty in retrieving tropospheric ozone from space, qualitative signatures of heavy ozone pollution events have been shown to be present in satellite observations already in the 1980's. In particular, *Fishman et al.* (1987) discuss the use of Total Ozone Mapping Spectrometer (TOMS) total ozone column observations to identify an extended pollution event that occurred over the United States during the August 1980. *Fishman et al.* (2003) relate the climatological features of tropospheric ozone columns retrieved through the Tropospheric Ozone Residual (TOR) technique applied to TOMS and Solar Backscattered Ultraviolet (SBUV) data to biomass burning in the Tropics and urban pollution over United States, China and India. *Kar et al.* (2010) suggest that urban scale signatures can be observed in TOR monthly means over large

metropolitan areas, by applying the TOR method to NASA Aura Ozone Monitoring Instrument (OMI) and Microwave Limb Sounder (MLS) data.

In this chapter, we address the question of whether satellite observations of tropospheric ozone can be used to monitor surface ozone pollution events on a daily basis. In order to answer this question, it is necessary to see preliminarily to what extent are surface ozone measurements representative of tropospheric ozone columns. In a recent paper, *Chatfield and Esswein* (2012) have made a first attempt to relate surface ozone to lower tropospheric columnar ozone concentrations (which they call "retrievable" columns), by analyzing the vertical covariance structure of ozonesonde data measured at a number of stations over United States and Canada. Their study is focused on the correlation between ozone mixing ratios near the surface and partial columns in the lower troposphere. They limit their analyses to this atmospheric region because it is expected that the upcoming satellite instruments, such as the Geostationary Coastal and Air Pollution Events (GeoCAPE), will provide reliable information on the lowest 3 km of the atmosphere (*Zoogman et al.*, 2011).

In this study, we try to assess the possibilities for the observation of ozone pollution events with the state-of-the-art ultraviolet (UV) satellite instruments, like OMI, that only provide one single piece of information about the total tropospheric ozone column. To this aim, we investigate how representative the Tropospheric Column Ozone (TCO) is of ozone near surface by comparing TCOs computed from ozone profiles measured at a number of ozonesonde stations over Europe to surface ozone measurements performed by the European Environmental Agency (EEA) network of air quality monitoring (AQM) stations. Then, we analyse TCO satellite retrievals performed by two different algorithms – the OMITROPO3-NN and the Trajectory enhanced TOR (TTOR, *Schoeberl et al.*, 2007) – during a number of ozone pollution events in Europe, in order to see how well the satellite retrievals follow such events.

A.2 Relationship between TCO and surface ozone

In order to investigate the relationship between TCO and surface ozone (hereafter called SO), TCOs have been computed from ozone profiles measured by a number of ozonesonde stations over europe, by integrating such profiles up to the NCEP/NCAR tropopause (*Kalnay et al.*, 1996). Then, for each ozonesonde station, the closest EEA AQM station has been selected, and the TCOs have been compared with the following surface ozone statis-

tics: i) 1 hour mean, at the time as the ozonesonde launch time; ii) 8-hour mean; iii) daily mean; iv) daily maximum. The aim of this comparison is to evaluate which one of such statistics correlates better with the TCO. The list of the ozonesonde and AQM stations used in this comparison is shown in Tab. A.1. The coordinates of each stations, as well as the great circle distance between each ozonesonde/AQM station pair, are also reported in the table.

In Fig. A.1, scatter plots of TCO versus the above mentioned surface ozone statistics are reported for Payerne (Switzerland). The Pearson regression coefficient is reported, as well as the TCO vs SO linear regression coefficients. It can be seen that the daily maximum and the 1 hour averaged SO are the statistics that correlate best with TCO. This is reasonable, because both the daily means and the 8 hour running means can be influenced by nighttime SO values, and it is well known that during the night there is a strong decoupling between the boundary layer and the free troposphere. This behaviour seems to be confirmed by the results shown in Tab. A.2, where the correlation coefficients and the regression line slopes and offsets are reported for all the stations considered in this study. For 6 out of the 8 stations, the correlation coefficients between TCO and SO are larger than 0.6, and in the case of Payerne, the correlation between TCO and daily maximum SO is as high as 0.74. The only stations that exhibit a very poor correlation are Lerwick and Valentia. These two are also the only non continental stations in our set. Both stations are located very close to the sea, and therefore it is possible that the reasons for their different behaviour lie in the different characteristics of the marine atmospheric boundary layer.

The results discussed above seem to suggests that at least a weak relationship between TCO and SO is present over continental areas. Hence, in principle, accurate TCO measurements could be useful to predict SO values, at least with limited accuracy, possibly in combination with other meteorological parameters. In all the analyzed cases, the daily maximum SO is the pollution-related quantity that correlates best with the TCO, whereas the 8 hour mean SO – which is the key parameter in order to verify the compliance between actual SO values and European laws - does not seem to be predictable through the TCO.

Since the accuracy of satellite TCO measurements is never too high, given the intrinsic difficulty of quantifying tropospheric ozone from space, the results shown above are still not enougth to answer the fundamental question of whether satellite data can be used to exploit these weak correlations in order to provide information about the SO. In the next section, we try to address this issue by comparing time series of TCO retrieved by OMI

Table A.1: Ozonesonde stations used in this study, together with the EEA AQM station selected for comparison for each ozonesonde station.

Ozonesonde station	Lat.	Lon.	AQM station (Code)	Lat.	Lon.	Distance (km)
Barajas (Madrid)	40.46	−3.65	Barajas I (ES1646A)	40.46	−3.58	5.92
De Bilt	52.10	5.18	Utrecht - Erzeijstraat (NL00639)	52.07	5.12	5.29
Legionowo	52.40	20.97	Legionowo (PL0029A)	52.41	20.96	1.30
Lerwick	60.13	−1.18	Lerwick (GB0881A)	60.14	−1.19	1.24
Payerne	46.82	6.95	Payerne (CH0002R)	46.81	6.94	1.34
Praha	50.02	14.45	Praha - Libus (CZALIB)	50.01	14.45	1.11
Uccle	50.80	4.35	Uccle (BETR012)	50.80	4.36	0.70
Valentia Obs.	51.93	−10.25	Valentia (IE0001R)	51.93	−10.23	1.37

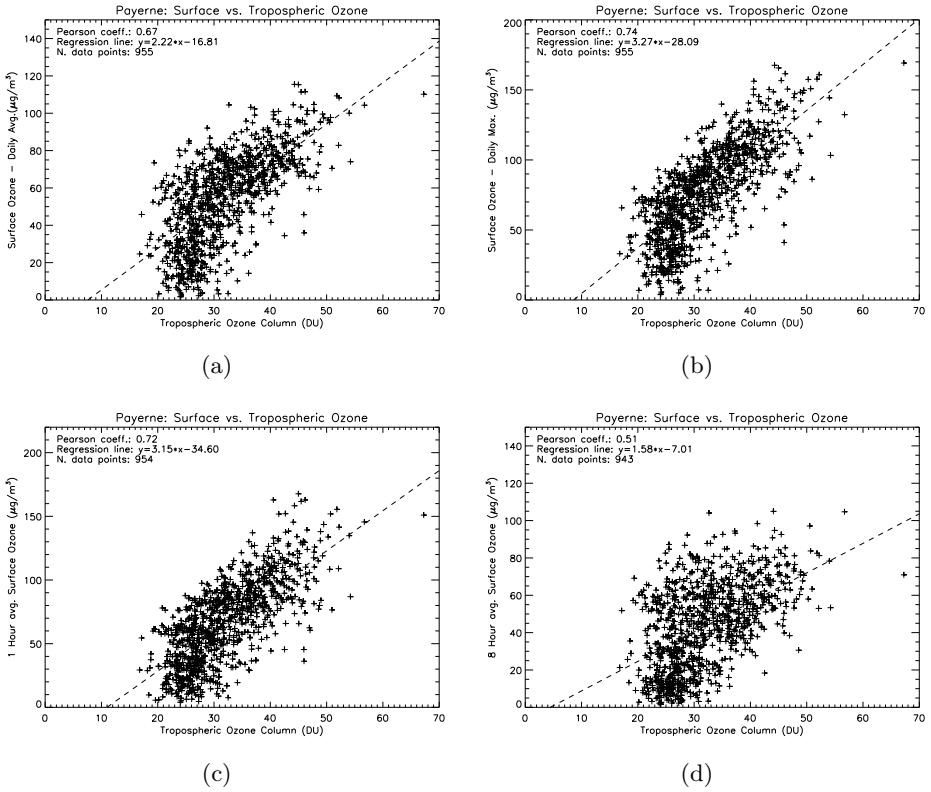

Figure A.1: Scatter plots of: (a) daily averaged, (b) daily maximum, (c) 1 hour averaged and (d) 8 hour averaged surface ozone, versus TCO, at Payerne (Switzerland).

Table A.2: Correlation coefficient (r), and regression line slope (α) and offset (β) between TCO and surface ozone for all the locations considered in this study.

Location	1 hour			8 hour			Daily			Daily max.			N. data
	r	α	β	r	α	β	r	α	β	r	α	β	
Barajas	0.62	1.93	−18.82	0.54	1.02	−8.14	0.60	1.37	−12.19	0.64	2.10	−19.64	247
De Bilt	0.55	1.91	−33.28	0.38	0.84	−9.34	0.57	1.61	−27.21	0.63	2.56	−43.15	279
Legionowo	0.65	2.79	−23.79	0.50	1.81	−1.59	0.59	2.03	−5.59	0.65	2.69	−8.24	129
Lerwick	0.27	0.86	36.01	0.26	0.80	36.04	0.32	0.93	33.70	0.33	0.96	40.41	109
Payerne	0.72	3.15	−34.60	0.51	1.58	−7.01	0.67	2.22	−16.81	0.74	3.27	−28.09	955
Praha	0.65	3.21	−38.78	0.43	1.45	−3.38	0.56	1.95	−13.72	0.68	3.10	−31.67	317
Uccle	0.62	2.53	−30.70	0.50	1.31	−8.53	0.60	1.77	−17.75	0.65	2.82	−33.14	473
Valentia	0.38	1.04	34.81	0.19	0.53	48.01	0.26	0.68	45.37	0.37	0.96	44.52	180

to time series of SO measured by AQM stations during an event of heavy ozone pollution that occurred over Europe in 2007.

A.3 Methodology

In this section, we will discuss the analysis of the time evolution of the SO measured by AQM stations and the TCO retrieved by OMI during a high ozone episode over Europe. We select a number of study areas over Europe, based on the following criteria: i) the areas must have been affected by the ozone episode; ii) the areas must be intensively sampled by the EEA AQM stations network. For each area we study the evolution of the daily maximum SO and of the TCO, both averaged over that area. The averaging has the aim of reducing the impact of random errors on TCO retrievals, because these errors can make it impossible to exploit the weak correlation between TCO and SO. In order to ensure that an adequate number of pixels are averaged, only the days where at least the 20% of the pixels included in the region of interest are not cloudy are considered in this analysis. Furthermore, we extend our observation period to a number of days before and after each pollution event, in order to see whether the signals of SO increases and decreases are visible in the satellite time series.

A.4 July 2007 ozone episode

According to the EEA statistics, the heaviest ozone episode in 2007 occurred between July 14 and 21 (*EEA*, 2008). During this period, extremely high SO values were observed in Northern Italy, Germany and Eastern Europe, during an intense heat wave that created favourable meteorological conditions for ozone formation near the surface. Satellite tropospheric ozone retrievals during this period have been analysed by *Eremenko et al.* (2008), who showed how signals of high ozone concentrations in the lowest 6 km of the atmosphere can be seen in retrievals performed by the Infrared Atmospheric Sounding Interferometer (IASI). However, IASI relies on a measurement principle that is completely different from that of OMI, and that is known to be more sensitive to the lowest atmospheric layers when the surface is warm, as occurs during heat waves. Therefore, we cannot expect the same level of agreement in OMI observations.

The areas we selected for our analysis during this period are Germany, the Iberian Peninsula and the Po Valley. The period selected for our analysis starts on July 12 and ends on July 31. In this way, we include the main ozone

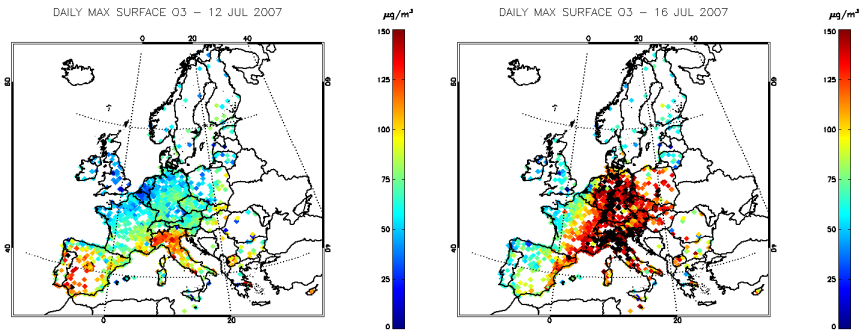

(a)

(b)

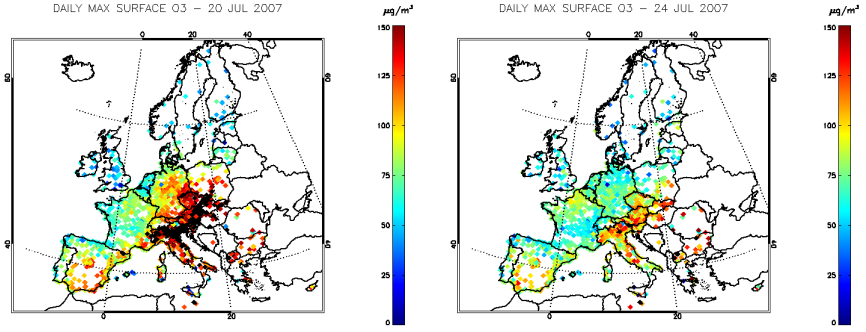

(c)

(d)

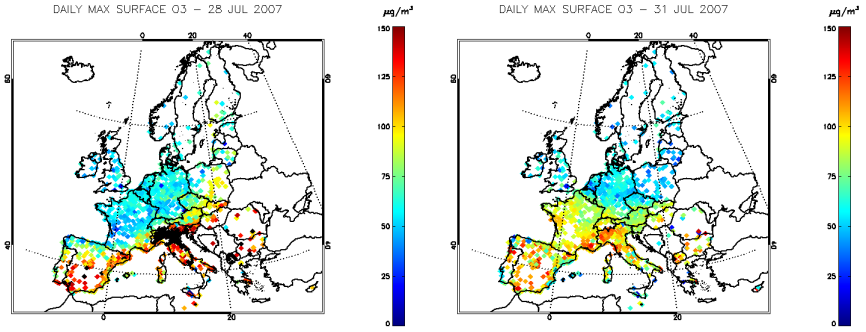

(e)

(f)

Figure A.2: Daily maximum surface ozone measured by the EEA AQM stations over Europe on 12, 16, 20, 24, 28 and 31 July 2007.

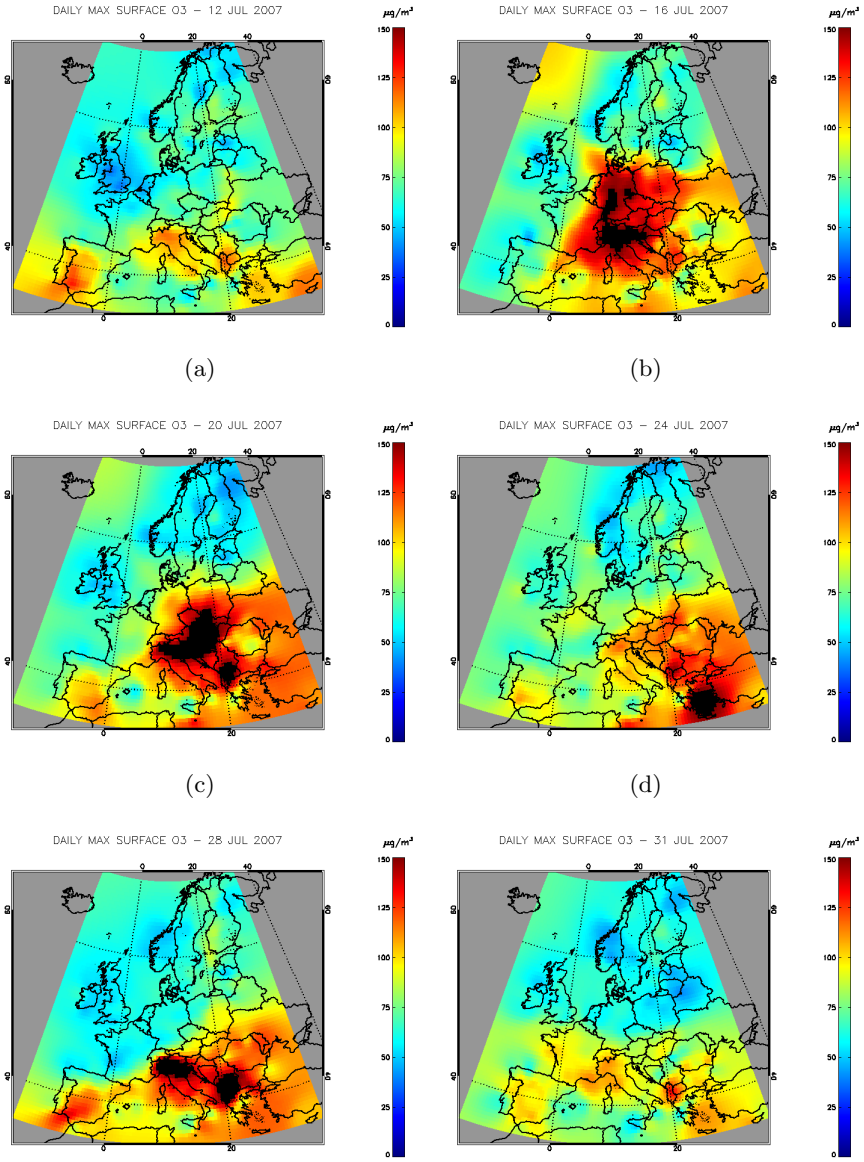

(a) (b) (c) (d) (e) (f)

Figure A.3: Daily maximum surface ozone measured by the EEA AQM stations over Europe on 12, 16, 20, 24, 28 and 31 July 2007, gridded through an Inverse Distance Weighting with exponent set to 5.

episode, together with minor episodes that occurred after July 21, and we also include two days (the first and the last one) when ozone concentrations are not high. In Fig. A.2 the daily maximum SO values measured by the AQM stations in 6 days during the selected period (see caption for details) are mapped on the European continent. In Fig. A.3, the same data are regridded using an Inverse Distance Weighting (IDW) technique, with exponent set to 5, in order to make the SO spatial patterns easier to interpret. However, it is worth to point out that these gridded maps can be considered as reliable only where the sampling is dense enough, i.e. over central and western Europe, but are not completely trustworthy over Scandinavia and eastern Europe, where the sampling is too sparse to yield a reliable interpolation. The black points/areas in the two figures represents the areas where SO concentrations are extremely high (more than 150 $\mu g/m^3$). Figures A.4 and A.5 show tropospheric ozone maps obtained by applying the OMITROPO3-NN and TTOR algorithm to OMI observations during the same dates. While remarkable difference exists between the maps produced by the two algorithms – essentially due to the inherent differences between the two methods – a visual inspection already allows to see that both the algorithms seem to reproduce the ozone enhancement that occurred over germany on July 16.

From Fig. A.6(a), it can be seen that the SO temporal behaviour over Germany is reflected reasonably well by the time behaviour of the average tropospheric ozone column retrieved by both the satellite algorithms, although some oscillations are present in the TTOR time series. In particular, the large increase in SO that occurred on the 16th of July is visible in both the algorithms. The secondary SO peak of July 26 causes a corresponding peak in the OMITROPO3-NN time series but not in the TTOR. Furthermore, it is interesting to note that both the satellite algorithms see another peak in the tropospheric ozone column on July 22, although with different magnitudes. Such peak does not seem to be attributable to variations in SO. In general, the OMITROPO3-NN time series achieves a degree of correlation as high as 0.74 with the SO time series, while the correlation coefficient for the TTOR time series drops to 0.35 because of the oscillations between July 17 and 21 (Tab. A.3).

While some pollution representativity can be observed in average TCOs and TORs retrieved over Germany, the same does not seem to hold for Iberian Peninsula and Po Valley. It must be said, however, that the SO standard deviation over the Iberian Peninsula is quite small as compared to Germany, and that makes it more difficult to follow the temporal evolution of the SO in a precise manner. For the Po Valley, instead, the cause of the

Table A.3: Correlation coefficient (r), and regression line slope (α) and offset (β) between retrieved tropospheric ozone columns and daily maximum surface ozone, averaged over Germany, Iberian Peninsula and Po Valley between 12th and 31th July 2007.

	OMITROPO3-NN			TTOR		
	r	α	β	r	α	β
Germany	0.74	6.20	−150.73	0.35	1.31	57.11
Iberian Peninsula	0.39	0.95	37.45	−0.21	−0.77	114.48
Po Valley	0.41	2.13	42.37	0.16	0.60	119.14

limited prediction skill of satellite retrievals may be related to a "saturation", due to the fact that the Po Valley remains highly polluted throughout the entire observation period (spatially averaged SO constantly above 100 $\mu g/m^3$).

Figure A.6 shows the time series of the spatially averaged SO, OMITROPO3-NN TCO and TTOR over Germany, Iberian Peninsula and Po Valley, from 12th to 31st July 2007. Table A.3 summarizes the correlation coefficient and the parameters of the spatially averaged daily maximum SO versus TCO and TOR regression line for the three regions.

Acknowledgements

The European AQM data are part of the European Environmental Agency (EEA) air quality database (AirBase), and have been downloaded from www.eea.europa.eu/data-and-maps/data. The TTOR data are publicly available at the FTP website ftp://hyperion.gsfc.nasa.gov/pub/aura/tropo3.

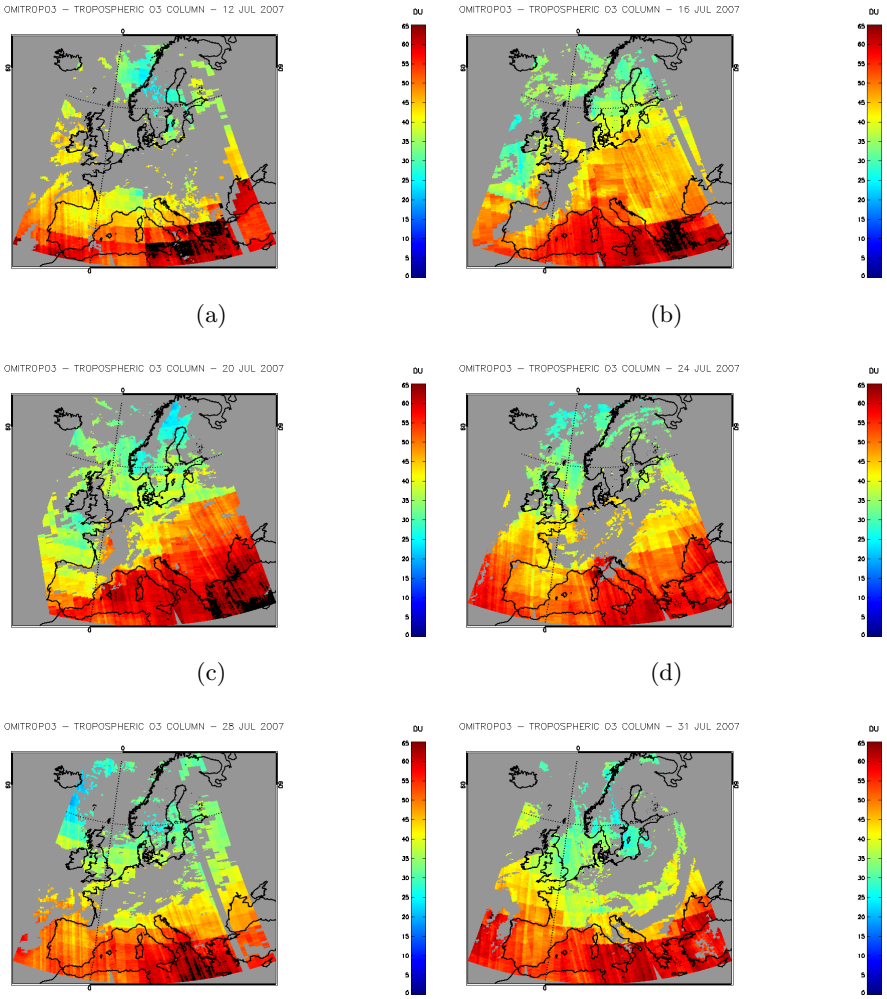

Figure A.4: Maps of TCO, as retrieved by the OMITROPO3-NN algorithm, over Europe, on 12, 16, 20, 24, 28 and 31 July 2007.

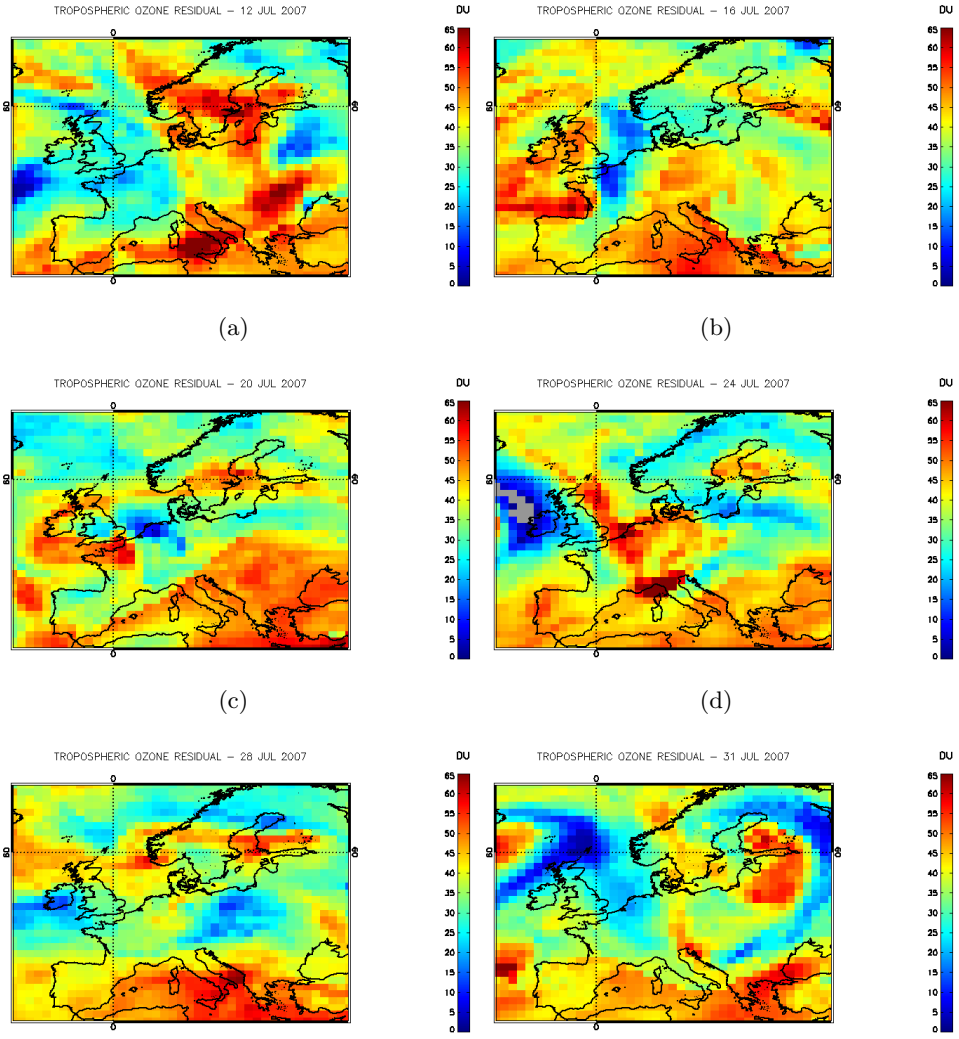

Figure A.5: Maps of TOR, as retrieved by the algorithm described in *Schoeberl et al.* (2007), over Europe, on 12, 16, 20, 24, 28 and 31 July 2007.

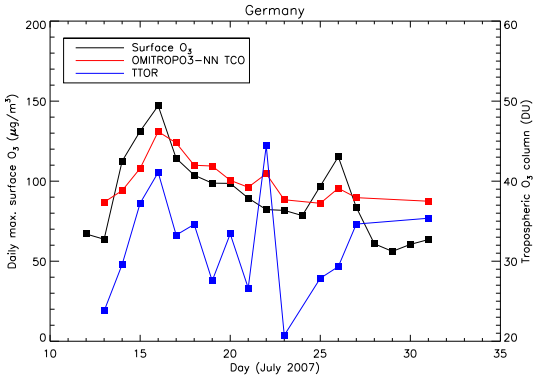

(a)

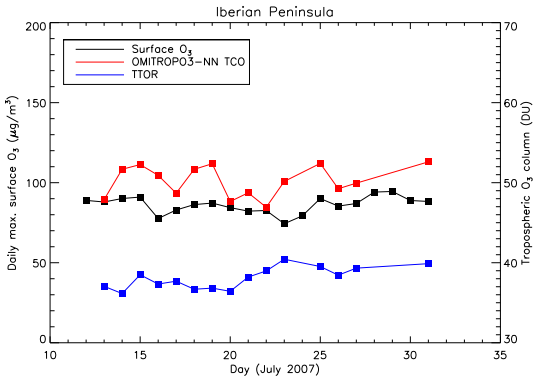

(b)

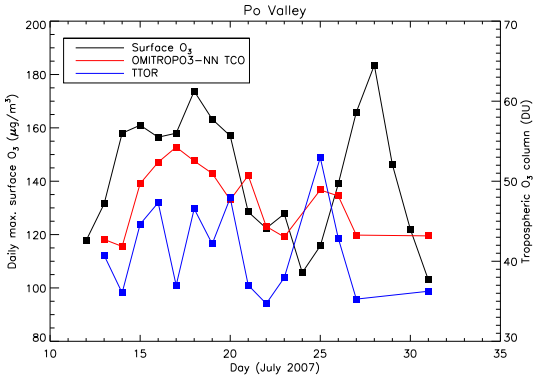

(c)

Figure A.6: Time series of the spatially averaged surface ozone (black), OMITROPO3-NN TCO (red) and TTOR (blue) over Germany (a), Iberian Peninsula (b) and Po Valley (c). The time period goes from July 12 to July 31, 2007.

Bibliography

Ahmad, Z., and P. K. Bhartia (1995), Effect of molecular anisotropy on backscattered ultraviolet radiance, *Appl. Opt.*, *34*(36), 8309–8314, doi:10.1364/AO.34.008309.

Ahn, C., J. R. Ziemke, S. Chandra, and P. K. Bhartia (2003), Derivation of tropospheric column ozone from the Earth Probe TOMS/GOES co-located data sets using the cloud slicing technique, *J. Atmos. Solar-Terr. Phys.*, *65*(10), 1127–1137, doi:10.1016/S1364-6826(03)00166-4.

Aires, F., M. Schmitt, A. Chédin, and N. Scott (1999), The "Weight Smoothing" regularization of MLP for Jacobian stabilization, *IEEE Trans. Neur. Net.*, *10*(6), 1502–1510, doi:10.1109/72.809096.

Aires, F., C. Prigent, W. B. Rossow, and M. Rothstein (2001), A new neural network approach including first-guess for retrieval of atmospheric water vapor, cloud liquid water path, surface temperature and emissivities over land from satellite microwave observations, *J. Geophys. Res.*, *106*(D14), 14,887–14,907, doi:10.1029/2001JD900085.

Aires, F., C. Prigent, and W. B. Rossow (2004a), Neural network uncertainty assessment using Bayesian statistics with application to remote sensing: 2. Output errors, *J. Geophys. Res.*, *109*, D10,304, doi:10.1029/2003JD004174.

Aires, F., C. Prigent, and W. B. Rossow (2004b), Neural network uncertainty assessment using Bayesian statistics with application to remote sensing: 3. Network Jacobians, *J. Geophys. Res.*, *109*, D10,305, doi:10.1029/2003JD004175.

Akaike, H. (1973), Information theory and an extension of the maximum likelihood principle, in *Proceedings of the 2nd International Symposium on Information Theory*, vol. 1, pp. 267–281, Akademiai Kiado, Budapest.

Anenberg, S. C., J. J. West, A. M. Fiore, D. A. Jaffe, M. J. Prather, D. Bergmann, K. Cuvelier, F. J. Dentener, B. N. Duncan, M. Gauss, P. Hess, J. E. Jonson, A. Lupu, I. A. Mackenzie, E. Marmer, R. J. Park, M. G. Sanderson, M. Schultz, D. T. Shindell, S. Szopa, M. García Vivanco, O. Wild, and G. Zeng (2009), Intercontinental impacts of ozone pollution on human mortality, *Environ. Sci. Technol.*, *43*, 6482–6487, doi:10.1021/es900518z.

Bak, J., X. Liu, J. C. Wei, L. L. Pan, K. Chance, and J. H. Kim (2013), Improvement of OMI ozone profile retrievals in the upper troposphere and lower stratosphere by the use of a tropopause-based ozone profile climatology, *Atmos. Meas. Tech.*, *6*, 2239–2254, doi:10.5194/amt-6-2239-2013.

Banzi, M., C. Carbonara, and M. Cervino (1994), Ozone observations at San Pietro Capofiume, Italy: Preliminary results, *Geophys. Res. Lett.*, *21*, 2231–2234, doi:10.1029/94GL01460.

Bass, A. M., and R. J. Paur (1985), The ultraviolet cross-sections of ozone. I. The measurements. II - Results and temperature dependence, in *Atmospheric ozone. Proceedings of the Quadrennial Ozone Symposium, Halkidiki, Greece, 3-7 September1984*, edited by C. S. Zerefos and A. Ghazi, pp. 606–616, Reidel, Dordrecht, The Netherlands.

Bates, D. A. (1984), Rayleigh scattering by air, *Planet. Space Sci.*, *32*(6), 785–790, doi:10.1016/0032-0633(84)90102-8.

Bhahethi, O. P., and R. S. Fraser (1980), Effect of molecular anisotropy on the intensity and degree of polarization of light scattered from model atmospheres, *Appl. Opt.*, *19*(8), 1333–1337, doi:10.1364/AO.19.001333.

Bhartia, P. K., and C. Wellemeyer (2002), TOMS-V8 total O_3 algorithm, in *OMI Ozone Product, OMI-ATBD-02*, vol. ii, edited by P. K. Bhartia, chap. 2, pp. 15–31, NASA Goddard Space Flight Center, Greenbelt, MD, USA.

Bhartia, P. K., R. D. McPeters, C. L. Mateer, L. E. Flynn, and C. Wellemeyer (1996), Algorithm for the estimation of vertical ozone profiles from the Backscattered Ultraviolet (BUV) technique, *J. Geophys. Res.*, *101*, 18,793–18,806, doi:10.1029/96JD01165.

Bishop, C. M. (1995a), *Neural Networks for Pattern Recognition*, Oxford University Press, New York, USA.

Bishop, C. M. (1995b), Training with noise is equivalent to Phillips-Tikhonov regularization, *Neural Comput.*, *7*(1), 108–116, doi:10.1162/neco.1995.7.1.108.

Blackwell, W. J. (2005), A neural-network technique for the retrieval of atmospheric temperature and moisture profiles from high spectral resolution sounding data, *IEEE Trans. Geosci. Remote Sens.*, *43*(11), 2535–2546, doi:10.1109/TGRS.2005.855071.

Blackwell, W. J., and F. W. Chen (2009), *Neural Networks in Atmospheric Remote Sensing*, Artech House, Norwood, MA, USA.

Bodhaine, B. A., N. B. Wood, E. D. Dutton, and J. R. Slusser (1999), On Rayleigh optical depth calculations, *J. Atmos. Oceanic Tech.*, *16*, 1854–1861, doi:10.1175/1520-0426(1999)016<1854:ORODC>2.0.CO;2.

Booker, F., R. Munifering, M. McGrath, K. Burkey, D. Decoteau, E. Fiscus, W. Manning, S. Krupa, A. Chappelka, and D. Grantz (2009), The ozone component of global change: Potential effects on agricultural and horticultural plant yield, product quality and interactions with invasive species, *J. Int. Plant Biol.*, *51*(4), 337–351, doi:10.1111/j.1744-7909.2008.00805.x.

Bucholtz, A. (1995), Rayleigh-scattering calculations for the terrestrial atmosphere, *Appl. Opt.*, *34*(15), 2765–2773, doi:10.1364/AO.34.002765.

Burrows, J. P., M. Weber, M. Buchwitz, V. Rozanov, A. Ladstätter-Weißenmeyer, A. Richter, R. de Beek, R. Hoogen, K. Bramstedt, K.-U. Eichmann, M. Eisinger, and D. Perner (1999), The Global Ozone Monitoring Experiment (GOME): Mission concept and first scientific results, *J. Atmos. Sci.*, *56*, 151–175, doi:10.1175/1520-0469(1999)056<0151:TGOMEG>2.0.CO;2.

Burrows, J. P., A. H. Goede, and C. Muller (2011a), SCIAMACHY – the need for atmospheric research from space, in *SCIAMACHY – Exploring the Changing Earth's Atmosphere*, edited by M. Gottwald and H. Bovensmann, chap. 1, pp. 1–17, Springer, doi:10.1007/978-90-481-9896-2_1.

Burrows, J. P., U. Platt, and P. Borrell (2011b), Tropospheric remote sensing from space, in *The Remote Sensing of Tropospheric Composition from Space*, edited by J. P. Burrows, U. Platt, and P. Borrell, chap. 1, pp. 1–65, Springer, doi:10.1007/978-3-642-14791-3_1.

Carmichael, G. R., I. Uno, M. J. Phadnis, Y. Zhang, and Y. Sunwoo (1998), Tropospheric ozone production and transport in the springtime in east Asia, *J. Geophys. Res.*, *103*(D9), 10,649–10,671, doi:10.1029/97JD03740.

Chameides, W., and J. C. G. Walker (1973), A photochemical theory of tropospheric ozone, *J. Geophys. Res.*, *78*(36), 8751–8760, doi:10.1029/JC078i036p08751.

Chance, K. V., J. P. Burrows, D. Perner, and W. Schneider (1997), Satellite measurements of atmospheric ozone profiles, including tropospheric ozone, from ultraviolet/visible measurements in the nadir geometry: a potential method to retrieve tropospheric ozone, *J. Quant. Spectrosc. Radiat. Transfer*, *57*(4), 467–476, doi:10.1016/S0022-4073(96)00157-4.

Chatfield, R. B., and R. F. Esswein (2012), Estimation of surface O_3 from lower-troposphere partial-column information: Vertical correlations and covariances in ozonesonde profiles, *Atmos. Environ.*, *61*, 103–113, doi:10.1016/j.atmosenv.2012.06.033.

Chevallier, F., F. Chéruy, N. A. Scott, and A. Chédin (1998), A neural network approach for a fast and accurate computation of a long-wave radiative budget, *J. Appl. Meteor.*, *37*, 1385–1397, doi:10.1175/1520-0450(1998)037<1385:ANNAFA>2.0.CO;2.

Chevallier, F., J.-F. Morcrette, F. Chéruy, and N. A. Scott (2000), Use of a neural-network-based long-wave radiative-transfer scheme in the ECMWF atmospheric model, *Q. J. R. Meteorol. Soc.*, *126*(563), 761–776, doi:10.1002/qj.49712656318.

Cortesi, U., J. C. Lambert, C. De Clercq, G. Bianchini, T. Blumenstock, A. Bracher, E. Castelli, V. Catoire, K. V. Chance, M. De Mazière, P. Demoulin, S. Godin-Beekman, N. Jones, N. Jucks, C. Keim, T. Kerzenmacher, H. Kuellmann, J. Kuttippurath, M. Iarlori, G. Y. Liu, Y. Liu, I. S. McDermid, Y. S. Meijer, F. Mencaraglia, S. Mikuteit, H. Oelhaf, C. Piccolo, M. Pirre, P. Raspolini, F. Ravegnani, W. J. Reburn, G. Redaelli, J. J. Remedios, H. Sembhi, D. Smale, T. Steck, A. Taddei, C. Varotsos, C. Vigouroux, A. Waterfall, G. Wetzel, and S. Wood (2007), Geophysical validation of MIPAS-ENVISAT operational ozone data, *Atmos. Chem. Phys.*, *7*, 4807–4867, doi:10.5194/acp-7-4807-2007.

Creilson, J. K., J. Fishman, and A. E. Wozniak (2003), Intercontinental transport of tropospheric ozone: a study of its seasonal variability across

the North Atlantic utilizing tropospheric ozone residuals and its relationship to the North Atlantic Oscillation, *Atmos. Chem. Phys.*, *3*, 2053–2066, doi:10.5194/acp-3-2053-2003.

Creilson, J. K., J. Fishman, and A. E. Wozniak (2005), Arctic Oscillation-induced variability in satellite-derived tropospheric ozone, *Geophys. Res. Lett.*, *32*, L14,822, doi:10.1029/2005GL023016.

Cybenko, G. (1989), Approximation by superpositions of a sigmoidal function, *Math. Contr. Sign. Syst.*, *2*, 303–314, doi:10.1007/BF02551274.

de Laat, A. T. J., I. Aben, and G. J. Roelofs (2005), A model perspective on total tropospheric O_3 column variability and implications for satellite observations, *J. Geophys. Res.*, *110*, D13,303, doi:10.1029/2004JD005264.

Del Frate, F., A. Ortenzi, S. Casadio, and C. Zehner (2002), Application of neural algorithms for a real-time estimation of ozone profiles from GOME measurements, *IEEE Trans. Geosci. Remote Sens.*, *40*, 2263–2270, doi:10.1109/TGRS.2002.803622.

Del Frate, F., M. Iapaolo, S. Casadio, S. Godin-Beekmann, and M. Petitdidier (2005a), Neural networks for the dimensionality reduction of GOME measurement vector in the estimation of ozone profiles, *J. Quant. Spectrosc. Radiat. Transfer*, *92*, 275–291, doi:10.1016/j.jqsrt.2004.07.028.

Del Frate, F., M. Iapaolo, and S. Casadio (2005b), Intercomparison between GOME ozone profiles retrieved by neural network inversion schemes and ILAS products, *J. Atmos. Oceanic Tech.*, *22*, 1433–1440, doi:10.1175/JTECH1764.1.

Delcloo, A., and O. Tuinder (2011), Validation of GOME-2 ozone profiles using balloon sounding data, in *Proceedings of EUMETSAT Meteorological Satellite Conference, Oslo, Norway, 5-9 September 2011*.

Di Noia, A., P. Sellitto, F. Del Frate, and J. de Laat (2012a), Global tropospheric ozone retrievals from OMI data by means of neural networks, in *Proceedings of the ESA Atmospheric Science Conference 2012, Bruges, Belgium, 18-22 June 2012*.

Di Noia, A., P. Sellitto, F. Del Frate, and J. de Laat (2012b), A neural network algorithm to retrieve tropospheric ozone from the Ozone Monitoring Instrument: Design and validation, in *Proceedings of the 9th International Symposium on Tropospheric Profiling (ISTP), L'Aquila, Italy, 3-7 September 2012*.

Di Noia, A., P. Sellitto, F. Del Frate, M. Cervino, M. Iarlori, and V. Rizi (2013a), Tropospheric ozone column retrieval from OMI data by means of neural networks: A validation exercise with ozone soundings over Europe, *EURASIP J. Adv. Sig. Pr.*, *2013*, 21, doi:10.1186/1687-6180-2013-21.

Di Noia, A., P. Sellitto, F. Del Frate, and J. de Laat (2013b), Global tropospheric ozone column retrievals from OMI data by means of neural networks, *Atmos. Meas. Tech.*, *6*(4), 895–915, doi:10.5194/amt-6-895-2013.

Doda, D. D., and A. E. S. Green (1980a), Surface reflectance measurements in the UV from an airborne platform. Part 1, *Appl. Opt.*, *19*(13), 2140–2145, doi:10.1364/AO.19.002140.

Doda, D. D., and A. E. S. Green (1980b), Surface reflectance measurements in the UV from an airborne platform. Part 2, *Appl. Opt.*, *20*(4), 636–642, doi:10.1364/AO.20.000636.

Doicu, A., T. Trautmann, and F. Schreier (2010a), *Numerical Regularization for Atmospheric Inverse Problems*, Springer, Dordrecht, The Netherlands.

Doicu, A., O. Schlüsser, and D. Loyola (2010b), Constrained regularization methods for ozone profile retrieval from UV/VIS nadir spectrometers, *J. Quant. Spectrosc. Rad. Transfer*, *111*, 907–916, doi:10.1016/j.jqsrt.2009.11.020.

Dragani, R. (2011), On the quality of the ERA-Interim ozone reanalyses: comparisons with satellite data, *Q. J. R. Meteorol. Soc.*, *137*, 1312–1326, doi:10.1002/qj.821.

Dybowski, R., and S. J. Roberts (2009), Confidence intervals and prediction intervals for feedforward neural networks, in *Clinical Applications of Artificial Neural Networks*, edited by R. Dybowski, chap. 13, pp. 298–326, Cambridge University Press, Cambridge, UK, doi:10.1017/CBO9780511543494.013.

Ebojie, F., C. von Savigny, A. Ladstätter-Weißenmeyer, A. Rozanov, M. Weber, K. Eichmann, S. Bötel, N. Rahpoe, H. Bovensmann, and J. P. Burrows (2013), Tropospheric column amount of ozone retrieved from SCIAMACHY limb-nadir-matching observations, *Atmos. Meas. Tech. Discuss.*, *6*, 7811–7865, doi:10.5194/amtd-6-7811-2013.

EEA (2008), Air pollution by ozone across Europe during summer 2007, *EEA Technical Report No. 5/2008*, European Environmental Agency, Copenhagen, Denmark.

Entcheva Campbell, P. K., E. M. Middleton, L. A. Corp, and M. S. Kim (2008), Contribution of chlorophyll fluorescence to the apparent vegetation reflectance, *Sci. Total Environ.*, *404*, 433–439, doi:10.1016/j.scitotenv.2007.11.004.

Eremenko, M., G. Dufour, G. Foret, J. Orphal, M. Beekmann, G. Bergametti, and J.-M. Flaud (2008), Tropospheric ozone distributions over Europe during the heat wave in July 2007 observed from infrared nadir spectra recorded by IASI, *Geophys. Res. Lett.*, *35*, L18,805, doi:10.1029/2008GL034803.

Fishman, J. (2000), Observing tropospheric ozone from space, *Prog. Environ. Sci.*, *2*(4), 275–290.

Fishman, J., and J. C. Larsen (1987), Distribution of total ozone and stratospheric ozone in the tropics: Implications for the distribution of tropospheric ozone, *J. Geophys. Res.*, *92*(D6), 6627–6634, doi:10.1029/JD092iD06p06627.

Fishman, J., P. Minnis, and H. G. Reichle Jr. (1986), The use of satellite data to study tropospheric ozone in the tropics, *J. Geophys. Res.*, *91*, 451–465, doi:10.1029/JD091iD13p14451.

Fishman, J., F. M. Vukovich, D. R. Cahoon, and M. C. Shipham (1987), The characterization of an air pollution episode using satellite total ozone measurements, *J. Clim. Appl. Meteor.*, *26*, 1638–1654, doi:10.1175/1520-0450(1987)026<1638:TCOAAP>2.0.CO;2.

Fishman, J., C. E. Watson, J. C. Larsen, and J. A. Logan (1990), Distribution of tropospheric ozone determined from satellite data, *J. Geophys. Res.*, *95*(D4), 3599–3617, doi:10.1029/JD095iD04p03599.

Fishman, J., A. E. Wozniak, and J. K. Creilson (2003), Global distribution of tropospheric ozone from satellite measurements using the empirically corrected tropospheric ozone residual technique: Identification of the regional aspects of air pollution, *Atmos. Chem. Phys.*, *3*, 893–907, doi:10.5194/acp-3-893-2003.

Fishman, J., J. K. Creilson, A. E. Wozniak, and P. J. Crutzen (2005), Interannual variability of stratospheric and tropospheric ozone determined from satellite measurements, *J. Geophys. Res.*, *110*, D20,306, doi:10.1029/2005JD005868.

Fishman, J., J. K. Creilson, P. A. Parker, E. A. Ainsworth, G. G. Vining, J. Szarka, F. L. Booker, and X. Xu (2010), An investigation of widespread ozone damage to the soybean crop in the upper Midwest determined from ground-based and satellite measurements, *Atmos. Environ.*, *44*, 2248–2256, doi:10.1016/j.atmosenv.2010.01.015.

Fortuin, J. P. F., and H. Kelder (1998), An ozone climatology based on ozonesonde and satellite measurements, *J. Geophys. Res.*, *103*, 31,079–31,734, doi:10.1029/1998JD200008.

Fröhlich, C., and G. E. Shaw (1980), New determination of Rayleigh scattering in the terrestrial atmosphere, *Appl. Opt.*, *19*(11), 1773–1775, doi:110.1364/AO.19.001773.

Funahashi, K.-I. (1989), On the approximate realization of continuous mappings by neural networks, *Neural Networks*, *2*, 183–192, doi:10.1016/0893-6080(89)90003-8.

Geman, S., E. Bienenstock, and R. Doursat (1992), Neural networks and the bias/variance dilemma, *Neural Comput.*, *4*, 1–58, doi:10.1162/neco.1992.4.1.1.

Giovanelli, G., G. Lenzi, A. Petritoli, F. Ravegnani, M. Cervino, D. Bortoli, I. Kostadinov, and G. Trivellone (2004), Study of vertical and temporal variability of ozone over Italy, by means of ozone-sounding activity at the S. Pietro Capofiume station, in *Proceedings of the XX Quadrennial Ozone Symposium, Kos, Greece, 1-8 June 2004*, edited by C. S. Zerefos, University of Athens.

Goody, R. M., and Y. L. Yung (2005), *Atmospheric Radiation: Theoretical Basis*, Oxford University Press.

Göttsche, F.-M., and F. S. Olesen (2002), Evolution of neural networks for radiative transfer calculations in the terrestrial infrared, *Rem. Sens. Env.*, *80*(1), 157–164, doi:10.1016/S0034-4257(01)00297-8.

Grainger, J. F., and J. Ring (1962), Anomalous Fraunhofer line profiles, *Nature*, *193*, 762, doi:10.1038/193762a0.

Guanter, L., C. Frankenberg, A. Dudhia, P. E. Lewis, J. Gómez-Dans, A. Kuze, H. Suto, and R. G. Grainger (2012), Retrieval and global assessment of terrestrial chlorophyll fluorescence from GOSAT space measurements, *Rem. Sens. Env.*, *121*, 236–251, doi:10.1016/j.rse.2012.02.006.

Hansen, J. E., and L. D. Travis (1974), Light scattering in planetary atmospheres, *Space Sci. Rev.*, *16*, 527–610, doi:10.1007/BF00168069.

Hasekamp, O. P., and J. Landgraf (2001), Ozone profile retrieval from backscattered ultraviolet radiances: The inverse problem solved by regularization, *J. Geophys. Res.*, *106*(D8), 8077–8088, doi:10.1029/2000JD900692.

Haykin, S. (1999), *Neural Networks: A Comprehensive Foundation*, Prentice Hall, Upper Saddle River, NJ, USA.

Heck, W. W., O. C. Taylor, R. Adams, G. Bingham, J. Miller, E. Preston, and L. Weinstein (1982), Assessment of crop loss from ozone, *J. Air Pollut. Control Assoc.*, *32*, 353–361, doi:10.1080/00022470.1982.10465408.

Herman, J. R., and E. A. Celarier (1997), Earth surface reflectivity climatology at 340–380 nm from TOMS data, *J. Geophys. Res.*, *102*(D23), 28,003–28,011, doi:10.1029/97JD02074.

Hilton, F., R. Armante, T. August, C. Barnet, A. Bouchard, C. Camy-Peiret, V. Capelle, L. Clarisse, C. Clerbaux, P.-F. Coheur, A. Collard, C. Crevoisier, G. Dufour, D. Edwards, F. Faijan, N. Fourrié, A. Gambacorta, M. Goldberg, V. Guidard, D. Hurtmans, S. Illingworth, N. Jacquinet-Hudson, T. Kerzenmacher, D. Klaes, L. Lavanant, G. Masiello, M. Matricardi, A. McNally, S. Newman, E. Pavelin, S. Payan, E. Péquignot, S. Peyridieu, T. Phulpin, J. Remedios, P. Schlüssel, C. Serio, L. Strow, C. Stubenrauch, J. Taylor, D. Tobin, W. Wolf, and D. Zhou (2012), Hyperspectral Earth observation from IASI, *Bull. Amer. Meteor. Soc.*, *93*, 347–370, doi:10.1175/BAMS-D-11-00027.1.

Hoinka, K. P. (1998), Statistics of the global tropopause pressure, *Mon. Wea. Rev.*, *126*, 3303–3325, doi:10.1175/1520-0493(1998)126<3303:SOTGTP>2.0.CO;2.

Holton, J. R., J. H. Haynes, M. E. McIntyre, A. R. Douglass, R. B. Rood, and L. Pfister (1995), Stratosphere-Troposphere Exchange, *Rev. Geophys.*, *33*(4), 403–439, doi:10.1029/95RG02097.

Hornik, K., M. Stinchcombe, and H. White (1989), Multilayer feedforward networks are universal approximators, *Neural Networks*, *2*, 359–366, doi:10.1016/0893-6080(89)90020-8.

Hornik, K., M. Stinchcombe, and H. White (1990), Universal approximation of an unknown mapping and its derivatives using multilayer feedforward networks, *Neural Networks*, *3*, 551–560, doi:10.1016/0893-6080(90)90005-6.

Hudson, R. D., J. H. Kim, and A. M. Thompson (1995), On the derivation of tropospheric column ozone from radiances measured by the total ozone mapping spectrometer, *J. Geophys. Res.*, *100*(D6), 11,137–11,145, doi:10.1029/94JD02435.

Huffman, R. E. (1992), *Atmospheric Ultraviolet Remote Sensing*, Academic Press.

Iapaolo, M., S. Godin-Beekman, F. Del Frate, S. Casadio, M. Petitdidier, I. S. McDermid, T. Leblanc, D. Swart, Y. Meijer, G. Hansen, and K. Stebel (2007), GOME ozone profiles retrieved by neural network techniques: a global validation with lidar measurements, *J. Quant. Spectrosc. Radiat. Transfer*, *107*(1), 105–119, doi:10.1016/j.jqsrt.2007.02.015.

IPCC (2007), Summary for policymakers, in *Climate Change 2007: the Physical Science Basis*, vol. 2, edited by S. Solomon, D. Qin, M. Manning, Z. Chen, M. Marquis, K. B. Averyt, M. Tignor, and H. L. Miller, 2nd ed., pp. 53–76, Cambridge University Press, Cambridge, UK.

Jacob, D. J. (1999), *Introduction to atmospheric chemistry*, Princeton University Press, Princeton, NJ, USA.

Jiang, Y., and Y. L. Yung (1996), Concentrations of tropospheric ozone from 1979 to 1992 over tropical Pacific South America from TOMS data, *Science*, *272*(5262), 714–716, doi:10.1126/science.272.5262.714.

Johnson, B. J., J. H. Vömel, S. J. Oltmans, H. G. J. Smit, T. Deshler, and C. Kroger (2002), Electrochemical concentration cell (ECC) ozonesonde pump efficiency measurements and tests on the sensitivity to ozone of buffered and unbuffered ECC sensor cathode solutions, *J. Geophys. Res.*, *107*(D19), 4393, doi:10.1029/2001JD000557.

Joiner, J., and A. P. Vasilkov (2006), First results from the OMI rotational raman scattering cloud pressure algorithm, *IEEE Trans. Geosci. Remote Sens.*, *44*(5), 1272–1282, doi:10.1109/TGRS.2005.861385.

Joiner, J., P. K. Bhartia, R. P. Cebula, E. Hilsenrath, R. D. McPeters, and H. Park (1995), Rotational Raman scattering (Ring effect) in satel-

lite backscatter ultraviolet measurements, *Appl. Opt.*, *34*(21), 4513–4525, doi:10.1364/AO.34.004513.

Joiner, J., Y. Yoshida, A. P. Vasilkov, Y. Yoshida, L. A. Corp, and M. Middleton (2011), First observations of global and seasonal terrestrial chlorophyll fluorescence from space, *Biogeosciences*, *8*, 637–651, doi:10.5194/bg-8-637-2011.

Kalnay, E., M. Kanamitsu, R. Kistler, W. Collins, D. Deaven, L. Gandin, M. Iredell, S. Saha, G. White, J. Woollen, Y. Zhu, M. Chelliah, M. Ebisuzaki, W. Higgins, J. Janowiak, K. C. Mo, C. Ropelewski, J. Wang, A. Leetmaa, R. Reynolds, R. Jenne, and D. Joseph (1996), The NCEP/NCAR 40-year reanalysis project, *Bull. Amer. Meteor. Soc.*, *77*, 437–470, doi:10.1175/1520-0477(1996)077<0437:TNYRP>2.0.CO;2.

Kar, J., J. Fishman, J. K. Creilson, A. Richter, J. Ziemke, and S. Chandra (2010), Are there urban signatures in the tropospheric ozone column products derived from satellite measurements?, *Atmos. Chem. Phys.*, *10*, 5213–5222, doi:10.5194/acp-10-5213-2010.

Kattawar, G. W., A. T. Young, and T. J. Humphreys (1981), Inelastic scattering in planetary atmospheres. I. The Ring effect, without aerosols, *Astrophys. J.*, *243*, 1049–1057, doi:10.1086/158669.

Kecman, V. (2001), *Learning and Soft Computing. Support Vector Machines, Neural Networks and Fuzzy Logic Models*, MIT Press, Cambridge, MA, USA.

Kim, J. H., and M. J. Newchurch (1996), Climatology and trends of tropospheric ozone over the eastern Pacific Ocean: The influences of biomass burning and tropospheric dynamics, *Geophys. Res. Lett.*, *23*(25), 3723–3726, doi:10.1029/96GL03615.

Kim, J. H., R. D. Hudson, and A. M. Thompson (1996), A new method of deriving time-averaged tropospheric column ozone over the tropics using total ozone mapping spectrometer (TOMS) radiances: Intercomparison and analysis using TRACE A data, *J. Geophys. Res.*, *101*(D19), 24,317–24,330, doi:10.1029/96JD01223.

Kim, J. H., M. J. Newchurch, and K. Han (2001), Distribution of tropical tropospheric ozone determined by the Scan-Angle Method applied to TOMS measurements, *J. Atmos. Sci.*, *58*, 2699–2708, doi:10.1175/1520-0469(2001)058<2699:DOTTOD>2.0.CO;2.

Kim, J. H., S. Na, M. J. Newchurch, and K. J. Ha (2004), Comparison of Scan-Angle Method and Convective Cloud Differential method in retrieving tropospheric ozone from TOMS, *Environ. Monit. Assess.*, *92*, 25–33, doi:10.1023/B:EMAS.0000014506.58857.db.

King, L. V. (1923), On the complex anisotropic molecule in relation to the dispersion and scattering of light, *Proc. Roy. Soc. Lond. A*, *104*(726), 333–357, doi:10.1098/rspa.1923.0113.

Kleipool, Q., M. R. Dobber, J. F. de Haan, and P. F. Levelt (2008), Earth surface reflectance climatology from 3 years of OMI data, *J. Geophys. Res.*, *113*, D18,308, doi:10.1029/2008JD010290.

Kley, D., P. J. Crutzen, H. G. J. Smit, H. Vömel, S. J. Oltmans, H. Grassl, and V. Ramanathan (1996), Observations of near-zero ozone concentrations over the convective Pacific: Effects on air chemistry, *Science*, *274*(5285), 230–233, doi:10.1126/science.274.5285.230.

Koelemeijer, R. B. A., J. F. de Haan, and P. Stammes (2003), A database of spectral surface reflectivity in the range 335-772 nm derived from 5.5 years of GOME observations, *J. Geophys. Res.*, *108*(D2), 4070, doi:10.1029/2002JD002429.

Komhyr, W. D. (1969), Electrochemical concentration cells for gas analysis, *Ann. Geophys.*, *25*, 167–183.

Krasnopolsky, V., and F. Chevallier (2003), Some neural network applications in environmental sciences. Part II: advancing computational efficiency of environmental numerical models, *Neural Networks*, *16*, 335–348, doi:10.1016/S0893-6080(03)00026-1.

Krasnopolsky, V., and S. Schiller (2003), Some neural network applications in environmental sciences. Part I: forward and inverse problems in geophysical remote measurements, *Neural Networks*, *16*, 321–334, doi:10.1016/S0893-6080(03)00027-3.

Krasnopolsky, V. M. (2007), Reducing uncertainties in neural network Jacobians and improving accuracy of neural network emulations with NN ensemble approaches, *Neural Networks*, *20*(4), 454–461, doi:10.1016/j.neunet.2007.04.008.

Krol, M., S. Houweling, B. Bregman, M. van den Broek, A. Segers, P. van Velthoven, W. Peters, F. Dentener, and P. Bergamaschi (2005), The two-way nested global chemistry-transport zoom model TM5: algorithm and

applications, *Atmos. Chem. Phys.*, *5*, 417–432, doi:10.5194/acp-5-417-2005.

Kroon, M., J. F. de Haan, J. P. Veefkind, L. Froidevaux, R. Wang, R. Kivi, and J. J. Hakkarainen (2011), Validation of operational ozone profiles from the Ozone Monitoring Instrument, *J. Geophys. Res.*, *116*, D18,305, doi:10.1029/2010JD015100.

Kurucz, R. L. (1993), Synthetic infrared spectra, in *Infrared Solar Physics*, vol. 154, edited by D. M. Rabin, J. T. Jefferies, and C. Lindsey, pp. 523–531, Springer, doi:10.1007/978-94-011-1926-9_62.

Levelt, P. F., E. Hilsenrath, G. W. Leppelmeier, G. H. J. van den Oord, P. K. Bhartia, J. Tamminen, J. F. de Haan, and P. Veefkind (2006a), Science objectives of the Ozone Monitoring Instrument, *IEEE Trans. Geosci. Remote Sens.*, *44*(5), 1199–1208, doi:10.1109/TGRS.2006.872336.

Levelt, P. F., G. H. J. van den Oord, M. R. Dobber, A. Mälkki, H. Visser, J. de Vries, P. Stammes, J. O. V. Lundell, and H. Saari (2006b), The Ozone Monitoring Instrument, *IEEE Trans. Geosci. Remote Sens.*, *44*(5), 1093–1101, doi:10.1109/TGRS.2006.872333.

Liou, K.-N. (2002), *An Introduction to Atmospheric Radiation*, Academic Press.

Lippmann, M. (1989), Health effects of ozone: A critical review, *J. Air Pollut. Contr. Assoc.*, *39*, 672–695, doi:10.1080/08940630.1989.10466554.

Liu, X., K. Chance, R. J. D. Spurr, T. P. Kurosu, R. V. Martin, and M. J. Newchurch (2005), Ozone profile and tropospheric ozone retrievals from the Global Ozone Monitoring Experiment: Algorithm description and validation, *J. Geophys. Res.*, *110*, D20,307, doi:10.1029/2005JD006240.

Liu, X., K. Chance, C. E. Sioris, T. P. Kurosu, R. J. D. Spurr, R. V. Martin, T. Fu, J. A. Logan, D. J. Jacob, P. I. Palmer, M. J. Newchurch, I. A. Megretskaia, and R. B. Chatfield (2006), First directly retrieved global distribution of tropospheric column ozone from GOME: Comparison with the GEOS-CHEM model, *J. Geophys. Res.*, *111*, D20,308, doi:10.1029/2006JD007374.

Liu, X., P. K. Bhartia, K. Chance, R. J. D. Spurr, and T. P. Kurosu (2010), Ozone profile retrievals from the Ozone Monitoring Instrument, *Atmos. Chem. Phys.*, *10*, 2521–2537, doi:10.5194/acp-10-2521-2010.

Logan, J. A. (1998), An analysis of ozonesonde data for the troposphere: Recommendations for testing 3-D models, and development of a gridded climatology for tropospheric ozone, *J. Geophys. Res.*, *104*(D13), 16,115–16,149, doi:10.1029/1998JD100096.

Long, D. A. (2002), *The Raman Effect: A Unified Treatment of the Theory of Raman Scattering by Molecules*, Wiley, Chichester, England.

López-Puertas, M., and F. W. Taylor (2001), *Non-LTE Radiative Transfer in the Atmosphere*, World Scientific, London, UK.

Mariotti, A., B. Moustaoui, B. Legras, and H. Teitelbaum (1997), Comparison between vertical ozone soundings and reconstructed potential vorticity maps by contour advection with surgery, *J. Geophys. Res.*, *102*(D5), 6131–6142, doi:10.1029/96JD03509.

Massart, S., C. Clerbaux, D. Cariolle, A. Piacentini, S. Turquety, and J. Hadji-Lazaro (2009), First steps towards the assimilation of IASI ozone data into the MOCAGE-PALM system, *Atmos. Chem. Phys.*, *9*, 5073–5091, doi:10.5194/acp-9-5073-2009.

Meier, R. R. (1991), Ultraviolet spectroscopy and remote sensing of the upper atmosphere, *Space Sci. Rev.*, *58*(1), 1–185, doi:10.1007/BF01206000.

Mie, G. (1908), Beiträge zur Optik trüber Medien, speziell kolloidaler Metallösungen, *Ann. Phys.*, *25*(3), 377–445, doi:10.1002/andp.19083300302.

Mishchenko, M. I. (2002), Vector radiative transfer equation for arbitrarily shaped and arbitrarily oriented particles: A microphysical derivation from statistical electromagnetics, *Appl. Opt.*, *41*(33), 7114–7134, doi:10.1364/AO.41.007114.

Møller, M. F. (1993), A Scaled Conjugate Gradient algorithm for fast supervised learning, *Neural Networks*, *6*, 525–533, doi:10.1016/S0893-6080(05)80056-5.

Müller, M. D., A. Kaifel, M. Weber, and J. P. Burrows (2002), Neural network scheme for the retrieval of total ozone from Global Ozone Monitoring Experiment data, *Appl. Opt.*, *41*(24), 5051–5058, doi:10.1364/AO.41.005051.

Müller, M. D., A. K. Kaifel, M. Weber, S. Tellmann, J. P. Burrows, and D. Loyola (2003), Ozone profile retrieval from Global Ozone Monitoring

Experiment (GOME) data using a neural network approach (Neural Network Ozone Retrieval System (NNORSY)), *J. Geophys. Res.*, *108*(D16), 4497, doi:10.1029/2002JD002784.

Munro, R., R. Siddans, W. J. Reburn, and B. J. Kerridge (1998), Direct measurement of tropospheric ozone distributions from space, *Nature*, *392*, 168–171, doi:10.1038/32392.

Natraj, V., X. Liu, S. Kulawik, K. Chance, R. Chatfield, D. P. Edwards, A. Eldering, G. Francis, T. Kurosu, K. Pickering, R. Spurr, and H. Worden (2011), Multi-spectral sensitivity studies for the retrieval of tropospheric and lowermost tropospheric ozone from simulated clear-sky GEO-CAPE measurements, *Atmos. Environ.*, *45*(39), 7151–7165, doi:10.1016/j.atmosenv.2011.09.014.

Newchurch, M. J., X. Liu, and J. H. Kim (2001), Lower-Tropospheric Ozone (LTO) derived from TOMS near mountainous regions, *J. Geophys. Res.*, *106*(D17), 20,403–20,412, doi:10.1029/2000JD000162.

Newchurch, M. J., D. Sun, and X. Liu (2003), Tropical tropospheric ozone derived using Clear-Cloudy Pairs (CCP) of TOMS measurements, *Atmos. Chem. Phys.*, *3*, 683–695, doi:10.5194/acp-3-683-2003.

Oltmans, S. J., A. S. Lefohn, J. M. Harris, I. Galbally, H. E. Scheel, G. Bodeker, E. Brunke, H. Claude, D. Tarasick, B. J. Johnson, P. Simmonds, D. Shadwick, K. Anlauf, K. Hayden, F. Schmidlin, T. Fujimoto, K. Akagi, C. Meyer, S. Nichol, J. Davies, A. Redondas, and E. Cuevas (2006), Long-term changes in tropospheric ozone, *Atmos. Environ.*, *40*, 3156–3173, doi:10.1016/j.atmosenv.2006.01.029.

Penndorf, R. (1957), Tables of the refractive index for standard air and the Rayleigh scattering coefficient for the spectral region between 0.2 and 20.0 μ and their application to atmospheric optics, *J. Opt. Soc. Am.*, *47*(2), 176–182, doi:10.1364/JOSA.47.000176.

Richter, A., and T. Wagner (2011), The Use of UV, Visible and Near IR Solar Back Scattered Radiation to Determine Trace Gases, in *The Remote Sensing of Tropospheric Composition from Space*, edited by J. P. Burrows, U. Platt, and P. Borrell, chap. 2, pp. 67–121, Springer-Verlag, Berlin, Germany, doi:10.1007/978-3-642-14791-3_2.

Rizi, V., M. Iarlori, G. Rocci, G. Redaelli, and G. Visconti (2003), The setup and the performances of L'Aquila Raman lidar and standard PTU and

PTO_3 balloon soundings for envisat validation, in *Proceedings of Envisat Validation Workshop, Frascati, Italy, 9-13 December 2002*, ESA SP-531.

Rodgers, C. D. (1990), Characterization and error analysis of profiles retrieved from remote sounding instruments, *J. Geophys. Res.*, *95*(D5), 5587–5595, doi:10.1029/JD095iD05p05587.

Rodgers, C. D. (2000), *Inverse Methods for Atmospheric Sounding: Theory and Practice*, World Scientific, London, UK.

Rodgers, C. D., and B. J. Connor (2003), Intercomparison of remote sounding instruments, *J. Geophys. Res.*, *108*(D3), 4416, doi:10.1029/2002JD002299.

Rosenkranz, P. W., and D. H. Staelin (1988), Polarized thermal microwave emission from oxygen in the mesosphere, *Radio Sci.*, *23*(5), 721–729, doi:10.1029/RS023i005p00721.

Schoeberl, M. R., A. R. Douglass, E. Hilsenrath, P. K. Bhartia, R. Beer, J. W. Waters, M. R. Gunson, L. Froidevaux, J. C. Gille, J. J. Barnett, P. F. Levelt, and P. DeCola (2006), Overview of the EOS Aura mission, *IEEE Trans. Geosci. Remote Sens.*, *44*, 1066–1074, doi:10.1109/TGRS.2005.861950.

Schoeberl, M. R., J. R. Ziemke, B. Bojkov, N. Livesey, B. Duncan, S. Strahan, L. Froidevaux, S. Kulawik, P. K. Bhartia, S. Chandra, P. F. Levelt, J. C. Witte, A. M. Thompson, E. Cuevas, A. Redondas, D. W. Tarasick, J. Davies, G. Bodeker, G. Hansen, B. J. Johnson, S. J. Oltmans, H. Vömel, M. Allaart, H. Kelder, M. Newchurch, S. Godin-Beekmann, G. Ancellet, H. Claude, S. B. Andersen, E. Kyrö, M. Parrondos, M. Yela, G. Zablocki, D. Moore, H. Dier, P. von der Gathen, P. Viatte, R. Stübi, B. Calpini, P. Skrivankova, V. Dorokhov, H. de Backer, F. J. Schmidlin, G. Coetzee, M. Fujiwara, V. Thouret, F. Posny, G. Morris, J. Merrill, C. P. Leong, G. Koenig-Langlo, and E. Joseph (2007), A trajectory-based estimate of the tropospheric ozone column using the residual method, *J. Geophys. Res.*, *112*, D24S49, doi:10.1029/2007JD008773.

Schwander, H., A. Kaifel, A. Ruggaber, and P. Koepke (2001), Spectral radiative-transfer modeling with minimized computation time by use of a neural-network technique, *Appl. Opt.*, *40*(3), 331–335, doi:10.1364/AO.40.000331.

Sellitto, P., A. Burini, F. Del Frate, and S. Casadio (2007), Dedicated neural network algorithms for direct estimation of tropospheric ozone from satellite measurements, in *Proceedings of IEEE International Geosciences and Remote Sensing Symposium (IGARSS) 2007, Barcelona, Spain, 23-28 July 2007*, pp. 1685–1688, doi:10.1109/IGARSS.2007.4423141.

Sellitto, P., B. R. Bojkov, X. Liu, K. Chance, and F. Del Frate (2011), Tropospheric ozone column retrieval at northern mid-latitudes from the Ozone Monitoring Instrument by means of a neural network algorithm, *Atmos. Meas. Tech.*, *4*, 2375–2388, doi:10.5194/amt-4-2375-2011.

Sellitto, P., F. Del Frate, D. Solimini, and S. Casadio (2012a), Tropospheric ozone column retrieval from ESA-Envisat SCIAMACHY nadir UV/VIS measurements by means of a neural network algorithm, *IEEE Trans. Geosci. Remote Sens.*, *50*(3), 998–1011, doi:10.1109/TGRS.2011.2163198.

Sellitto, P., A. Di Noia, F. Del Frate, A. Burini, S. Casadio, and D. Solimini (2012b), On the role of visible radiation in ozone profile retrieval from nadir UV/VIS satellite measurements: An experiment with neural network algorithms inverting SCIAMACHY data, *J. Quant. Spectrosc. Rad. Transfer*, *113*(12), 1429–1436, doi:10.1016/j.jqsrt.2012.04.007.

Shapiro, M. A. (1980), Turbulent mixing within the tropopause folds as a mechanism for the exchange of chemical constituents between the stratosphere and the troposphere, *J. Atmos. Sci.*, *37*, 994–1004, doi:10.1175/1520-0469(1980)037<0994:TMWTFA>2.0.CO;2.

Shindell, D. T., G. Faluvegi, A. Lacis, J. Hansen, R. Ruedy, and E. Aguilar (2006), Role of tropospheric ozone increases in 20th-century climate change, *J. Geophys. Res.*, *111*, D08,302, doi:10.1029/2005JD006348.

Tarasick, D. W., J. J. Jin, V. E. Fioletov, G. Liu, A. M. Thompson, S. J. Oltmans, J. Liu, C. E. Sioris, X. Liu, O. R. Cooper, T. Dann, and V. Thouret (2010), High-resolution tropospheric ozone fields for INTEX and ARCTAS from IONS ozonesondes, *J. Geophys. Res.*, *15*, D20,301, doi:10.1029/2009JD012918.

Thompson, A. M., J. C. Witte, R. D. McPeters, S. J. Oltmans, F. J. Schmidlin, J. A. Logan, M. Fujiwara, V. W. J. H. Kirchhoff, F. Posny, G. J. R. Coetzee, B. Hoegger, S. Kawakami, T. Ogawa, B. J. Johnson, H. Vömel, and G. Labow (2003), Southern Hemisphere Additional Ozonesondes (SHADOZ) 1998–2000 tropical ozone climatology 1. Comparison with Total Ozone Mapping Spectrometer (TOMS)

and ground-based measurements, *J. Geophys. Res.*, *108*(D2), 8238, doi:10.1029/2001JD000967.

Thompson, A. M., S. K. Miller, S. Tilmes, D. W. Kollonige, J. C. Witte, S. J. Oltmans, B. J. Johnson, M. Fujiwara, F. J. Schmidlin, G. J. R. Coetzee, N. Komala, M. Maata, M. bt Mohamad, J. Nguyo, C. Mutai, S.-Y. Ogino, F. R. da Silva, N. M. Paes Leme, F. Posny, R. Scheele, H. B. Selkirk, M. Shiotani, R. Stübi, G. Levrat, B. Calpini, V. Thouret, H. Tsuruta, J. Valverde Canossa, H. Vömel, S. Yonemura, J. A. Diaz, N. T. Tan Thanh, and H. T. Thuy Ha (2012), Southern Hemisphere Additional Ozonesondes (SHADOZ) ozone climatology (2005-2009): Tropospheric and tropical tropopause layer (TTL) profiles with comparison with OMI-based ozone products, *J. Geophys. Res.*, *117*, D23,301, doi:10.1029/2011JD016911.

Tikhonov, A. N., and V. Y. Arsenin (1977), *Solutions of Ill-posed Problems*, Wiley, Hoboken, NJ, USA.

Torres, O., P. K. Bhartia, J. R. Herman, Z. Ahmad, and J. Gleason (1998), Derivation of aerosol properties from satellite measurements of backscattered ultraviolet radiation: Theoretical basis, *J. Geophys. Res.*, *103*(D14), 17,099–17,110, doi:10.1029/98JD00900.

Turquety, S., J. Hadji-Lazaro, C. Clerbaux, D. A. Hauglustaine, S. A. Clough, V. Cassé, P. Schlüssel, and G. Mégie (2004), Operational trace gas retrieval algorithm for the Infrared Atmospheric Sounding Interferometer, *J. Geophys. Res.*, *109*, D21,301, doi:10.1029/2004JD004821.

Twomey, S. (1977), *Introduction to the Mathematics of Inversion in Remote Sensing and Indirect Measurements*, Elsevier Publishing Company, New York, NY, USA.

Valks, P., R. B. A. Koelemeijer, M. van Weele, P. van Velthoven, J. P. F. Fortuin, and H. Kelder (2003), Variability in tropical tropospheric ozone: Analysis with Global Ozone Monitoring Experiment observations and a global model, *J. Geophys. Res.*, *108*(D11), 4328, doi:10.1029/2002JD002894.

van Deelen, R. (2007), Rotational Raman scattering in the Earth's atmosphere, Ph.D. thesis, Vrije Universiteit Amsterdam.

van den Oord, B., and P. Veefkind (2002), Interpretation flags in OMI Level 1B data products, *Tech. Rep. RP-OMIE-KNMI-396*, Royal Netherlands Meteorological Institute, De Bilt, The Netherlands.

Vasilkov, A. P., J. Joiner, J. Gleason, and P. K. Bhartia (2002), Ocean Raman scattering in satellite backscatter UV measurements, *Geophys. Res. Lett.*, *29*, 1837, doi:10.1029/2002GL014955.

Veefkind, J. P., I. Aben, K. McMullan, H. Förster, J. de Vries, G. Otter, J. Claas, H. J. Eskes, J. F. de Haan, Q. Kleipool, M. van Weele, O. Hasekamp, R. Hoogeveen, J. Landgraf, R. Snel, P. Tol, P. Ingmann, R. Voors, B. Kruizinga, R. Vink, H. Visser, and P. F. Levelt (2012), TROPOMI on the ESA Sentinel-5 Precursor: A GMES mission for global observations of the atmospheric composition for climate, air quality and ozone layer applications, *Rem. Sens. Env.*, *120*, 70–83, doi:10.1016/j.rse.2011.09.027.

Veihelmann, B., and Q. Kleipool (2006), Reducing along-track stripes in OMI Level 2 products, *Tech. Rep. TN-OMIE-KNMI-785*, Royal Netherlands Meteorological Institute, De Bilt, The Netherlands.

Verhoeven, G. J., and K. D. Schmitt (2010), An attempt to push back frontiers – digital near-ultraviolet aerial archaeology, *J. Archaeol. Sci.*, *37*(4), 833–845, doi:10.1016/j.jas.2009.11.013.

Vömel, H., and K. Diaz (2010), Ozone sonde cell current measurements and implications for observations of near-zero ozone concentrations in the tropical upper troposphere, *Atmos. Meas. Tech.*, *3*, 495–505, doi:10.5194/amt-3-495-2010.

Vountas, M., V. V. Rozanov, and J. P. Burrows (1998), Ring effect: Impact of rotational Raman scattering on radiative transfer in Earth's atmosphere, *J. Quant. Spectrosc. Rad. Transfer*, *60*(6), 943–961, doi:10.1016/S0022-4073(97)00186-6.

Wei, J. C., L. L. Pan, E. Maddy, J. V. Pittman, M. Divarkarla, X. Xiong, and C. Barnet (2010), Ozone profile retrieval from an advanced infrared sounder: Experiments with tropopause-based climatology and optimal estimation approach, *J. Atmos. Oceanic Tech.*, *27*(7), 1123–1139, doi:10.1175/2010JTECHA1384.1.

Werbos, P. J. (1974), Beyond Regression: New Tools for Prediction and Analysis in the Behavioral Sciences, Ph.D. thesis, Harvard University.

Westwater, E. R. (2003), Profile retrieval estimation techniques, in *Remote Sensing of Atmosphere and Ocean from Space: Models, Instruments and Techniques*, edited by F. S. Marzano and G. Visconti, chap. 3, pp. 35–47, Kluwer Academic Publishers, Dordrecht, The Netherlands.

Williams, J. E., A. Strunk, V. Huijnen, and M. van Weele (2012), The application of the Modified Band Approach for the calculation of on-line photodissociation rate constants in TM5: implications for oxidative capacity, *Geosci. Model Dev.*, *5*, 15–35, doi:10.5194/gmd-5-15-2012.

Yang, Q., D. M. Cunnold, H.-J. Wang, L. Froidevaux, H. Claude, J. Merrill, M. Newchurch, and S. J. Oltmans (2007), Midlatitude tropospheric ozone columns derived from the Aura Ozone Monitoring Instrument and Microwave Limb Sounder measurements, *J. Geophys. Res.*, *112*, D20,305, doi:10.1029/2007JD008528.

Young, A. T. (1980), Revised depolarization corrections for atmospheric extinction, *Appl. Opt.*, *19*(20), 3427–3428, doi:10.1364/AO.19.003427.

Young, A. T. (1981), On the Rayleigh scattering optical depth of the atmosphere, *J. Appl. Meteorol.*, *20*(3), 328–329, doi:10.1175/1520-0450(1981)020<0328:OTRSOD>2.0.CO;2.

Young, A. T. (1982), Rayleigh scattering, *Phys. Today*, *35*(1), 42–48, doi:10.1063/1.2890003.

Ziemke, J. R., S. Chandra, and P. K. Bhartia (1998), Two new methods for deriving tropospheric column ozone from TOMS measurements: The assimilated UARS MLS/HALOE and convective-cloud differential techniques, *J. Geophys. Res.*, *103*(D17), 22,115–22,127, doi:10.1029/98JD01567.

Ziemke, J. R., S. Chandra, and P. K. Bhartia (2001), "Cloud slicing": A new technique to derive upper tropospheric ozone from satellite measurements, *J. Geophys. Res.*, *106*(D9), 9853–9867, doi:10.1029/2000JD900768.

Ziemke, J. R., S. Chandra, B. N. Duncan, L. Froidevaux, P. K. Bhartia, P. F. Levelt, and J. W. Waters (2006), Tropospheric ozone determined from Aura OMI and MLS: Evaluation of measurements and comparison with the Global Modeling Initiative's Chemical Transport Model, *J. Geophys. Res.*, *111*, D19,303, doi:10.1029/2006JD007089.

Ziemke, J. R., S. Chandra, G. J. Labow, P. K. Bhartia, L. Froidevaux, and J. C. Witte (2011), A global climatology of tropospheric and stratospheric ozone derived from Aura OMI and MLS measurements, *Atmos. Chem. Phys.*, *11*, 9237–9251, doi:10.5194/acp-11-9237-2011.

Zoogman, P., D. J. Jacob, K. Chance, L. Zhang, P. Le Sager, A. M. Fiore, A. Eldering, X. Liu, V. Natraj, and S. Kulawik (2011), Ozone air quality measurement requirements for a geostationary missions, *Atmos. Environ.*, *45*(39), 7143–7150, doi:10.1016/j.atmosenv.2011.05.058.